



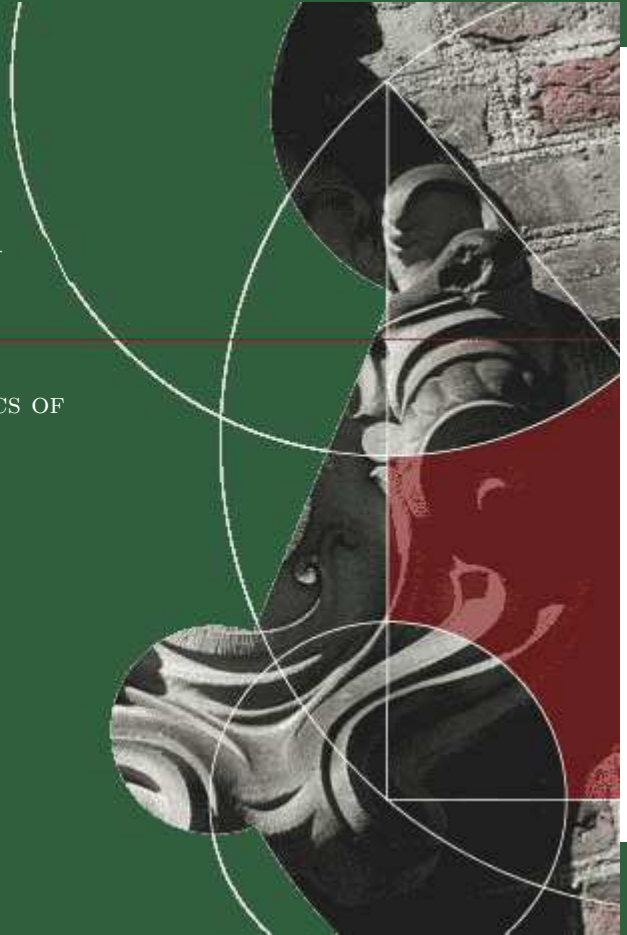
UNIVERSITY OF COPENHAGEN
THE FACULTY OF SCIENCE

THESIS SUBMITTED FOR THE DEGREE IN ASTROPHYSICS OF
DOCTOR OF PHILOSOPHY

EVOLUTION PROBLEMS
OF
GENERAL RELATIVITY

Jakob Hansen

Niels Bohr Institute – February 2005



The present thesis appears in partial fulfilments of the requirements for the Ph.D. degree at the Faculty of Science at the University of Copenhagen. The work has been supervised by:

Internal supervisor:

**Professor Igor D. Novikov
Niels Bohr Institute
Blegdamsvej 17
DK-2100 København Ø
DENMARK
E-mail: novikov@nbi.dk**

External supervisor:

**Professor Alexei M. Khokhlov
Department of Astronomy and Astrophysics
The University of Chicago
5640 South Ellis Avenue
Chicago, IL 60637
USA
E-mail: ajk@oddjob.uchicago.edu**

Copies of the thesis may be obtained by contacting the author:

**Jakob Hansen
Niels Bohr Institute
Blegdamsvej 17
DK-2100 København Ø
DENMARK
E-mail: jahansen@nbi.dk**

©2005 - Jakob Hansen.

Preface

The thesis at hand represents one of the last steps of my Ph.D. studies at the University of Copenhagen. It has been a long and interesting journey, physically and mentally, into the fields of general and numerical relativity. At times it has been a bumpy ride and there has been many unexpected turns along the way. But it has also been a great adventure which has taken me across three continents to some of the research hotspots and it has given me the opportunity to meet some of the most brilliant theoreticians and numerical experimentalists currently working in the field at a time which seems to be the golden age of numerical relativity.

This thesis is the physical manifestation of this journey. It is written with the intention that it should be a presentation of the work which I have done during my Ph.D. studies. I have therefore chosen to present it in the form of the concrete work which have resulted from my Ph.D. studies, that is my research papers. Unfortunately this approach also means that the thesis is aimed at specialists and may seem somewhat inaccessible to outsiders of the field of numerical relativity, not to mention any non-physicist who may dare to read it! However, if the thesis should have included thorough introductions to all the topics and concepts, the thesis would probably have been equally inaccessible due to the size it would have. To the interested readers who wish to further explore the topics in the thesis I have included some important references at the end of each chapters. Furthermore, any reader with unanswered questions should not hesitate to contact me for clarification.

Great thanks should be given to the many people from all around the world who have helped, supported and encouraged me in various ways during my studies and in the making of this thesis. Especially I owe great gratitude to my supervisors, Igor Novikov and Alexei Khoklov; You have been a source of great inspiration and valuable insight and I am proud to have made my Ph.D. under your supervision. I am also much indebted to my family and friends whose support and understanding helped me through hard times and made a significant difference; Thank you for accepting and understanding my need for isolation and solitude during long periods and yet always being there for me when I needed your help. A special heartfelt thanks is given to Stina, thank you for being there when I needed it the most. Finally I wish to thank the Theoretical Astrophysics Center (TAC) for sponsoring my Ph.D. and the Niels Bohr Institute for "adopting" me when TAC was closed.

Jakob Hansen

Copenhagen, Denmark,
February, 2005.

Contents

Preface	iii
Introduction	3
References for the Introduction	5
I Numerical Studies	7
1 Elements of numerical relativity	9
1.1 Setting the scene	9
1.1.1 Formulation	9
1.1.2 Lapse and shift	10
1.1.3 Boundary and initial conditions	11
1.1.4 Further developments	11
1.2 Numerical issues	12
References for Chapter 1	15
2 Properties of Four Numerical Schemes Applied to a Nonlinear Scalar Wave Equation with a GR-type Nonlinearity	17
2.1 Introduction	18
2.2 Formulation of the problem	18
2.2.1 A Non-linear Wave Equation	18
2.2.2 Perturbation analysis	19
2.2.3 The Numerical Schemes	20
2.2.4 The Von Neumann analysis	23
2.3 The linear scalar wave equation	24
2.4 Von Neumann stability analysis of the non-linear wave equation	29
2.4.1 The spatial constant solutions	30
2.4.2 The exponential solutions	30
2.5 Numerical Tests	33
2.6 Discussion and conclusion	35
2.7 Acknowledgements	36
References for Chapter 2	36
II Physical Studies	37
3 Internal structure of black holes	39
3.1 Analytic solutions	39
3.2 Physical phenomena	41
3.2.1 Ingoing fluxes	41

3.2.2	Simultaneous in- and outgoing fluxes	41
3.2.3	Quantum effects	43
3.3	More realistic models	43
	References for Chapter 3	44
4	Physics of the interior of a spherical, charged black hole with a scalar field	47
4.1	Introduction	48
4.2	The model	49
4.2.1	Field equations	49
4.2.2	Initial value problem	51
4.3	Nonlinear effects; internal mass function	52
4.4	Homogeneous approximation	53
4.4.1	Dust, $P = 0$	55
4.4.2	Massless scalar field	56
4.4.3	Ultrarelativistic gas, $P = \frac{\epsilon}{3}$	60
4.5	Physics of the interior	61
4.5.1	Simple compact pulse	61
4.5.2	Double sine pulse	69
4.5.3	The influence of the T_{uu} flux	70
4.6	Conclusions	73
4.7	Acknowledgements	74
	Appendix 4.A: The numerical code	74
	Appendix 4.A.1: The numerical scheme	74
	Appendix 4.A.2: Splitting algorithm	75
	Appendix 4.B: Analysis of the code	76
	Appendix 4.B.1: Basic convergence tests	76
	Appendix 4.B.2: Convergence with AMR	79
	References for Chapter 4	81

Evolution Problems of General Relativity

Introduction

The theory of general relativity is without doubt one of the most successful and sensational physical theories of the 20th century. Not only has it passed all feasible experimental tests and predictions with unprecedented accuracy, it has also drastically changed the way we think of space, time and gravity.

At the heart of the theory are the Einstein equations which (using the Einstein summation convention) can be written as:

$$(R_{\mu\nu} - \frac{1}{2}R g_{\mu\nu}) = 8\pi T_{\mu\nu}, \quad (1)$$

using $c = G = 1$ and indices running from 0 to 4. Theoretical research in classical general relativity basically boils down to solving this (seemingly simple) set of equations. This, however, is far from easy since the equations form a system of ten coupled nonlinear partial differential equations in four dimensions, which, when fully expanded in a general coordinate system, have literally thousands of terms. Because of this complexity, exact analytical solutions can only be found in very simplified scenarios involving high degrees of symmetry and numerous simplifications. When one is interested in studying highly dynamic systems that have little or no symmetry, it is simply impossible to solve the equations analytically. This has naturally led to the advent of numerical relativity, i.e. the "art" of solving and studying the Einstein equations numerically.

Numerical relativity was born in the 1960s with the pioneering work of Hahn and Lindquist[1], who tried to numerically solve the Einstein equations for two colliding black holes. However, appropriate methods for obtaining stable and accurate numerical solutions had not yet been developed for such a complex theory, the theory behind black holes was still in development and the computational resources available at the time were insufficient. Because of these difficulties the project was doomed to failure, but the field of numerical relativity was born and interest in the subject was spreading.

By the middle of the 1970s great advances had been made in the theoretical foundation of black holes and numerical algorithms and computers were growing more powerful. Led by these advances Smarr and Eppley[2, 3] performed the first successful simulations of head-on collisions of black holes and showed that two black holes colliding head-on would merge to form a single black hole. They also demonstrated that the black hole resulting from the merger oscillates with a special frequency or "ringing mode". With these simulations and discoveries the modern era of numerical relativity was born.

Since then numerical relativity has been a rapidly advancing field and has been used to study gravitational collapse, critical phenomenas in general relativity, singularities, interior structure of black holes, gravitational waves and compact objects to name a few applications. However, the subfield that has received the most attention by far (and is often taken to be synonymous with numerical relativity) is the problem of simulating colliding black holes, commonly referred to as *the* evolution problem. By the middle of the 1990s large interferometric gravitational wave detectors had begun their construction. This initiated a lot of work in an effort to predict the gravitational waveforms emitted by in-spiralling and colliding black

holes which are needed to decipher gravitational wave observations. However, the problem turned out to be far more complex than initially assumed and even though great progress was made under the National Science Foundation "Binary Black Hole Grand Challenge" project which brought a number of US institutions together in a combined effort, the problem was not (and has not yet completely been) solved. Since the end of the Grand Challenge project a number of groups have continued to simulate the in-spiral of two black holes. In recent years, there has been rapid progress due to the use of more robust well-posed formulations of the evolution equations, such as BSSN[4], the development of improved gauge conditions, advanced excision techniques and numerical techniques such as the use of adaptive mesh refinement and parallel computing. Recently, this evolution problem has moved into the realm of orbiting black holes[5] and the numerical relativity community is now closer than ever before to solving the problem of simulating the orbiting and collision of black holes. At the same time, numerical relativity has reached a level of maturity that allows it to be used to study ever more complex systems and increasingly realistic systems.

The subject of my Ph.D. studies at the University of Copenhagen has been the field of numerical relativity. Specifically, my main interest and focus has been on evolution problems with brief strays to adjacent topics such as the initial value problem ([6]).

The first part of my studies has been devoted to a somewhat technical aspect of numerical relativity, namely the analysis of numerical schemes used for numerical integration of evolution equations. This topic is not exclusive to numerical relativity, but is of great importance in all branches of numerical physics. However, in numerical relativity, this topic is perhaps even more important than elsewhere because of the complexity of the overall problem. Although numerical relativity has indeed come a long way since its infancy, the "holy grail" of producing stable, generic, fully 3D evolutions of orbiting and colliding black holes has still not been achieved. It is now clear that this "lack of success" is due to many factors. The problems of choosing the system of evolution equations, choice of coordinates/gauge, determination of initial data and boundary conditions (and other key problems) have each proved to be far more complex than one could fear. While great analytical efforts are required to solve these problems, numerical methods are the "glue" that bind these subproblems together and in the end, the hard work of simulating spacetimes will be done by computers. Hence, it is clear that if inadequate numerical techniques are used to evolve the chosen system of equations, the simulations will crash despite any inherent stability properties of the evolution equations. On the other hand, any numerical calculation will always produce some amount of roundoff and truncation errors that will contaminate the simulation data and thus the evolution system must be stable enough to deal with this inevitable numerical noise. Furthermore, although computers are continuously growing more powerful and are steadily becoming more widely available, computational resources are not unlimited. Thus, one wishes to have the highest possible amount of computational accuracy and stability with as few computations as possible. These two objectives are somewhat contradictory and the job of the numerical technician is to construct numerical methods that optimise the relation between numerical accuracy and computational cost while keeping the simulation stable.

In chapter 1 of this thesis, I briefly review some of the key problems in creating stable numerical relativistic simulations and in chapter 2, I present the work which I have done in this field in the form of the paper "Properties of four numerical schemes applied to a nonlinear scalar wave equation with a GR-type nonlinearity"[7] in which the properties of four numerical schemes suitable for use in numerical relativity are analysed when applied to both linear and nonlinear scalar wave equations.

While numerical techniques and analyses are most important aspects of numerical relativity, it was my desire to also include a more physical aspect of numerical relativity in my Ph.D. studies. Most of the efforts in numerical relativity have been aimed at the problem

of colliding black holes and the resulting emission of gravitational waves, however, this is only one of many unsolved evolution problems that can be approached by numerical methods. For the second part of the thesis I have chosen to study the physics of the interior of black holes. An important point for understanding this problem is the fact that the path into the gravitational abyss of the interior of a black hole is a progression in time[8], which makes the problem of the black hole interior an evolutionary problem. A result of this is that if one knows the conditions on the border of a black hole, it is in principle possible to integrate the Einstein equations in time and thereby learn the structure of internal layers of a black hole. The problem of the internal structure of black holes has been the subject of increasingly active investigations in recent decades and numerical studies have proved invaluable in analysing the details of this problem. One might expect that the interior of black holes is a dark and dull place where nothing but the devastating forces of the singularity await the unfortunate infalling observer. This however, turns out not to be the case and the studies have shown that the interior of perturbed black holes is governed by dynamical nonlinear processes creating interesting physical phenomena (although the question whether it is possible to travel "through" the black hole into another universe is still a partially open question). Many important results of the internal structure of black holes have been achieved by analytical approaches, however, as in most branches of physics, if one wishes to know the full effects of complex nonlinear interactions in the strong field regime, numerical methods are the only feasible approach.

In chapter 3, I give a brief introduction to the topic of physics of the interior of black holes. This is followed by the paper "Physics of the interior of a spherical, charged black hole with a scalar field"[9] in chapter 4, in which I present the studies and results we have performed using numerical models to analyse physical processes in the interior of a spherical, charged black hole which is perturbed by scalar fields.

Finally it should be noted that the papers, presented in chapters 2 and 4, have been typographically formatted for this thesis in order to be presented in a coherent form, but the contents of the papers are completely identical to the form in which they have been published.

References for the Introduction

- [1] S. Hahn and R. Lindquist, *Ann. Phys.* **29**, 304 (1964).
- [2] K. Eppley, Ph.D. thesis, Princeton University (1975).
- [3] L. Smarr, A. Cadez, B. DeWitt, and K. Eppley, *Phys. Rev.* **D14**, 2443 (1976).
- [4] T. W. Baumgarte and S. L. Shapiro, *Phys. Rev.* **D59**, 024007 (1999).
- [5] B. Brügmann, W. Tichy, and N. Jansen, *Phys. Rev. Lett.* **92**, 211101 (2004).
- [6] N. Jansen, P. Diener, J. Hansen, A. Khokhlov, and I. Novikov, *Class. Quant. Grav* **20**, 51 (2003).
- [7] J. Hansen, A. Khokhlov, and I. Novikov, *Int. J. Mod. Phys.* **D13**, 961 (2004).
- [8] V. Frolov and I. Novikov, *Black Hole Physics* (Kluwer Academic Publishers, 1998).
- [9] J. Hansen, A. Khokhlov, and I. Novikov, "Physics of the interior of a spherical, charged black hole with a scalar field", Accepted for publication in *Phys. Rev. D*, gr-qc/0501015. (2005).

Part I

Numerical Studies

Chapter 1

Elements of numerical relativity

Numerical relativity can basically be defined as the task of finding solutions to the Einstein equations by numerical methods. However, although the numerical approach can be a powerful tool that can be used to solve highly complex problems, it is not a magic black box that takes initial data and equations as input and spits out solutions. In some ways this method is even more difficult in that one must worry not only about the standard points of the paper and pencil method, but also consider issues related to the numerical approach, while ensuring that all the individual components of the problem play well together.

In this chapter I will briefly describe some of the key elements involved in performing a numerical integration of the Einstein equations. For more thorough introductions to the key problems of numerical relativity see e.g. [1, 2] and references therein.

1.1 Setting the scene

Before one can begin to find numerical solutions to the Einstein equations, there are a number of issues that first need to be considered in order to make the problem well suited for numerical investigations:

1.1.1 Formulation

When the Einstein equations are written in fully covariant form:

$$(R_{\mu\nu} - \frac{1}{2}Rg_{\mu\nu}) = 8\pi T_{\mu\nu}, \quad (\mu, \nu = 0, \dots, 3 \text{ and } c = G = 1) \quad (1.1)$$

they are completely independent of any coordinate system and with space and time being treated on an equal base. This is a very elegant and powerful way of posing the equations, but when one wishes to study the evolution in time of a dynamic gravitational system, it is not very useful.

Luckily, general relativity allows the Einstein equations to be posed as an initial value formulation[3, 4], i.e. it is possible to specify conditions on an initial hypersurface and obtain its future development by means of solving the Einstein equations, which is what we need for our purpose.

Today there are three main procedures for writing the Einstein equations in an initial value formulation. Most common is the "Cauchy" or "3+1" approach, in which the spacetime is split into a foliation of 3-dimensional spacelike hypersurfaces which are parametrised along a (1-dimensional) time direction.

A similar approach is the conformal, in which spacetime is also split into a foliation of spacelike hypersurfaces, however, where the hypersurfaces in the 3+1 approach reach spatial

infinity, they are hyperboloidal in the conformal approach and reach future null infinity instead. This naturally has the advantage of eliminating the need for advanced boundary conditions at a finite distance as must be introduced in the 3+1 approaches.

Finally there is the characteristic approach in which the spacetime is foliated into a sequence of lightlike hypersurfaces. This makes the characteristic approach well suited to study key issues regarding gravitational radiation. In part II of this thesis, a (1 + 1)variant of this approach will be used to study the interior structure of spherical black holes.

These three approaches each have advantages and disadvantages. However, the 3+1 approach has so far received the most attention in numerical relativity. The mother of practically all 3+1 approaches to numerical relativity is based on a formulation of the Einstein equations first formulated by Arnowitt, Deser and Misner in 1962[5]*.

In this approach a three-dimensional metric γ_{ij} measuring distances within a (three-dimensional) spacelike hypersurface is defined. Also, the extrinsic curvature tensor, K_{ij} , is introduced, which measures how the spatial hypersurfaces are immersed in spacetime. Lastly, two additional functions are introduced, these are the “lapse” function α which measures the proper time between two adjacent hypersurfaces and the “shift” vector β^i which measures the relative speed between observers moving along the normal direction to the hypersurfaces and those keeping constant spatial coordinates.

Based on these definitions, the Einstein equations (for vacuum) can be written as:

$$(\partial_t - \mathcal{L}_\beta)g_{ij} = -2\alpha K_{ij} \quad (1.2)$$

$$(\partial_t - \mathcal{L}_\beta)K_{ij} = -D_i D_j \alpha + \alpha(R_{ij} - 2K_{im}K_j^m + K_{ij}K) \quad (1.3)$$

$$0 = R + K^2 - K_{ij}K^{ij} \quad (1.4)$$

$$0 = D^j(K_{ij} - \gamma_{ij}K) \quad (1.5)$$

where R_{ij} is the 3-Ricci tensor, R is the Ricci scalar, K is the trace of the extrinsic curvature, \mathcal{L}_β is the Lie derivative for β , D_i is the covariant derivative compatible with the 3-metric γ_{ij} and t is the time coordinate. Indices i, j run from 1 to 3.

In these equations, known as the ADM-equations, equations (1.2) and (1.3) are evolution equations, describing how the dynamic variables γ_{ij} and K_{ij} evolve in time if they are specified on an initial three-dimensional spacelike hypersurface. Equations (1.4) and (1.5) are the Hamiltonian and momentum constraint equations respectively, imposing conditions that γ_{ij} and K_{ij} must satisfy everywhere and at all times. In principle, one need only to worry about the constraint equations on the initial hypersurface as the Bianchi identities guarantee that if they are satisfied there, they will be preserved on future slices of the evolution. Because of this, after the constraint equations have been used to construct initial data on the initial hypersurface, during the evolution they are often used only passively to check the validity of the numerical solution, this is known as free evolution. However, in more advanced formulations the constraint equations can be more actively used to control the evolution, see below.

1.1.2 Lapse and shift

As the lapse and shift functions appear in the evolution equations, they first need to be specified before a simulation can begin, however there are no restrictions on how they are chosen[†]. The freedom to choose these functions represents our freedom to choose the coordinate system and exploiting this has proved to be a very crucial and delicate point in

*See also the classical review by York[6].

[†]Other than trivial restrictions, e.g. α should be non-negative, i.e. time should advance in a positive direction.

simulations, making it one of the key problems in numerical relativity. A good choice of lapse and shift may significantly prolong the lifetime of a simulation, while bad choices may render a simulation unstable very quickly. One of the problems of finding good gauge conditions is that ideally one would like to choose conditions tailored to the simulation at hand. However, one cannot in general specify these functions without prior knowledge of the expected dynamics of the simulation. The lapse and shift must therefore be chosen dynamically as functions of the evolving geometry.

1.1.3 Boundary and initial conditions

Another problem that one needs to worry about is the choice of good boundary conditions, i.e. boundaries which correspond to the physical situation at hand and do not contaminate the domain of integration by spurious reflections which can disturb the simulated physical situation, or even worse, make the simulation unstable. As with most problems in numerical relativity, this is a highly non-trivial task, even for simple systems and in full nonlinear systems where backscattering is expected, even more so.

For black hole simulations one furthermore has to consider inner boundary conditions due to the singularities of black holes which a numerical simulation clearly will not be able to handle.

Lastly, before the simulation can be begin, initial conditions, i.e. γ_{ij} and K_{ij} , need to be specified on the initial hypersurface. The initial conditions should naturally reflect the physical situation that one wishes to simulate while satisfying the constraint equations. This, (also non-trivial) task is in itself one of the key problems in numerical relativity. For a review paper on initial data for numerical relativity, see[7].

1.1.4 Further developments

The ADM formulation sketched above is the system that has received the most attention in numerical relativity. Unfortunately, most simulations using it are not very longlived but quickly turn unstable.

However, the ADM system is by no means unique and many related 3+1 formulations can be obtained using the ADM equations as a "template". For instance, since the constraint equations should be zero, one can add arbitrary multiples of these to the evolution equations without affecting the physical solution, but the non-physical solutions, i.e. those that do not satisfy the constraints, *will* be affected. Other ways to change the system include using a different combination of variables or introducing extra variables to eliminate second order spatial derivatives.

There has been a number of attempts to formulate physical equivalent, but numerically more stable systems. So far the most successful reformulation came in 1999 when Baumgarte and Shapiro [8] showed that a reformulation of the ADM equations proposed by Nakamura, Oohara and Kojima [9] and Shibata and Nakamura[10] had superior stability properties compared to the original ADM equations. It is believed that the better stability properties of the new system, known as BSSN, is related to ADM being only weakly hyperbolic[11], whereas BSSN is strongly hyperbolic[12, 13]. The hyperbolicity of a system is important as it relates to the well posedness of a system. By well posedness one understands that solutions exist (at least locally) and are stable in the sense that small changes in the initial data produce small changes in the solution. As strongly hyperbolic systems of equations are well posed under general conditions, one often looks for such systems[1, 14].

1.2 Numerical issues

When one has decided for a given system of equations for a set of variables, adopted suitable lapse and shift functions and determined/defined initial and boundary conditions, one is in principle ready to numerically evolve the system to obtain a solution. However, the issue of numerically implementing the system still remains. Unfortunately, this is not a trivial task and many efforts in numerical relativity have been put into the development of efficient numerical techniques.

Before the system can be numerically solved, a "finite" representation of the (continuous) evolution equations must be obtained. There are different approaches to doing this, but finite difference approximations have so far been the most popular choice in numerical relativity. In a finite difference approximation (FDA), all derivative operators are replaced by discrete counterparts. The discrete operators can e.g. be obtained through formal Taylor expansions. There are an infinite number of combinations that a priori can be used to approximate the original system[‡]. Unfortunately the majority of these combinations result in unstable implementations, which is often reflected in the high frequency components of the numerical solution growing without bounds.

Let

$$Lu = f \tag{1.6}$$

denote a general differential system, where L denotes some differential operator, u is a function of the independent variables, i.e. the solution of the system and f is some source function of the independent variables. We can then write the FDA equivalent of the general differential system as:

$$L_{\Delta x}u_{\Delta x} = f_{\Delta x} \tag{1.7}$$

where $u_{\Delta x}$ is the discrete solution, $f_{\Delta x}$ is the specified function evaluated on the finite-difference mesh, $L_{\Delta x}$ is the finite-difference approximation of L and Δx symbolise the discretization scale, i.e. the grid spacing.

Fundamental properties describing a FDA/numerical scheme are:

- **Convergence:** Assuming that the FDA is characterised by a single discretization scale h , the approximation converges if $u_{\Delta x} \rightarrow 0$ as $\Delta x \rightarrow 0$. Operationally, convergence is clearly the main concern when constructing a FDA and is not only desirable, but a fundamental requirement. One should furthermore ensure that the solution is not only converging, but converging to the desired solution, e.g. by monitoring constraint equations and physical measures.
- **Stability:** Naturally the FDA should be stable, i.e. small perturbations (which will inevitably be introduced as a result of roundoff errors in the computer) should not cause the numerical solution to grow without bounds. On the other hand, the stability requirement should not in general rule out exponentially growing modes as this may be the solution one is looking for. Quite often one can find a (necessary) stability requirement in the form of a relation between the grid spacings in the time and space directions which the discretization must satisfy as a minimum stability requirement. Such a relation between the time steps and space steps is known as a Courant condition.
- **Accuracy:** We measure the accuracy of the FDA by its truncation error, $\tau_{\Delta x}$, which is defined by

$$\tau_{\Delta x} \equiv L_{\Delta x}u - f_{\Delta x} \tag{1.8}$$

[‡]A specific combination or approach to discretizing a set of equations is often being referred to as a *numerical scheme*.

where u satisfies the continuum equation (1.6). The form of the truncation error can always be computed, e.g. by using Taylor series expansions, from the finite difference approximation and the differential equations. We say that the FDA is of the p 'th order if for some integer p :

$$\lim_{\Delta x \rightarrow 0} \tau_{\Delta x} = O(\Delta x^p), \quad (1.9)$$

Generally it is desirable to use a FDA of the highest possible order as this gives a faster convergence rate and yield more accurate results for a given grid spacing. However, this has to be balanced with the computational cost of the FDA.

- **Dispersion and dissipation:** We are interested in the dispersion and dissipation properties of the FDA, i.e. how fast wavepackets travel as a function of wavenumber/frequency and whether they are amplified or damped respectively. As discussed below, the dissipation properties are especially important as they are closely connected to the stability of the FDA.
- **Computational cost:** Finally, it is desirable that the FDA has a low computational cost, i.e. we desire that a solution with a given accuracy can be found using as few computational resources as possible or conversely that a given grid resolution optimises the accuracy. Within the last decade, advanced computational techniques such as adaptive mesh refinements, multigrid techniques and parallelism of codes have significantly contributed to reducing computational cost, making numerical codes more efficient. However, computational resources are (still) not unlimited and it is practically always desirable to construct the FDAs to be as cost-effective as possible unless the problem at hand is very simple.

These are the main properties which characterise a FDA. Some of the properties are absolutely crucial (stability and convergence), while others are "only" desirable (accuracy, dispersion and computational cost). The accuracy and dispersion properties of a (sensible constructed) FDA can always be improved by using a higher resolution, but the task of the numerical engineer is to construct the FDA in such a way that these properties are "good enough" for as low computational cost as possible. Finally there are the dissipation properties which in some ways lie in between necessary and desirable properties. Generally, we are interested in the FDA simulating the dissipation properties of the continuous equations as closely as possible, especially for wavelengths/frequencies which are well resolved on the discrete grid. However, for wavelengths lying near the Nyquist frequency[§] it is often, especially when treating nonlinear systems, desirable to tailor the FDA in such a way that some amount of dissipation is introduced[15] at the highest frequencies. This is because random numerical noise arises at the Nyquist frequency and numerical instabilities are often first seen at this frequency. Furthermore, in a nonlinear FDA, energy may be transferred between different wavelengths, which may trigger instabilities at the Nyquist frequency or noise at this frequency may disturb the solution at other frequencies. However, by tailoring the FDA in such a way that a small amount of damping is introduced near the Nyquist frequency, one may remove/smooth out random noise introduced to the system before the simulation is contaminated by it or before it has time to produce numerical instabilities which would crash the simulation. However, for the well resolved wavelengths, which describe the solution we are looking for, we naturally wish that the dissipation and dispersion properties match the continuous differential equation as closely possible.

[§]I.e. the highest possible representable frequency for a given resolution/grid spacing corresponding to two grid points per wavelength. If the grid spacing is Δx the wave number at the Nyquist frequency is thus: $k = \frac{\pi}{\Delta x}$.

It is, in principle, possible to investigate most of the properties mentioned above before a FDA is put to use. An important tool in this respect is the Von Neumann analysis, which can be used to find the stability, dissipation and dispersion properties numerical of a given FDA and textbooks on numerical analysis are filled with examples of this (e.g. [16, 17]). The key idea of the Von Neumann analysis is to split up the solution into a linear combination its Fourier modes. The time evolution of each mode can then be analysed and the properties of the scheme can be learned as a function of the wavelengths of the solution and the parameters of the FDA (e.g. discretization scales).

For a linear equation, where the frequency modes do not interact, the analysis depends only on the frequency of the mode to be analysed and the discretization parameters of the FDA but not on the solution itself. Because of this, the Von Neumann analysis needs only to be performed once (for each frequency component of the solution) and can be done prior to the simulation in order to know the properties of the FDA at all times and all gridpoints during the simulation.

However, formally, the Von Neumann analysis applies only to FDAs which describe linear equations and most problems, especially general relativistic problem, that need to be attacked by numerical methods are highly nonlinear. Nevertheless, it is possible to perform a Von Neumann analysis of nonlinear FDAs by locally linearising the numerical solution and in this way obtain estimates of the properties of the FDA at hand. However, in this case the Von Neumann analysis depends on the local solution and in principle one has to perform the analysis at all grid points (in space and time) throughout the simulation. Even so, a localised Von Neumann analysis can successfully be applied to learn important properties of a specific FDA.

The paper presented in the next chapter ([18]) is an example of such an analysis. In the paper the numerical properties of four different numerical schemes are studied, when applied to a) the classical scalar linear wave equation and to b) a nonlinear scalar wave equation. The nonlinear wave equation has a nonlinear term which mimics part of the nonlinearities found in equations of general relativity. Hence it is reasonable to assume that in order to function well on "real" general relativistic equations, the numerical schemes as a minimum requirement should be successful when applied to our "mock" GR-equation. The nonlinear scalar wave equation used in this paper has also been employed in other papers for similar test purposes[19].

References for Chapter 1

- [1] M. Alcubierre, 'The status of numerical relativity', gr-qc/0412019 (2004).
- [2] L. Lehner, *Class. Quant. Grav.* **18**, 17 (2001).
- [3] R. M. Wald, *General Relativity* (University of Chicago Press, 1984).
- [4] Y. Bruhat, *Acta Mathematica* **88**, 141 (1952).
- [5] R. Arnowitt, S. Deser, and C. W. Misner, *Gravitation: An Introduction to Current Research* (John Wiley & Sons, Inc., New York, 1962), chap. The Dynamics of General Relativity.
- [6] J. W. York, in *Sources of Gravitational Radiation*, edited by L. L. Smarr (Cambridge University Press, Cambridge, UK, 1979), pp. 83–126, ISBN 0-521-22778-X.
- [7] G. B. Cook, *Living Reviews in Relativity* **3**, 5 (2000), <http://relativity.livingreviews.org/Articles/lrr-2000-5/>.
- [8] T. W. Baumgarte and S. L. Shapiro, *Phys. Rev.* **D59**, 024007 (1999).
- [9] T. Nakamura, K. Oohara, and Y. Kojima, *Progress of Theoretical Physics Supplement* **D90**, 1 (1987).
- [10] M. Shibata and T. Nakamura, *Phys. Rev.* **D52**, 5428 (1995).
- [11] S. Frittelli and R. Gomez, *J. Math. Phys.* **41**, 5535 (2000).
- [12] H. Beyer and O. Sarbach, *Phys. Rev.* **D70**, 104004 (2004).
- [13] O. Sarbach, G. Calabrese, J. Pullin, and M. Tiglio, *Phys. Rev.* **D66**, 064002 (2002).
- [14] H. O. Kreiss and J. Lorentz, *Initial-Boundary Value Problems and the Navier-Stokes Equations* (Academic Press, New York, 1989).
- [15] H. Kreiss and J. Oliger, *Methods for the approximate solution of time independent problems* (GARP Publication Series, Geneva, 1973).
- [16] R. D. Richtmeyer and K. Morton, *Difference Methods for Initial-Value Problems* (Wiley, New York, 1967), 2nd ed.
- [17] B. Gustafsson, H. O. Kreiss, and J. Oliger, *Time dependent problems and difference methods* (Wiley, New York, 1995).
- [18] J. Hansen, A. Khokhlov, and I. Novikov, *Int. J. Mod. Phys.* **D13**, 961 (2004).
- [19] A. Khokhlov and I. Novikov, *International Journal of Modern Physics* **D13**, 1889 (2003).

Chapter 2

Properties of Four Numerical Schemes Applied to a Nonlinear Scalar Wave Equation with a GR-type Nonlinearity

By:

Jakob Hansen*, Alexei M. Khokhlov[†] and Igor D. Novikov*^{‡,§}

Published in:

International Journal of Modern Physics D
Vol. 13. No. 5 (2004) 961-982

Abstract:

We study stability, dispersion and dissipation properties of four numerical schemes (Iterative Crank-Nicolson, 3'rd and 4'th order Runge-Kutta and Courant-Fredrichs-Levy Non-linear). By use of a Von Neumann analysis we study the schemes applied to a scalar linear wave equation as well as a scalar non-linear wave equation with a type of non-linearity present in GR-equations. Numerical testing is done to verify analytic results. We find that the method of lines (MOL) schemes are the most dispersive and dissipative schemes. The Courant-Fredrichs-Levy Non-linear (CFLN) scheme is most accurate and least dispersive and dissipative, but the absence of dissipation at Nyquist frequency, if fact, puts it at a disadvantage in numerical simulation. Overall, the 4'th order Runge-Kutta scheme, which has the least amount of dissipation among the MOL schemes, seems to be the most suitable compromise between the overall accuracy and damping at short wavelengths.

*Niels Bohr Institute, Blegdamsvej 17, DK-2100 Copenhagen, Denmark

[†]Department of Astronomy and Astrophysics, The University of Chicago,
5640 Ellis Avenue, Chicago, IL 60637, USA

[‡]NORDITA, Blegdamsvej 17, DK-2100 Copenhagen, Denmark

[§]Astro Space Center of P.N. Lebedev Physical Institute, Profsoyuznaja 83/32, Moscow 118710, Russia

2.1 Introduction

The area of numerical relativity is very complex with many factors influencing the calculations. Due to this complexity, choosing a best numerical scheme for solving problems in general relativity (GR) may be of particular importance in order to have a long term stability and to minimize truncation errors. At the same time, problems in numerical relativity usually demand a large amount of computational resources. Hence it is also desirable to choose a scheme which best exploits the available computer power at any given time, i.e. provides accurate results with a minimal number of operations.

First and foremost the scheme needs to be numerically stable, but in addition to this basic (but not always trivially established) property, there are a number of other features, such as accuracy, dissipation and dispersion properties, which may have important impacts on the numerical solutions as well.

The purpose of this paper is to investigate numerical properties (in particular dispersion, stability and dissipation) of some numerical schemes which can be used to solve GR type equations, allowing users of these schemes to estimate potential pitfalls and limitations of the schemes. The schemes that are being analyzed are the iterative Crank-Nicolson scheme (ICN), the third and fourth order Runge-Kutta schemes (RK3 and RK4) and a nonlinear version of the classical Courant-Friedrichs-Levy scheme (CFLN). A unique aspect of numerical GR is that the integration may be affected not only by stability of the scheme, but also by constraint and gauge instabilities which are intrinsic to the equations themselves. In order to separate these effects from the stability of the schemes and to investigate strengths and weaknesses of the different schemes, we want to apply the schemes to simpler scalar wave equations. Numerical schemes are usually analyzed by their application to the standard linear scalar wave equation (e.g. [1], [2]) however, they are usually applied to solve nonlinear problems. By use of a classical Von Neumann analysis, we analyze properties of the schemes applied to both the standard scalar linear wave equation and to a nonlinear scalar wave equation, which is designed to mimic some properties of the nonlinear terms in the Einstein equations. By this we hope to expand our knowledge of the behavior of the schemes in a regime which is closer to the computational reality of numerical GR than a sole analysis of the schemes in the fully linear regime. The non-linear wave equation, a perturbation analysis of it and the numerical schemes are presented in section 2.2. The results from the Von Neumann analysis of the schemes applied to the scalar linear and nonlinear wave equations are presented in section 2.3 and 2.4 respectively. To support the analytic results, numerical results are presented in section 2.5.

2.2 Formulation of the problem

In this section we present the numerical schemes which we will analyze in subsequent sections, the non-linear scalar wave equation to which we will apply the schemes and the method by which we will be analysis the schemes.

2.2.1 A Non-linear Wave Equation

Consider the following scalar, quasi-linear, hyperbolic partial differential equation of two independent variables, t and x ([3]):

$$\frac{\partial^2 g}{\partial t^2} = \frac{\partial^2 g}{\partial x^2} - \frac{1}{g} \left(\frac{\partial g}{\partial t} \right)^2 \quad (2.1)$$

or cast into first order form:

$$\frac{\partial g}{\partial t} = K, \quad \frac{\partial K}{\partial t} = \frac{\partial^2 g}{\partial x^2} - \frac{(K)^2}{g} \quad (2.2)$$

This equation is essentially the standard scalar wave equation with an added non-linear term. The equation is interesting because the non-linear term mimics part of the non-linearities present in GR equations. This can be seen by recalling that the structure of a Ricci tensor R_{ab} is

$$R \sim \sum \partial \Gamma + \sum \Gamma \Gamma,$$

where Christoffel symbols $\Gamma \sim g^{-1} \partial g$, and g is the metric. Thus R_{ab} can be represented as a sum of the terms

$$R \sim \sum g^{-1} \partial^2 g + \sum g^{-2} (\partial g)^2.$$

Equation (2.1) thus mimics a type of non-linearity present in GR equations $R_{ab} = 0$. Especially equations (2.2) resembles the evolutionary part of GR equation in a standard ADM 3+1 form (with zero shift and constant lapse). We expect that in order to successfully apply the schemes to GR equations they must be applicable to equation (2.1).

Equation (2.1) posses a large number of non-trivial solutions [3]. For test purposes we use two particular analytical solutions to this equation: A spatial constant solution:*

$$g(t) = \sqrt{C_1 + C_2 \cdot t}, \quad (C_1 + C_2 \cdot t \geq 0). \quad (2.3)$$

and an exponential solution:†

$$g(x, t) = \exp \left(\pm \sqrt{C} \cdot x \pm \sqrt{\frac{C}{2}} \cdot t \right), \quad (C \geq 0, \pm \text{ signs independent}). \quad (2.4)$$

2.2.2 Perturbation analysis

We wish to analyze the analytical behavior of small amplitude perturbations of solutions (2.3) and (2.4).

Let $g_0(x, t)$ be a base solution of equation (2.1) and let $g_0 + \tilde{g}$ be a perturbed solution, with $|\tilde{g}| \ll |g_0|$. We linearize (2.1) around g_0 and obtain a linear equation for the perturbations

$$\frac{\partial^2 \tilde{g}}{\partial t^2} = \frac{\partial^2 \tilde{g}}{\partial x^2} - 2 \left(\frac{1}{g_0} \frac{\partial g_0}{\partial t} \right) \frac{\partial \tilde{g}}{\partial t} + \left(\frac{1}{g_0} \frac{\partial g_0}{\partial t} \right)^2 \tilde{g} \quad (2.5)$$

or

$$\frac{\partial^2 \tilde{g}}{\partial t^2} = \frac{\partial^2 \tilde{g}}{\partial x^2} - 2A \frac{\partial \tilde{g}}{\partial t} + A^2 \tilde{g} \quad (2.6)$$

where

$$A \equiv \frac{1}{g_0} \frac{\partial g_0}{\partial t} \quad (2.7)$$

Consider perturbations of the form:

$$\tilde{g} \propto e^{I\omega t - I k x}. \quad (2.8)$$

* $g(t) = -\sqrt{C_1 + C_2 \cdot t}$ is naturally also a solution but since we are trying to mimic some features of the Einstein equations, g (which mimics the 3-metric of the general relativity) cannot be negative. This is also why we require $C_1 + C_2 \cdot t \geq 0$ as we would otherwise obtain complex solutions which would be unphysical.

† C cannot be negative as this would create complex solutions (see previous footnote).

where $I = \sqrt{-1}$. Then the dispersion relation is

$$\omega^2 = k^2 + 2AI\omega - A^2. \quad (2.9)$$

Substituting $\omega = \omega_R + I\omega_I$ into equation (2.9) and separating real and imaginary parts we obtain:

$$2I\omega_R\omega_I = 2IA\omega_R \quad (2.10)$$

$$\omega_R^2 - \omega_I^2 = k^2 - 2A\omega_I - A^2 \quad (2.11)$$

From (2.10) it follows that $\omega_I = A$, hence the growth rate of a perturbation $\tilde{g} \propto e^{I\omega_I t}$ is

$$\tilde{g} \propto e^{-At}. \quad (2.12)$$

We see that a base solution is stable if $A \geq 0$ and otherwise it is unstable. Hence growing solutions are stable and decaying solutions are unstable.

Due to a local linearization involved in the above analysis, the conclusion is strictly valid for perturbations with high wave numbers $k = \frac{2\pi}{\lambda}$ compared to the base solutions, and only if the growth rate is \gg then that of the base solution. By looking at the spatial constant base solution (2.3), perturbed by a spatial constant perturbation ($k = 0$), we can estimate the behavior of spatial constant or very long wavelength perturbations.

Consider a spatial constant base solution (2.3) perturbed by a small spatially constant perturbation: $g(t) = g_0(t) + \tilde{g}(t)$. Then equation (2.5) simplifies to an ordinary differential equation which can be solved to yield:

$$\tilde{g}(t) = \pm \frac{K}{2} \left(\frac{\sqrt{2}}{g_0(t)} + \frac{g_0(t)}{\sqrt{2}} \right) \quad (2.13)$$

where K is an arbitrary integration constant. From (2.13) we see that for growing base solutions (i.e positive C_2 in (2.3)) the second term is growing proportionally to the base solution, while the first term is decaying inversely proportionally to the base solution, hence the relative error is decreasing towards a constant value proportional to K . That is, the perturbation is growing but it is not unstable. If the base solution is decaying (i.e. negative C_2 in (2.3)), the first term increases rapidly as $g_0(t) \rightarrow 0$ and the solution becomes unstable as the relative error grows unbounded.

2.2.3 The Numerical Schemes

The four schemes that we are investigating are

- Iterative Crank-Nicolson
- 3'rd order Runge-Kutta
- 4'th order Runge-Kutta
- Courant-Friedrichs-Levy Nonlinear

The first three schemes are based on the method of lines approach [4], while the Courant-Friedrichs-Levy Nonlinear scheme is based on the classic central-difference, second-order explicit scheme introduced in 1928 by Courant, Friedrichs and Levy [5]. The schemes are defined as follows:

The Iterative Crank-Nicolson scheme

The iterative Crank-Nicolson scheme (ICN) is an explicit, iterative scheme which was developed by Matt Choptuik from the classic implicit Crank-Nicolson scheme [6, 7]. To solve equation (2.2), we define the ICN-scheme as follows. First the iteration process is initiated:

$$\begin{aligned} K_i^{(1)} &= K_i^n + \Delta t (\delta^2 (g_i^n) + NLT (g_i^n, K_i^n)) \\ g_i^{(1)} &= g_i^n + \Delta t \cdot K_i^n \end{aligned} \quad (2.14)$$

where $\delta^2(g_i^n) = \frac{g_{i-1}^n - 2g_i^n + g_{i+1}^n}{\Delta x^2}$ is the centered second order accurate finite difference approximation to the second order spatial derivative, g_i^n and K_i^n are determined at mesh points $x_i = i\Delta x$, $t^n = n\Delta t$ and $NLT(g_i^n, K_i^n)$ is the non-linear term (i.e for eq. (2.2) $NLT(g_i^n, K_i^n) = \frac{(K_i^n)^2}{g_i^n}$). The scheme is then iterated:

$$\begin{aligned} K_i^{(j)} &= K_i^n + \Delta t \left(\delta^2 \left(\frac{g_i^{(j-1)} + g_i^n}{2} \right) + NLT \left(\frac{g_i^{(j-1)} + g_i^n}{2}, \frac{K_i^{(j-1)} + K_i^n}{2} \right) \right) \\ g_i^{(j)} &= g_i^n + \Delta t \left(\frac{K_i^{(j-1)} + K_i^n}{2} \right) \end{aligned} \quad (2.15)$$

$j \in [2, j_{max}]$), and finally the dependent variables at the next time step are:

$$K_i^{(n+1)} = K_i^{(j_{max})}, \quad g_i^{(n+1)} = g_i^{(j_{max})} \quad (2.16)$$

As shown in [1] and [2], the optimal number of iterations, for the scalar wave equation is $j_{max} = 3^\ddagger$, which is the scheme that we will investigate in this paper. This scheme can be shown to be second order accurate in both time and space by a Taylor series expansion [1, 2].

The 3'rd order Runge-Kutta scheme

To solve eq. (2.2), the 3'rd order Runge-Kutta scheme (RK3) is defined as follows [8]:

$$\begin{aligned} K_i^{n+1} &= K_i^n + \frac{K_i^{(1)} + 4K_i^{(2)} + K_i^{(3)}}{6} \\ g_i^{n+1} &= g_i^n + \frac{g_i^{(1)} + 4g_i^{(2)} + g_i^{(3)}}{6} \end{aligned} \quad (2.17)$$

where

$$\begin{aligned} K_i^{(1)} &= \Delta t [\delta^2 (g_i^n) + NLT (g_i^n, K_i^n)] \\ g_i^{(1)} &= \Delta t [K_i^n] \\ K_i^{(2)} &= \Delta t \left[\delta^2 \left(g_i^n + \frac{g_i^{(1)}}{2} \right) + NLT \left(g_i^n + \frac{g_i^{(1)}}{2}, K_i^n + \frac{K_i^{(1)}}{2} \right) \right] \\ g_i^{(2)} &= \Delta t \left[K_i^n + \frac{K_i^{(1)}}{2} \right] \\ K_i^{(3)} &= \Delta t \left[\delta^2 \left(g_i^n - g_i^{(1)} + 2g_i^{(2)} \right) + NLT \left(g_i^n - g_i^{(1)} + 2g_i^{(2)}, K_i^n - K_i^{(1)} + 2K_i^{(2)} \right) \right] \\ g_i^{(3)} &= \Delta t \left[K_i^n - K_i^{(1)} + 2K_i^{(2)} \right] \end{aligned} \quad (2.18)$$

This scheme can be shown to be second order accurate in space and third order accurate in time by a Taylor series expansion.

[‡]Note that different authors count the number of iterations in different ways, some do not count the first step as an iteration and hence state that the optimal number of iterations is 2.

The 4'th order Runge-Kutta scheme

To solve eq. (2.2) the 4'th order Runge-Kutta scheme (RK4) is defined as follows [8]:

$$\begin{aligned} K_i^{n+1} &= K_i^n + \frac{K_i^{(1)} + 2K_i^{(2)} + 2K_i^{(3)} + K_i^{(4)}}{6} \\ g_i^{n+1} &= g_i^n + \frac{g_i^{(1)} + 2g_i^{(2)} + 2g_i^{(3)} + g_i^{(4)}}{6} \end{aligned} \quad (2.19)$$

where

$$\begin{aligned} K_i^{(1)} &= \Delta t [\delta^2 (g_i^n) + NLT (g_i^n, K_i^n)] \\ g_i^{(1)} &= \Delta t [K_i^n] \\ K_i^{(2)} &= \Delta t \left[\delta^2 \left(g_i^n + \frac{g_i^{(1)}}{2} \right) + NLT \left(g_i^n + \frac{g_i^{(1)}}{2}, K_i^n + \frac{K_i^{(1)}}{2} \right) \right] \\ g_i^{(2)} &= \Delta t \left[K_i^n + \frac{K_i^{(1)}}{2} \right] \\ K_i^{(3)} &= \Delta t \left[\delta^2 \left(g_i^n + \frac{g_i^{(2)}}{2} \right) + NLT \left(g_i^n + \frac{g_i^{(2)}}{2}, K_i^n + \frac{K_i^{(2)}}{2} \right) \right] \\ g_i^{(3)} &= \Delta t \left[K_i^n + \frac{K_i^{(2)}}{2} \right] \\ K_i^{(4)} &= \Delta t \left[\delta^2 \left(g_i^n + g_i^{(3)} \right) + NLT \left(g_i^n + g_i^{(3)}, K_i^n + K_i^{(3)} \right) \right] \\ g_i^{(4)} &= \Delta t \left[K_i^n + K_i^{(3)} \right] \end{aligned} \quad (2.20)$$

This scheme can be shown to be second order accurate in space and fourth order accurate in time by a Taylor series expansion.

Crank-Friedrichs-Levy Nonlinear scheme (CFLN)

Another approach to solving eq.(2.2) numerically is to notice that without the non-linear term, equation (2.2) is a scalar wave equation which can be solved by the classic explicit scheme by Courant, Friedrichs and Levy [5](see also cp. 10 in [7]):

$$\frac{g_i^{n+1} - 2g_i^n + g_i^{n-1}}{\Delta t^2} = \frac{g_{i+1}^n - 2g_i^n + g_{i-1}^n}{\Delta x^2} \quad (2.21)$$

We can cast this scheme into a first order form:

$$\begin{aligned} K_i^{n+\frac{1}{2}} &= K_i^{n-\frac{1}{2}} + \Delta t (\delta^2 (g_i^n)) \\ g_i^{n+1} &= g_i^n + \Delta t K_i^{n+\frac{1}{2}} \end{aligned} \quad (2.22)$$

Now, in order to use this scheme as a basis for solving equation (2.2), we must add a term to evolve the non-linear part, moreover, we wish to do this with second-order accuracy at the grid points (x_i, t^n) to ensure overall second-order accuracy of the scheme. We do this by evaluating the non-linear term using the following predictor-corrector style approach [3]:

$$\begin{aligned} \tilde{K}_i^{n+\frac{1}{2}} &= K_i^{n-\frac{1}{2}} + \Delta t \left(\delta^2 (g_i^n) + NLT (g_i^n, K_i^{n-\frac{1}{2}}) \right) \\ K_i^{n+\frac{1}{2}} &= \tilde{K}_i^{n+\frac{1}{2}} + \frac{\Delta t}{2} \left(NLT (g_i^n, K_i^{n-\frac{1}{2}}) + NLT (g_i^n, \tilde{K}_i^{n+\frac{1}{2}}) \right) \\ g_i^{n+1} &= g_i^n + \Delta t K_i^{n+\frac{1}{2}} \end{aligned} \quad (2.23)$$

This scheme can be shown to be second order accurate in both space and time by a Taylor series expansion. An advantage of the scheme is that the second-order accuracy is achieved with a relatively small number of right hand side operations, to calculate one time step CFLN requires 2 evaluations of the non-linear terms, compared to 3 evaluations required for the ICN and RK3 schemes and 4 evaluations required for the RK4 scheme. It is also noted that the scheme is staggered in time, i.e. initial values are required at points $g_{j-i,j,j+1}^n, K_i^{n-\frac{1}{2}}$.

2.2.4 The Von Neumann analysis

To investigate the properties of the numerical schemes we use a Von Neumann analysis following a standard approach [7, 9]: All the schemes can be represented by the following evolution operator:

$$U_{j,l}^{n+1} = S_{j,l}^n(U_{j',l'}^n) \quad (2.24)$$

where $U_{j,l}^n$ is a set of dynamical variables, n and j are temporal and spatial indices respectively and l enumerates the dynamic variables. In our case, the operator $S_{j,l}^n$ may depend on all components of $U_{j',l'}^n$ at grid points ($j = j - 1, j, j + 1$) corresponding to a time layer n (or a combination of n and $n - \frac{1}{2}$ in the staggered case of CFLN scheme).

Perturbing $U_{j,l}^n$ as

$$U_{j,l}^n = \hat{U}_{j,l}^n + \delta U_{j,l}^n, \quad (2.25)$$

where $\hat{U}_{j,l}^n$ is the background solution, substituting equation (2.25) into (2.24) and doing a Taylor-expansion, we obtain

$$\delta U_{j,l}^{n+1} = \sum_{j',l'} \frac{\partial S_{j,l}^n}{\partial \hat{U}_{j',l'}^n} \delta U_{j',l'}^n + O\left((\delta U_{j',l'}^n)^2\right) \quad (2.26)$$

Assuming a perturbation of the form

$$\delta U_{j,l}^n = \xi_l^n e^{-Ij\Delta x k}, \quad (2.27)$$

where $0 < k < \frac{\pi}{\Delta x}$ is the perturbation wave number and $I = \sqrt{-1}$, and substituting (2.27) into (2.26) we obtain

$$\xi_l^{n+1} \approx \sum_{j',l'} \frac{\partial S_{j,l}^n}{\partial \hat{U}_{j',l'}^n} \xi_{l'}^n e^{I(j-j')\Delta x k} \equiv G_{j,l,l'}^n \xi_{l'}^n \quad (2.28)$$

The *amplification matrix* $G_{j,l,l'}^n$

$$G_{j,l,l'}^n = \sum_{j'} \frac{\partial S_{j,l}^n}{\partial \hat{U}_{j',l'}^n} e^{I(j-j')\Delta x k} \quad (2.29)$$

holds information about properties of the numerical schemes.

For a linear finite difference equation, the amplification matrix only depends on the discretization parameters Δt , Δx and the wave number k , and needs to be calculated only once in order to know properties of the scheme at all times and grid points. For non-linear schemes the amplification matrix depends on $\hat{U}_{j,l}^n$ and must in principle be evaluated at *all* spatial points and at *all* points in time.

The generally complex eigenvalues of the amplification matrix, λ_i , hold information about the amplification and speed of a given perturbation for a single time step which can be extracted by calculating the modulus and argument of the eigenvalues respectively. The classic condition for numerical stability is that the spectral radius (i.e. the largest modulus of the

eigenvalues) of the amplification matrix is less than or equal to 1 for all wave numbers [7], however this excludes the possibility of growing exponential solutions. A less strict stability requirement (the Von Neumann stability criterion) which allows for exponentially growing solutions is that the eigenvalues must satisfy

$$|\lambda| \equiv \max_i |\lambda_i| \leq 1 + O(\Delta t) \quad (2.30)$$

for all k [7]. In this paper, we will refer to the spectral radius $|\lambda|$ as the amplification factor. We presents amplification factors as a function of $k \cdot \Delta x$ which runs in the range $k \cdot \Delta x \in [0, \pi]$ with $k \cdot \Delta x = \pi$ corresponding to the Nyquist frequency.

It should be noted that due to the local linearization involved in calculating the eigenvalues for non-linear schemes, the Von Neumann analysis is only locally valid. This also means that the analysis cannot be trusted for non-local wave modes, i.e. small wave numbers. However, we *are* most interested in high wave numbers, as experience tells us that numerical instabilities usually arises first at the Nyquist frequencies. Hence for analyzing the stability of a scheme one searches for conditions under which equation (2.30) is valid, focusing on the Nyquist frequency, which usually reduces to a restriction on the relationship between Δt and Δx , known as the Courant number $\alpha = \frac{\Delta x}{\Delta t}$.

2.3 The linear scalar wave equation

Before studying the non-linear schemes, we briefly summarize stability, dissipation and dispersion properties of the schemes applied for a scalar linear wave equation

$$\frac{\partial^2 g(x, t)}{\partial t^2} = \frac{\partial^2 g(x, t)}{\partial x^2} \quad (2.31)$$

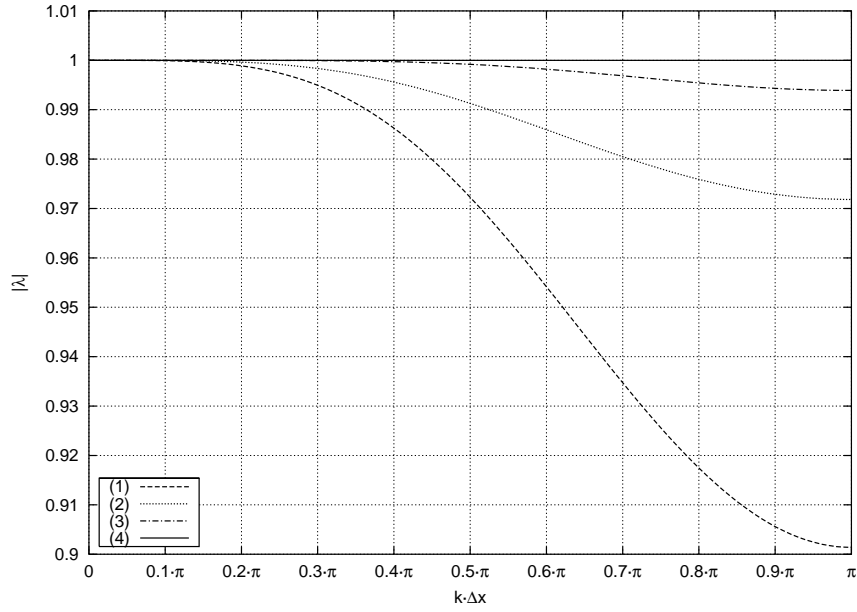
Table 2.1 shows which Courant intervals satisfies the Von Neumann stability criterion (2.30) for the Nyquist frequency as calculated by a Von Neumann analysis in the limit $\Delta t \rightarrow 0$.

Scheme	Stable Courant interval
ICN	$0 < \alpha < 1$
RK3	$0 < \alpha < \sqrt{\frac{3}{4}}$
RK4	$0 < \alpha < \sqrt{2}$
CFLN	$0 < \alpha < 1$

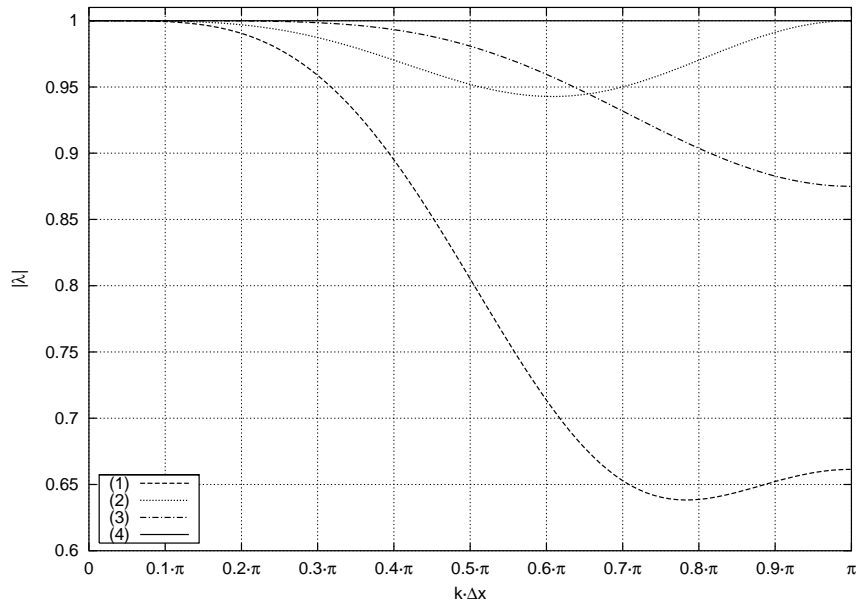
Table 2.1: Courant intervals which satisfies the Von Neumann stability criterion (2.30) for the linear wave equation (2.31)

Figures 2.1 shows the amplification factors as a function of $k \cdot \Delta x$ for Courant numbers $\alpha = 0.50$ and $\alpha = \sqrt{0.75}$ respectively, the latter corresponds to the maximal stable Courant number for the RK3 scheme (cf. table 2.1). These figures are representative of the dissipative behavior of the four schemes. The plot (and all plots in this section) is valid for all choices of Δx .

For zero wave numbers all schemes are non-dissipative, but with increasing wave numbers and increasing Courant numbers the method of lines schemes shows monotonically increasing dissipation, with ICN being the most dissipative scheme followed by the RK3 and RK4 scheme respectively. For very high wave numbers the dissipation for the method of lines



(a) Courant number $\alpha = 0.50$



(b) Courant number $\alpha = \sqrt{0.75}$

Figure 2.1: Amplification factor as a function of $k \cdot \Delta x$ at Courant number a) $\alpha = 0.50$ and b) $\alpha = \sqrt{0.75}$, respectively, for the 4 schemes investigated. Legend is (1) = ICN, (2) = RK3, (3) = RK4 and (4) = CFLN.

schemes shows a non-monotonic behavior as can be seen by comparing figures 2.1. We see that the ICN scheme is still, generally, the most dissipative scheme, but as Courant numbers are increased towards the stable limit, the dissipation at the Nyquist frequency vanishes and the maximal dissipation is seen for smaller wave numbers. Figure 2.2 shows the dissipative

behavior of the schemes at the Nyquist frequency as a function of Courant number. This shows how the Nyquist frequency has maximal dissipation at around $\alpha \approx 0.8 \cdot \alpha_{max}$ (where α_{max} is the maximal stable Courant number for the corresponding scheme), after which the dissipation at the Nyquist frequency goes to zero just before numerical instability sets in.

The CFLN scheme, in contrast, is completely non-dissipative for all wave numbers for all stable Courant numbers.

Figure 2.3 compares the dispersion errors for the four schemes for various Courant numbers as calculated from an Von Neumann analysis for equation (2.31). For small Courant numbers (fig. 2.3(a)), it is seen that the schemes behave quite similarly (in fact, for $\alpha \rightarrow 0$ the dispersion errors for the four schemes converge to the same line), but a closer examination shows that the CFLN scheme has the smallest dispersion error, then follows the RK3 and RK4 schemes respectively and finally the ICN scheme which exhibits the largest dispersion errors. Also, dispersion errors are largest for large wave numbers and going to zero in the limit $k \rightarrow 0$ for all schemes.

The dispersion errors for the ICN and RK4 schemes are increased monotonically for increasing Courant numbers at smaller wave numbers, while the dispersion errors for these schemes show some non-monotonic behavior at high wave numbers. As can be seen from figure 2.3(d), the ICN scheme in the limit of $\alpha = 1.00$ exhibits positive dispersion errors for high wave numbers, i.e. the numerical solution is propagating faster than the analytic solution[§].

The dispersion errors for the RK3 and CFLN schemes conversely are minimized for their respective maximal stable Courant numbers. The CFLN scheme in this limit has zero dispersion errors, while the RK3 still has a non-vanishing (but minimized) dispersion error.

[§]However, this is unlikely to be of numerical importance due to the high damping for ICN in the high wave number / high Courant number limit.

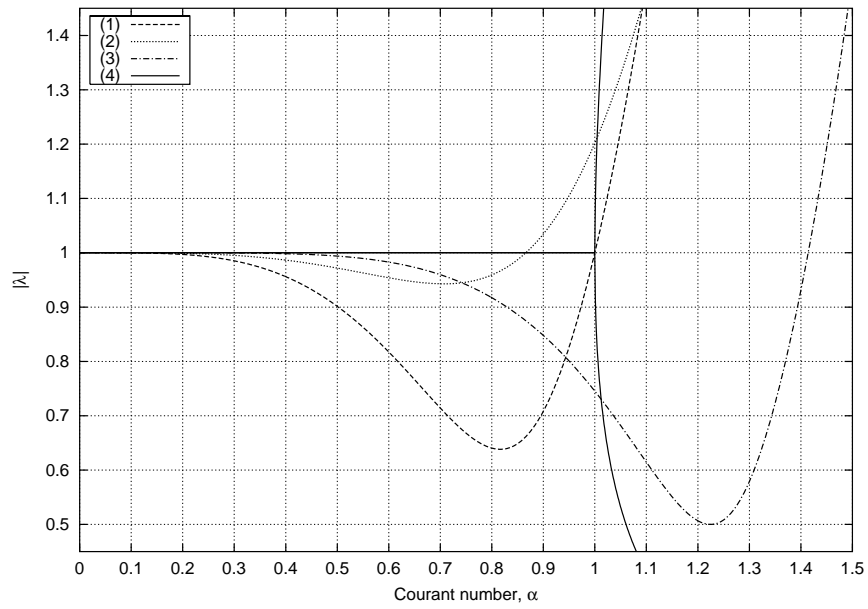
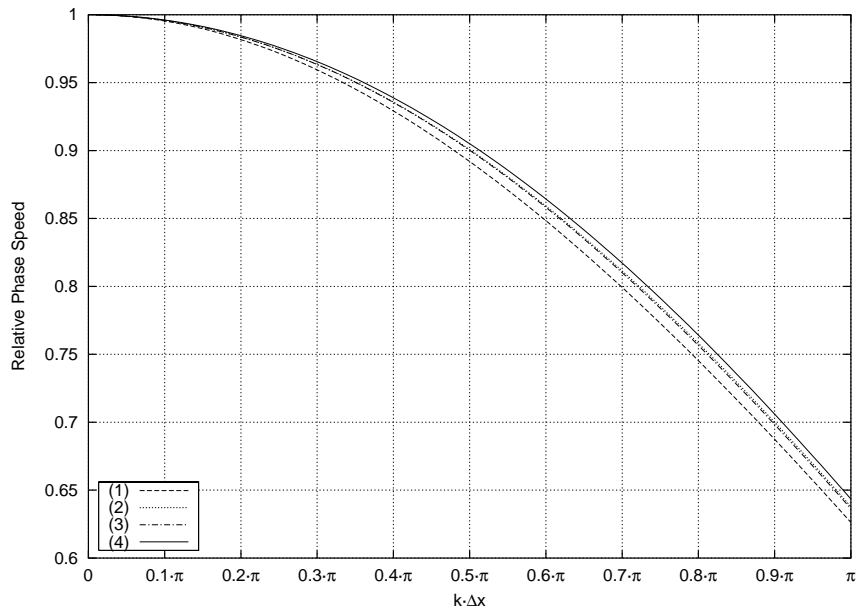
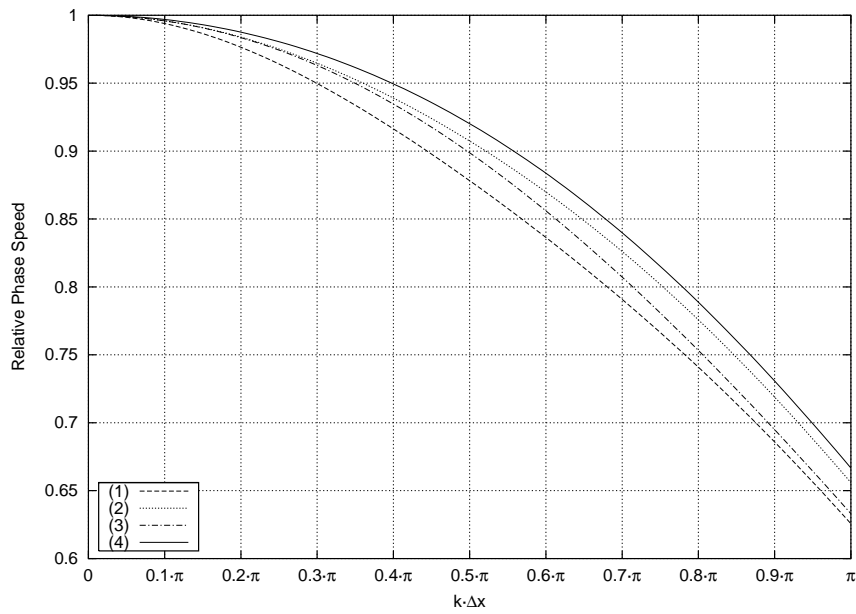


Figure 2.2: Largest eigenvalues at the Nyquist frequency ($k\Delta x = \pi$) as function of Courant numbers for the 4 schemes investigated. Legend is (1) = ICN, (2) = RK3, (3) = RK4 and (4) = CFLN.

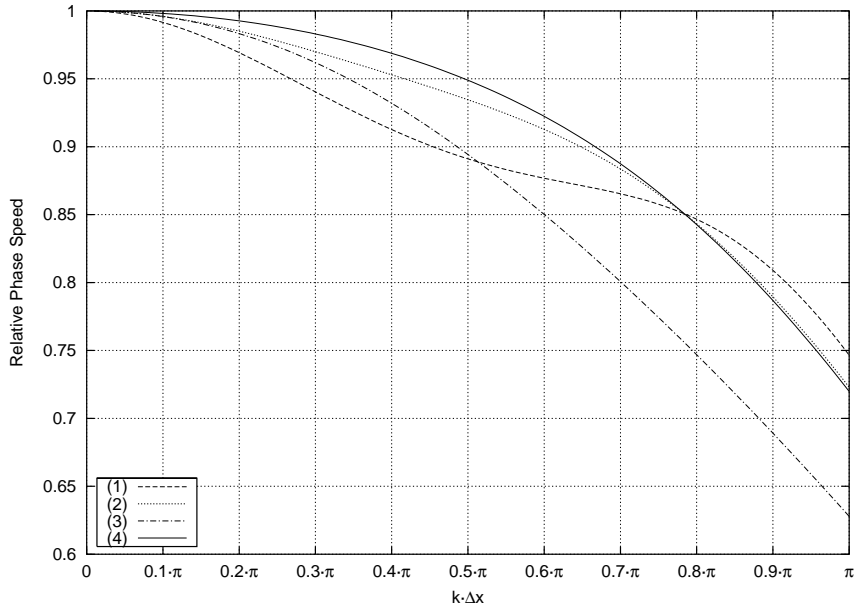


(a) Courant number $\alpha = 0.25$

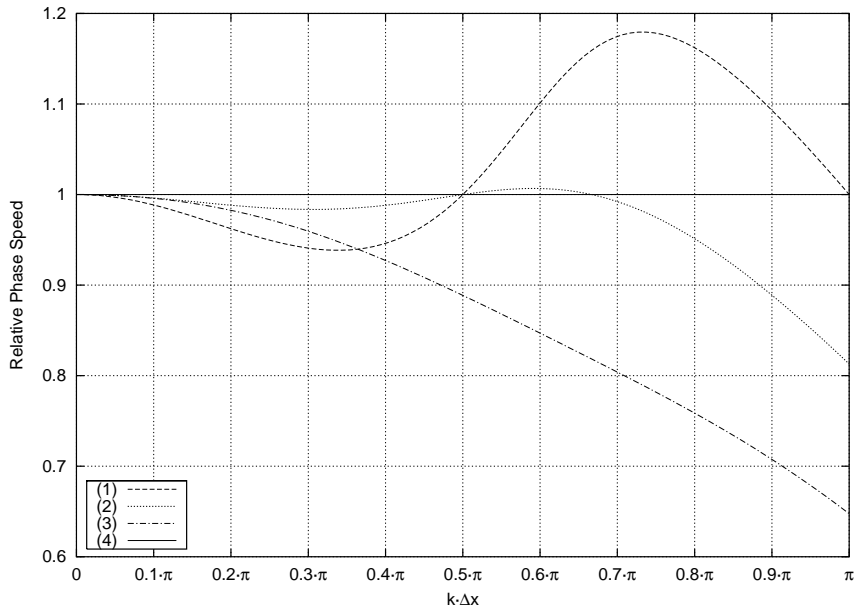


(b) Courant number $\alpha = 0.50$

Figure 2.3: Wave speeds for the four schemes for various Courant numbers relative to the analytic wave speed. Legend is (1) = ICN, (2) = RK3, (3) = RK4 and (4) = CFLN.



(c) Courant number $\alpha = 0.75$



(d) Courant number $\alpha = 1.00$

Figure 2.3: (continued)

2.4 Von Neumann stability analysis of the non-linear wave equation

We are interested in the behavior of the schemes in the non-linear regime. In this section we present the results of a Von Neumann stability analysis of the four schemes applied to a

local linearization of the non-linear wave equation, equation (2.2), presented in section 2.2.1.

2.4.1 The spatial constant solutions

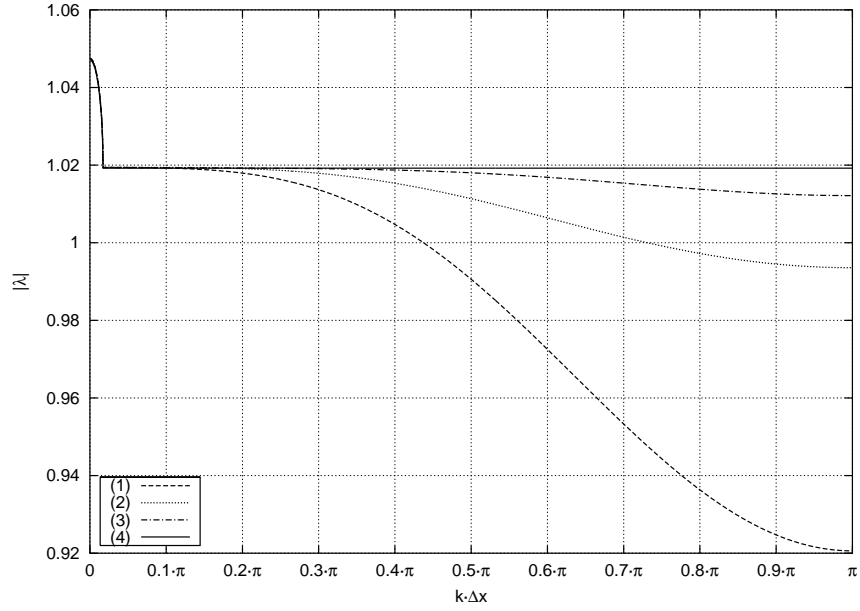
Figure 2.4 shows a typical plot of amplification factors versus $k \cdot \Delta x$ for the spatially constant solution (2.3) of equation (2.2) for decaying and growing solutions respectively, for the four schemes. Solution parameters are $C_1 = 2$ for both plots and $C_2 = -1$ and $C_2 = 1$ for figure 2.4(a) and 2.4(b) respectively. From the perturbation analysis in subsection 2.2.2 we expect to observe an amplification for all wave numbers when solution (2.3) is decaying. For growing solutions we expect to see a more modest amplification at small wave numbers and damping at higher wave numbers. Looking at figures 2.4, we observe that at small wave numbers, all schemes agree with this prediction, i.e. we see a strong amplification at small wave numbers for the decaying solution and a smaller amplification for the growing solution. At high wave numbers the CFLN scheme agrees well with the perturbation analysis and we see an amplification at the Nyquist frequency, while the method of lines schemes all show various degrees of damping, consistent with the results from section 2.3. The amount of damping is dependent on the Courant number as in the linear case, but also upon the spatial step size, Δx . By choosing a smaller Δx , for a fixed Courant number, Δt decreases proportionally, by which any amplification also becomes smaller. However, with the amplification factor moving closer to $|\lambda| = 1$, the damping for the method of lines schemes are shifted proportionally, i.e. the method of lines schemes may go from showing amplificative behavior to damping behavior at the Nyquist frequency, with the choice of a smaller Δx . We see this effect in figure 2.4(a) for the ICN scheme. If we for the same solution had chosen a sufficiently small Δx , the other method of lines schemes would also have shown damping behavior at the Nyquist frequency. The qualitative behavior of the CFLN scheme, in contrast, is unaffected by the choice of Δx for reasonably small Δx . For very large Δx , all the schemes show abnormal behavior which is caused by the fact that the base solution in this case changes much more rapidly than the temporal resolution allows for.

2.4.2 The exponential solutions

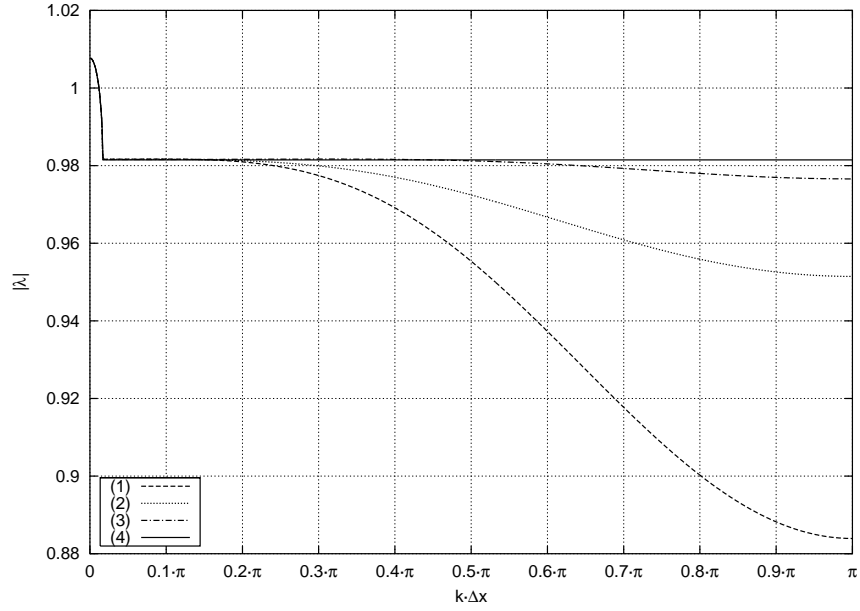
Figure 2.5 shows a typical plot of the amplification factors for the four schemes under investigation for the exponentially growing and decaying solution (2.4) to equation (2.2) as a function of $k \cdot \Delta x$ with solution parameter $C = 1$. We see that the plots are very similar to figures 2.4. For the decaying solution (figure 2.5(a)) we see that CFLN is an amplificative scheme whereas the method of lines schemes display a certain amount of damping. We note that in order to reproduce a correct behavior of perturbed analytic solutions the scheme must have the amplification number greater than one. However, in numerical simulations it may be better to damp growing large wave number (short wavelength) perturbations instead of trying to faithfully reproduce them.

For small wave numbers both the decaying and growing solutions are indicating amplificative behavior. We note that solution (2.4) is spatially dependent, hence the spatially constant perturbation analysis from subsection 2.2.2 is not valid in this regime. Nevertheless, comparing with figures 2.4 where we see (and expect) the same behavior it seems plausible that the amplificative behavior seen in the figures is an expected behavior.

As a closing remark to this section, we note that all schemes and solutions have been tested in the limit $\Delta t \rightarrow 0$ to investigate the stability properties of the schemes in the non-linear regime and we have found that all schemes agree with the stability intervals for the linear case (table 2.1) for all solutions.

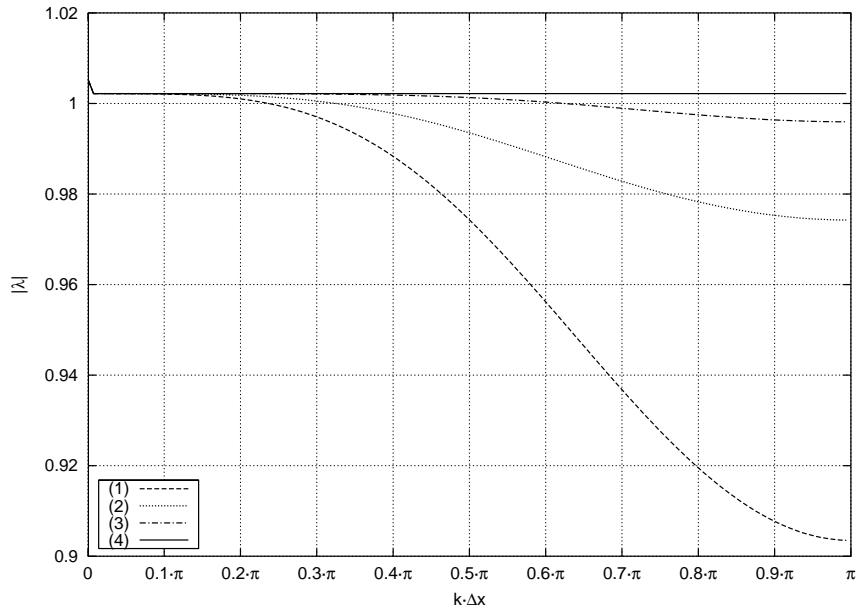


(a) Decaying solution (2.3).

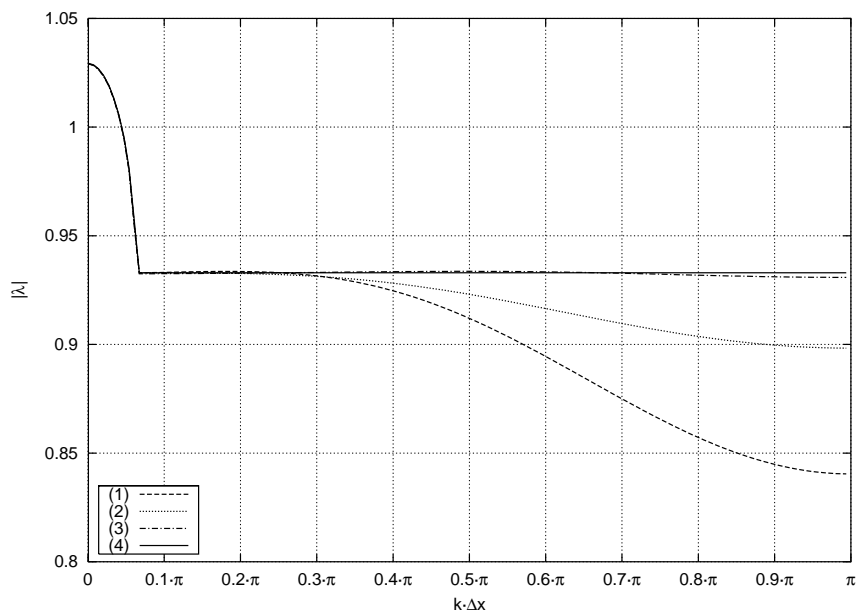


(b) Growing solution (2.3).

Figure 2.4: Amplification factors for solution (2.3) as a function of $k \cdot \Delta x$. (a) is decaying ($C_2 = -1$) and (b) is growing ($C_2 = 1$). Courant number is $\alpha = 0.5$ and $\Delta x = \frac{\pi}{16}$. Legend is (1) = ICN, (2) = RK3, (3) = RK4 and (4) = CFLN.



(a) Decaying solution (2.4)



(b) Growing solution (2.4)

Figure 2.5: Amplification factors for solution (2.4) as a function of $k \cdot \Delta x$. (a) is decaying and (b) is growing. Courant number is $\alpha = 0.5$, $\Delta x = \frac{\pi}{16}$ and $C = 1$. Legend is (1) = ICN, (2) = RK3, (3) = RK4 and (4) = CFLN.

2.5 Numerical Tests

We have done numerical testings to verify the analytic results presented in the preceding sections. Figure 2.6 shows the convergence of solution (2.3) to equation (2.2). Plotted on the vertical axis is the absolute error of the central point in the domain between a simulation with the spatial step specified on the horizontal axis and a reference simulation. The reference simulation is a high resolution simulation with a resolution twice that of the leftmost point in the plot. The constants in solution (2.3) were set to $C_1 = 2$ and $C_2 = -1$, the simulations were run for a time $t = \pi/4$ in a domain of size 2π and the Courant number of the simulations was fixed at $\alpha = 0.50$.

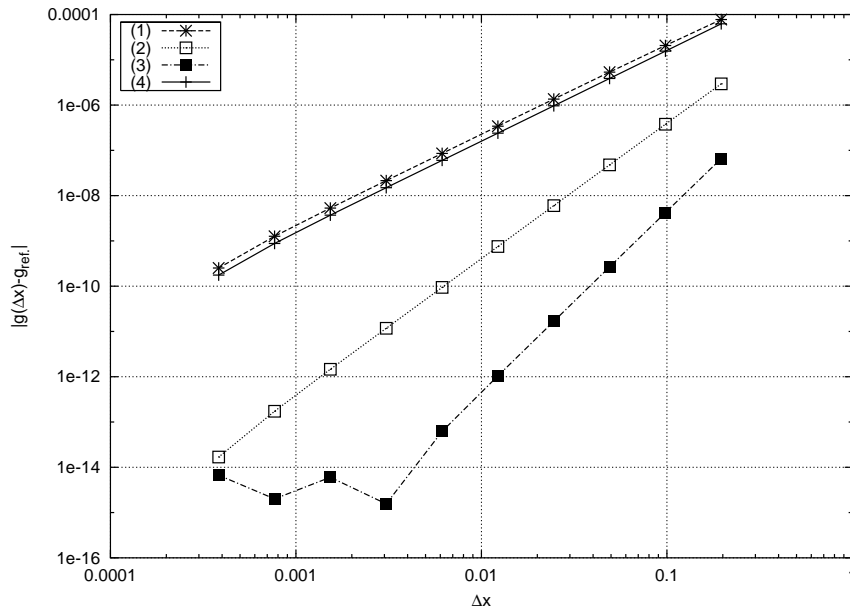


Figure 2.6: Absolute error between simulation at specified Δx vs. simulation at $\Delta x = \frac{\pi}{2^{14}}$ for Courant number $\alpha = 0.50$. Legend is (1) = ICN, (2) = RK3, (3) = RK4 and (4) = CFLN.

From the figure we see that the CFLN and ICN schemes are showing second order convergence, the RK3 scheme shows third order convergence. The RK4 scheme shows fourth order convergence at large Δx , but flattens out around 10^{-15} and for small step sizes. The flattening is caused by machine precision errors affecting the solutions. The convergence rates are what should be expected for spatially constant solutions. This solution does not introduce any truncation errors associated with spatial discretization. The figure thus shows convergence rates in agreement with the truncation error due to the temporal discretization of the schemes (second order CFLN and ICN, third order RK3, and fourth order RK4). Identical convergence tests for the exponential solutions (2.4) shows second order convergence for all schemes due to the second order spatial finite difference operator we have used in the schemes to calculate spatial derivatives.

To test analytic predictions of the behavior of a perturbed solution we have made numerical tests of base solutions perturbed by small amplitude sinusoidal perturbations, $g(x, t) = g_0(x, t) + \tilde{g}(x, t, k)$, with wave number k . Figure 2.7 is identical to figure 2.6, except that now base solution (2.3) is perturbed by a moving sinusoidal wave with wave number of $k = 16$ (corresponding to the Nyquist frequency for the rightmost point) and initial amplitude $A_0 = 10^{-6}$, all other parameters are as for figure 2.6.

We see from the figure that the perturbed solution is converging for all schemes. For

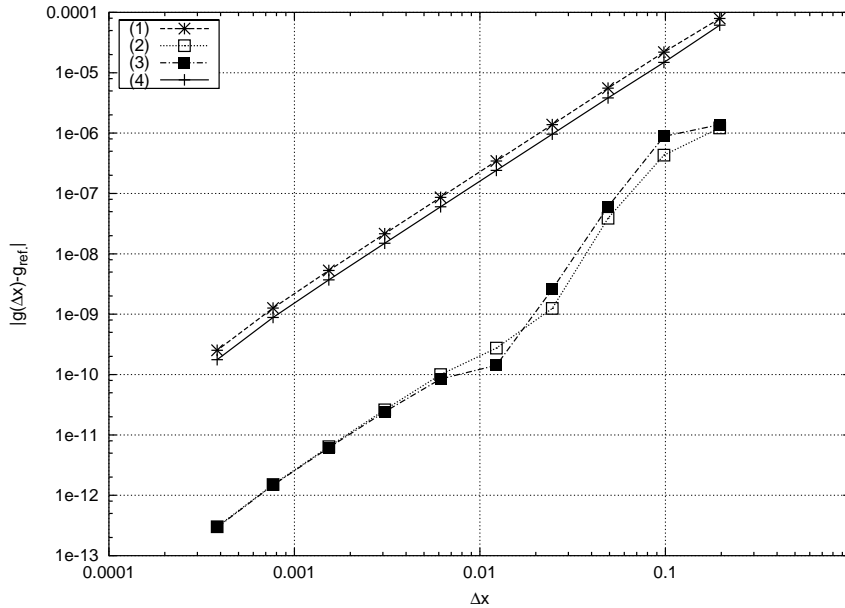


Figure 2.7: Absolute error between perturbed simulation at specified Δx vs. simulation at $\Delta x = \frac{\pi}{2^{14}}$ for Courant number $\alpha = 0.50$. Perturbation is a moving sinusoidal wave with wave number $k = 16$ and initial amplitude $A_0 = 10^{-6}$. Legend is (1) = ICN, (2) = RK3, (3) = RK4 and (4) = CFLN.

higher resolutions the convergence is at least second order. Similar convergence rates are seen for analogous simulations with other base solutions.

Figure 2.8 shows the ratio of the final amplitude (A_t) of a perturbation at time $t = \pi/4$ to its initial amplitude ($A_0 = 10^{-6}$) as a function of the resolution of the perturbed wave for simulations with base solution 2.3 with $C_1 = 10$ and $C_2 = -1$. Courant $\alpha = 0.50$ and $\Delta x = \frac{\pi}{2^{13}}$ was used in all simulations. The rightmost data point corresponds to a perturbation being at the Nyquist frequency. The analytical prediction is that

$$\frac{A_{t=\pi/4}}{A(0)} = \exp\left(-\frac{C_2 \cdot t}{2C_1 - 2C_2 \cdot t}\right) \approx 1.0435$$

according to (2.12). This prediction is also shown on the figure as line (0).

From this figure we see that at high resolutions all schemes produce the same growth of amplitude of perturbations, which is in agreement with the analytical prediction. As the resolution decreases the results for all schemes for all schemes begin to deviate from the analytical value. Among the method of lines schemes, the RK4 is the most accurate and is able to reproduce the correct behavior of the perturbation up to the resolution of 16 grid points per wavelength. CFLN also requires only 16 grid points per wavelength to reproduce the correct behavior. The other two schemes requires from 32 to 64 grid points per wavelength. The major difference between the CFLN and the method of lines schemes is that at low resolutions, CFLN is amplifying the perturbations more than it should according to the analytical predictions, whereas the method of lines schemes are damping. The RK4 is the least damping and the most accurate of these schemes. The behavior of the schemes at low resolutions is fully consistent with the results of the Von Neumann stability analysis, presented in section 2.4.1. According to that analysis the CFLN scheme must be amplifying at all wavelengths whereas the method of lines schemes must be damping.

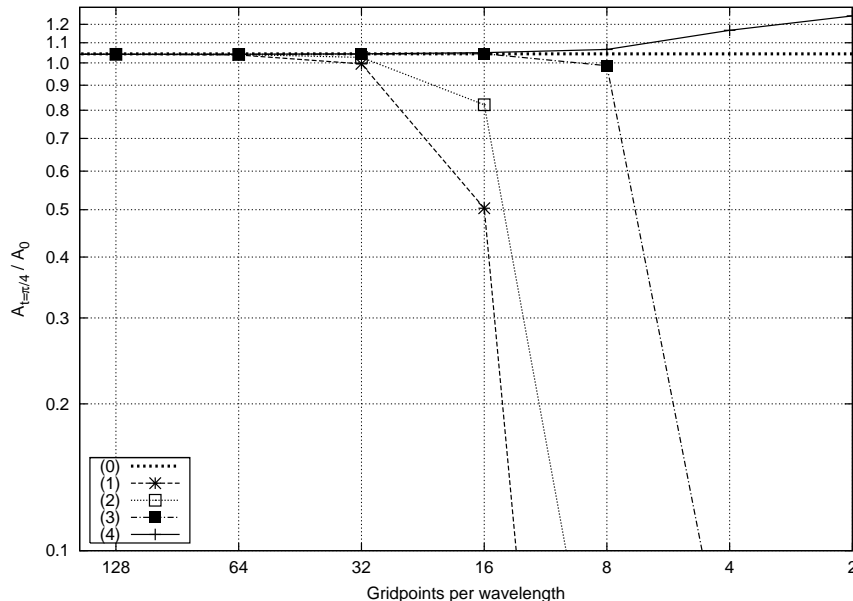


Figure 2.8: A_t/A_0 of sinusoidal perturbation at $t = \pi/4$ for base solution (2.3) versus various wave numbers for a fixed $\Delta x = \frac{\pi}{2^{13}}$ and $\alpha = 0.50$. Legend is (0) = Analytic prediction, (1) = ICN, (2) = RK3, (3) = RK4 and (4) = CFLN.

2.6 Discussion and conclusion

In this paper we studied the properties of four numerical schemes, CFLN, ICN, RK3 and RK4, applied to a non-linear scalar wave equation (2.1). This equation has a number of non-trivial analytic solutions whose properties, including stability, were studied and summarized in section 2.2. We carried out the Von Neumann stability analysis of the schemes and studied their phase and amplitude errors. Finally we carried out numerical experiments and compared the results of those experiments with the perturbation analysis of the equation and the Von Neumann stability analysis of the schemes.

We find that all four schemes presented in this paper are stable and converge with the second order accuracy. The stability range for the schemes were determined and are presented in table 2.1. Those ranges are valid for both linear and non-linear solutions.

For non-linear schemes we checked that the amplification factor $|\lambda|$ is less than $1 + O(\Delta t)$ for sufficiently small Δt .

With respect to the dissipation errors, we find that the CFLN has the least amount of dissipation. The ICN scheme has the largest dissipation errors. The RK3 and RK4 are intermediate. For the method of lines schemes we find that damping is behaving non-monotonically with the increase of the Courant number.

With respect to phase errors, the schemes can be arranged in the sequence CFLN RK3, RK4 and ICN, with the CFLN having the least amount of errors and ICN having the largest.

We find that CFLN scheme requires the least amount of operations per time step, whereas the RK4 requires the largest amount.

Ideally a numerical scheme is preferable which has the minimal phase and amplitude errors, and is computationally inexpensive. It is also of practical importance to have a scheme which will damp the high frequency perturbations at and close to the Nyquist frequency. Otherwise truncation errors at the highest frequency will remain within the computational domain, may be amplified and may eventually spoil the solution. None of the schemes

discussed in this paper satisfy all those criteria. We think that the RK4 scheme should be preferred to other schemes because of its damping properties at the Nyquist frequency and the minimal amount of errors consistent with this property. On the other hand, the amount of dissipation in the RK4 scheme is dependent upon Courant number and is not controllable. If not for the damping properties, the CFLN scheme is the most accurate and cost effective. It would be of great interest to develop a version of this scheme with a controllable filter, for damping the minimum amount of perturbations at a narrow range of frequencies near the Nyquist frequency.

2.7 Acknowledgements

This work was supported in part by Danmarks Grundforskningsfond through its support for establishment of the Theoretical Astrophysics Center and by the Danish SNF Grant 21-03-0336. We thank A. Doroshkevich and R. Takahashi for useful discussions. The authors thank Caltech for hospitality during their visits.

References for Chapter 2

- [1] M. Alcubierre *et. al.*, *Phys. Rev.* **D62**, 044034 (2000).
- [2] S.A. Teukolsky, *Phys. Rev.* **D61**, 087501 (2000).
- [3] A. Khokhlov and I.D. Novikov, *Int. J. Mod. Phys.* **D12**, 1889 (2003).
- [4] B. Gustafsson, H. O. Kreiss and J. Olinger, *Time dependent problems and difference methods* (Wiley, New York, 1995).
- [5] R. Courant, K. O. Friedrichs and H. Levy, *Math. Ann.* **100**, 32 (1928).
- [6] J. Crank and P. Nicolson, *Proc. Cambridge Philos. Soc.* **43**, 50 (1947).
- [7] R. D. Richtmeyer and K.W. Morton, *Difference Methods for Initial-Value Problems*, 2nd edn. (Wiley-Interscience, New York, 1967).
- [8] M. Abramowitz and I .A. Stegun, *Handbook of Mathematical functions*, (Dover, 1965).
- [9] M. Miller, On the Numerical Stability of the Einstein Equations (2000), gr-gc/0008017.

Part II

Physical Studies

Chapter 3

Internal structure of black holes

The formation of a realistic black hole from the collapse of a massive star is a highly dynamical process. In the collapse, any deviation from a spherical state will be emitted as gravitational waves and the external gravitational field will quickly settle down to a stationary state, a Kerr black hole*. In the case of any subsequent external perturbations of the black hole, an analogous result is valid and the perturbed black hole will quickly return to a Kerr state.

However, the details of how the internal geometry reacts to perturbations are not fully understood. This problem has been an area of active analytical and numerical researches, which have received an increasing amount of attention in recent decades. It is now clear that the internal geometry will *not* relax to a Kerr form when perturbed, but the details of the physical processes occurring in the interior of the perturbed black hole is still a partly unsolved problem. In this chapter, some of the most important physical processes will briefly be presented. For a more thorough overview of the problems of the internal structure of black holes see e.g. [1, 2] and references therein.

3.1 Analytic solutions

If we consider an eternal black hole placed in an asymptotically flat and (apart from the black hole) empty spacetime, it is quite straightforward to analytically extend the metrics of known analytical black hole solutions to their interiors by choosing proper sets of coordinates[1].

Of particular interest is the extension of the Kerr metric as realistic astrophysical black holes are believed to be externally described by this metric. As it turns out, the internal causal structure of the analytic Kerr and Reissner-Nordström spacetimes are very similar, in particular both of these solutions possess a Cauchy horizon in their interior, i.e. a surface beyond which spacetime is unpredictable. Due to the similarity of the two geometries, it has been argued that the key physics underlying the analysis of a spherical charged black hole is sufficiently general and that similar results should hold for generic collapse of a rotating body without spherical symmetry[3]. Based on this assumption, most work on the internal structure of black hole, including the work presented in this part of the thesis, has been done in the framework of spherical electrically charged black holes.

In fig. 3.1 is sketched the Penrose diagram for a typical Reissner-Nordström black hole. As in the Schwarzschild case, this black hole possess an external event horizon, r_+ , where the radius r switches from being a spacelike coordinate to a timelike coordinate and past which

*In the general case a Kerr-Newman black hole, however realistic black holes are not expected to possess any significant electric charge.

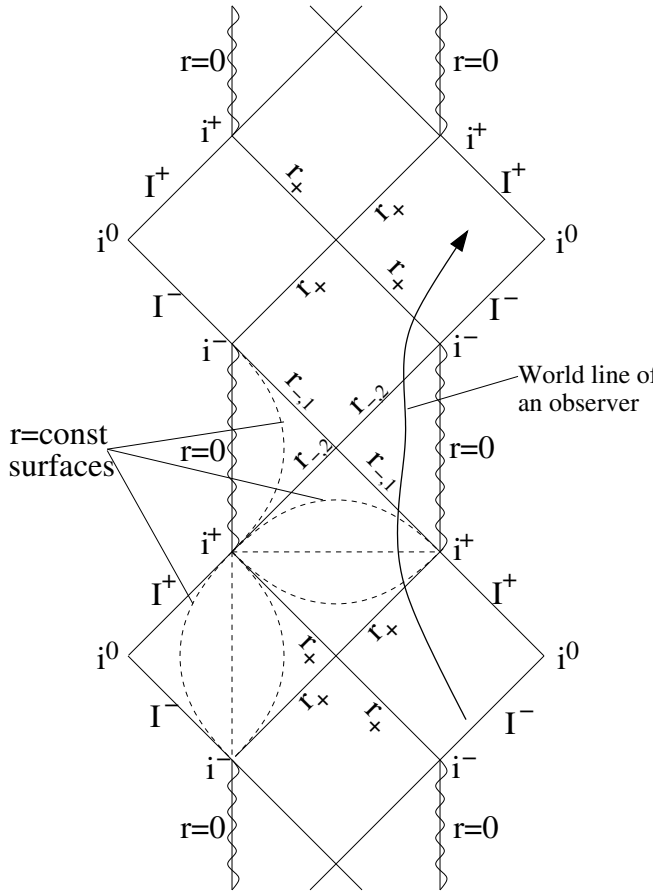


Figure 3.1: Penrose diagram of a typical Reissner-Nordström spacetime.

an observer must necessarily move in the direction of decreasing r . However, unlike in the Schwarzschild case, the observer is not doomed to crash into a spacelike $r = 0$ singularity, but will continue his journey from r_+ to ever-decreasing radii only until he reaches the Cauchy horizon, $r_{-,1}$ or $r_{-,2}$, where r switches back to being a spacelike coordinate and the motion in the direction of decreasing r can be arrested. Therefore the observer can avoid the (timelike) $r = 0$ singularity, and may begin to move in the direction of increasing r through a second Cauchy horizon, where r once again becomes a timelike coordinate, but with reversed orientation, and the observer will be forced to move in the direction of ever-increasing r . Eventually, this observer will travel past $r = r_+$ once more and exit from a white hole into another (but similar) universe.

This has inspired theoreticians (as well as science-fiction writers) on the possibility of using black holes as a portal for hyperspace travel. Naturally, it would be most interesting to know if a Cauchy horizon exists in realistic black holes and whether it, in principle, would be possible for an extended physical object to travel through it. There are, however, serious conceptual problems with the existence of a Cauchy Horizon as the part of spacetime lying beyond it is in causal connection with the $r = 0$ singularity whereby predictability is lost. Furthermore, as will be described below, violent physical processes takes place near the Cauchy Horizon in more realistic scenarios, which may destroy the Cauchy horizon.

3.2 Physical phenomena

While the internal structure described above is most interesting, it is also very unrealistic as it describes a highly idealised scenario in which a single black hole exists eternally in an (apart from the black hole) empty and asymptotically flat spacetime without any external disturbances. However, in a realistic scenario where the black hole is influenced by external perturbations, important physical phenomena occur in the interior of the black holes.

3.2.1 Ingoing fluxes

A realistic black hole may be created as a result of the collapse of a massive star. After such a collapse, the exterior of the black hole will quickly settle down to a stationary state. Any deviation from this state will be radiated away as gravitational radiation which interacts with the spacetime curvature near the black hole and while most of it escapes to infinity, part of it will be backscattered into the black hole. This backscattered radiation will exist along the event horizon as a dying tail of gravitational radiation[4]. Furthermore, the black hole will also be influenced by other sources of radiation from the surrounding universe, e.g. cosmic microwave background radiation.

It can be shown that an observer following a timelike world line crossing the Cauchy horizon $r_{-,1}$, will do so in a finite amount of proper time, however, on this journey, he will encounter all the radiation that sinks into the black hole after an infinite time of an external observer. Thus, when the observer approaches $r_{-,1}$, the radiation he receives has an infinite blueshift and there will be an infinite concentration of energy density near $r_{-,1}$. It is natural to expect that such a concentration of energy restructures the spacetime and produces a spacetime singularity in place of $r_{-,1}$ [5] and mathematical analyses confirm that small perturbations are indeed unstable near $r_{-,1}$ [6].

Using the charged Vaidya metric[7, 8] to model an radial ingoing lightlike flux which is not backscattered by the background curvature inside the black hole, we can analyse the situation in greater detail. The result of this analysis confirms that a freefalling observer measures an infinite energy density when he comes to the Cauchy horizon. However, the analysis also reveals that the metric is perfectly regular at and near the Cauchy horizon and that the tidal forces will remain finite in the reference frame of the observer as he crosses the Cauchy horizon[3]. This singularity situated along the Cauchy horizon is a weak so-called “whimper” singularity[9, 10].

3.2.2 Simultaneous in- and outgoing fluxes

The picture gets more complicated if we consider the simultaneous coexistence of in- and outgoing fluxes inside the black hole near the Cauchy horizon. Outgoing fluxes originate from the surface of objects collapsing to form black holes, but most of this radiation falls down into the singularity not far from the collapsing star and does not have a great influence on the Cauchy Horizon[1]. A more important source of outgoing radiation is the scattering of infalling radiation inside the black hole on an internal potential barrier around the radius $r_b = e^2/m$ [1].

A consequence of the simultaneous existence of in- and outgoing fluxes near the Cauchy horizon is a tremendous growth of the black hole internal mass parameter[†], a phenomenon which has been dubbed mass inflation [3].

[†]The internal mass parameter measures the amount of mass within a sphere as seen by an observer on the surface of the sphere.

The mechanism responsible for the mass inflation can be understood by considering a concentric pair of thin spherical shells moving with the speed of light (e.g. are made of photons) in an empty spacetime without a black hole[1, 11].

One shell of mass m_{con} contracts, while the other shell of mass m_{exp} expands. The contracting shell, which initially has a radius greater than the expanding one, does not create any gravitational effects inside it, so the expanding shell does not feel the existence of the external shell. On the other hand, the contracting shell moves in the gravitational field of the expanding one. The mutual potential of the gravitational energy of the shells acts as a debit (binding energy) on the gravitational mass energy of the external contracting shell. Before the crossing of the shells, the total mass of both of them, measured by an observer outside both shells, is equal to $m_{con} + m_{exp}$ and is constant because the debit of the absolute increase of the negative potential energy is exactly balanced by the increase of the positive energies of photons blueshifted in the gravitational field of the internal sphere.

When the shells cross one another, at radius r_0 , the debit is transferred from the contracting shell to the expanding one, but the blueshift of the photons in the contracting shell will not be affected. As a result, the masses of both spheres change. The increase of mass m_{con} is called mass inflation. An exact calculation shows that the new masses m'_{con} and m'_{exp} are [1]:

$$m'_{con} = m_{con} + \frac{2m_{con}m_{exp}}{\epsilon}, \quad m'_{exp} = m_{exp} - \frac{2m_{con}m_{exp}}{\epsilon}, \quad (3.1)$$

where $\epsilon \equiv (r_0 - 2m_{exp})$ (with units $G = c = 1$). The total mass-energy is, of course, conserved: $m'_{con} + m'_{exp} = m_{con} + m_{exp}$. If ϵ is small (the encounter is just outside the horizon of m_{exp}), the inflation of mass of m_{con} can become arbitrary large. It is important to notice that a necessary requirement for mass inflation is that in- and outgoing fluxes are present simultaneously.

This result is straightforwardly extendable to the crossing of shells inside a charged black hole. If the shells cross near the Cauchy Horizon, the blueshift of the ingoing shell may be arbitrarily large which results in a correspondingly large mass inflation.

Several investigations have confirmed this scenario. The pioneer paper by Poisson and Israel[3] (see also [12]), which used continuous fluxes to model both the in- and outgoing fluxes, also confirmed the mass inflation scenario and the presence of a mild singularity. It turns out that the main properties of mass inflation do not depend on the specific nature of the outflux, just its presence is essential. Ori[13] investigated a model with a continuous influx (imitating the "tail" of ingoing gravitational radiation obeying the Price power-law tail[4]) and the outflux in the form of a thin shell (a very rough imitation of the outgoing gravitational radiation scattered by the spacetime curvature inside the black hole). This model confirmed the mass inflation scenario near the Cauchy horizon. It was also demonstrated that even though the tidal forces in the reference frame of a freely falling observer grows infinitely, its integral along the world line of the observer remains finite, i.e. it is still possible, in principle, for a physical object to cross the Cauchy horizon. The singularity created in this scenario, though much stronger than the whimper singularity in the case of the Vaidya model, is still quite weak, a so-called mild singularity.

There is one other important effect caused by the presence of fluxes inside the black hole. If we draw the worldlines of imaginary in- or outgoing test photons they will be under the influence of the gravity of any opposite directed fluxes causing the test photons to move to smaller radii. This focusing effect will continue until the radii shrinks to $r = 0$ and a stronger singularity occurs. The contraction of the Cauchy horizon caused by outgoing fluxes has received special attention[13], but it is important to notice that the focusing effect can also create $r = 0$ singularities in regions which are not causally connected to the Cauchy horizon, thus it would be wrong to say that the contraction of the Cauchy horizon creates

a $r = 0$ singularity, but rather that it meets with one. Examples of this will be given in the next chapter [14]. An important consequence of the focusing effect is an increase of mass that occurs when a sphere is compressed due to the work of pressure forces on the surface of the sphere. Near the Cauchy horizon this mass squeeze/compression effect will be negligible compared to the mass inflation, but as we will see in the next chapter this effect can be detected in other regions of the interior of black holes.

3.2.3 Quantum effects

Finally it should be noted that quantum effects are expected to play an important role inside black holes. A number of theorems (see references in [1]) imply that singularities in the structure of spacetime develop inside black holes. Near these singularities, curvature invariants, e.g. the Kretschmann scalar $K = R_{\alpha\beta\gamma\delta}R^{\alpha\beta\gamma\delta}$ are expected to diverge. When these invariants are comparable to planckian scales, classical theory breaks down and must be replaced by a quantum theory of gravity. Unfortunately such a theory is not yet complete and any speculation of physical processes in this Planck region would be highly speculative. About different aspects of quantum effects in black holes see e.g. [1, 15, 16].

Secondly, as the essential events, mass inflation and singularity formation, happen along the Cauchy horizon which brings information from the infinite future of an external observer it is very important to know the boundary conditions of the black hole up to infinity. However, even an isolated black hole in an asymptotically flat spacetime will evaporate by emitting Hawking quantum radiation and even without going into details, it is clear that quantum evaporation of the black holes is crucial for the whole problem. Unfortunately, little is known about how the Hawking radiation affects the interior structure as well as the final (exterior) state of the radiation and most analyses blissfully ignore its presence.

3.3 More realistic models

The physical processes described in the previous section are crucial for understanding the internal structure of black holes. However, these results were found using analytical approaches relying on a number of simplifying assumptions and while there is little doubt that the main results remain valid in more realistic scenarios, the detailed study of realistic cases with complicated fluxes and nontrivial nonlinear effects is very complicated and impossible to solve analytically. This has naturally led to numerical investigations of the problem which, while still relying on some simplifying assumptions, have the capabilities to simulate more realistic spacetimes under the influence of very complicated fluxes including backscattering of fluxes and other important nonlinear effects in extended regions of the interior of black holes.

As with most analytical studies, the numerical computations usually assume that the interior structures of the Kerr and Reissner-Nordström black holes are sufficiently similar to allow studying the latter and still obtain results valid in the general case. This greatly simplifies the computations, since the Reissner-Nordström black holes, due to spherical symmetry, can be simulated in a 1+1 spacetime. On the other hand, however, the assumption of spherical symmetry also implies that one is limited to studying scalar fields in this case. It is also common to take as initial conditions a pure Reissner-Nordström black hole which is then perturbed by an influx of scalar radiation and often it is assumed that no outgoing radiation initially exists, but is only created as a consequence of scattering of the ingoing radiation.

Motivated by previous numerical studies ([17–20] and others) and by the desire to extend our knowledge and understanding of the physical processes inside black holes, we initiated research in this area. Our research is mainly based on a numerical approach, following the simplifications mentioned above. With an appropriate numerical code, we have studied the interior of black holes under the influence of compact pulses of scalar radiation. We studied both extended parts of the interior in general, but have also investigated a local part of the spacetime near spacelike singularities under the influence of different matter contents, namely scalar radiation, dust (with pressure $P = 0$) and relativistic isotropic radiation. The localised study followed previous work by Ori using a homogeneous model of the spacetime, based on the assumption that near a spacelike singularity, spacetime is mainly dependent upon the timecoordinate[‡]. Throughout our investigations we have calculated the Kretschmann scalar to locate the Plank region, considering this region a physical singularity.

The results of these researches have resulted in the paper "Physics of the interior of a spherical, charged black hole with a scalar field"[14], which is presented in the next chapter.

References for Chapter 3

- [1] V. Frolov and I. Novikov, *Black Hole Physics* (Kluwer Academic Publishers, 1998).
- [2] L. M. Burko and A. Ori, eds., *Internal Structure of Black Holes and Spacetime Singularities*, vol. XIII (Institute of Physics Publishing, Bristol and Philadelphia and Israel Physical Society, Jerusalem, 1997).
- [3] E. Poisson and W. Israel, *Phys. Rev.* **D41**, 1976 (1990).
- [4] R. H. Price, *Phys. Rev.* **D5**, 2419 (1972).
- [5] R. Penrose, in *Battelle Rencontres*, edited by C. M. DeWitt and J. A. Wheeler (Benjamin, NY, 1968).
- [6] S. Chandrasekhar and J. B. Hartle, *Proc. R. Soc. London* **A384**, 301 (1982).
- [7] W. B. Bonnor and P. C. Vaidya, *Gen. Relativ. Gravit.* **1**, 127 (1970).
- [8] B. T. Sullivan and W. Israel, *Phys. Lett.* **79A**, 371 (1980).
- [9] G. F. R. Ellis and A. R. King, *Commun. Math. Phys.* **38**, 119 (1974).
- [10] A. R. King, *Phys. Rev.* **D11**, 763 (1975).
- [11] S. Droz, W. Israel, and S. Morsink, *Physics World* **9**, 34 (1995).
- [12] A. Bonnano, S. Droz, W. Israel, and S. Morsink, *Proc. R. Soc. London* **A450**, 553 (1995).
- [13] A. Ori, *Phys. Rev. Letters* **67**, 789 (1991).
- [14] J. Hansen, A. Khokhlov, and I. Novikov, "Physics of the interior of a spherical, charged black hole with a scalar field", Accepted for publication in *Phys. Rev. D*, gr-qc/0501015. (2005).
- [15] R. Balbinot and E. Poisson, *Phys. Lett.* **70**, 13 (1992).
- [16] W. G. Anderson, P. R. Brady, W. Israel, and S. M. Morsink, *Phys. Lett.* **70**, 1041 (1993).

[‡]Note that the timelike coordinate in the region between r_+ and r_- is the radial coordinate.

- [17] P. R. Brady and J. D. Smith, Phys. Rev. Lett. **75**, 1256 (1995).
- [18] L. M. Burko and A. Ori, Phys. Rev. **D56**, 7820 (1997).
- [19] L. M. Burko, Phys. Rev. **D66**, 024046 (2002).
- [20] L. M. Burko, Phys. Rev. **D58** (1998).

Chapter 4

Physics of the interior of a spherical, charged black hole with a scalar field

By:
Jakob Hansen*, Alexei Khokhlov[†] and Igor Novikov*^{,‡,§}

Physical Review D, Vol. 71, 064013 (2005)

Abstract:

We analyse the physics of nonlinear gravitational processes inside a spherical charged black hole perturbed by a self-gravitating massless scalar field. For this purpose we created an appropriate numerical code. Throughout the paper, in addition to investigation of the properties of the mathematical singularities where some curvature scalars are equal to infinity, we analyse the properties of the physical singularities where the Kretschmann curvature scalar is equal to the planckian value. Using a homogeneous approximation we analyse the properties of the spacetime near a spacelike singularity in spacetimes influenced by different matter contents namely a scalar field, pressureless dust and matter with ultrarelativistic isotropic pressure. We also carry out full nonlinear analyses of the scalar field and geometry of spacetime inside black holes by means of an appropriate numerical code with adaptive mesh refinement capabilities. We use this code to investigate the nonlinear effects of gravitational focusing, mass inflation, matter squeeze, and these effects dependence on the initial boundary conditions. It is demonstrated that the position of the physical singularity inside a black hole is quite different from the positions of the mathematical singularities. In the case of the existence of a strong outgoing flux of the scalar field inside a black hole it is possible to have the existence of two null singularities and one central $r = 0$ singularity simultaneously.

PACS numbers: 04.70.Bw, 04.20.Dw

*Niels Bohr Institute, Blegdamsvej 17, DK-2100 Copenhagen, Denmark

[†]Department of Astronomy and Astrophysics, The University of Chicago,
5640 Ellis Avenue, Chicago, IL 60637, USA

[‡]NORDITA, Blegdamsvej 17, DK-2100 Copenhagen, Denmark

[§]Astro Space Center of P.N. Lebedev Physical Institute, Profsoyuznaja 83/32, Moscow 118710, Russia

4.1 Introduction

The problems of the internal structure of black holes are a real great challenge and has been the subject of very active analytical and numerical researches during the last decades [1–24]. There has been a great progress in these researches in the last few years and we now know many important properties of the realistic black hole’s interior, but some details and crucial problems are still the subject of much debate.

Many important results have been obtained under simplifying assumptions. One of the most widely used test toy models is a spherical, charged, non-rotating black hole, nonlinearly perturbed by a minimally coupled and self-gravitating massless, uncharged, scalar field. While this toy model is not very realistic, it share many properties, including causal structure, with the more realistic rotating black holes (e.g. [9] page 5 and [25]) which is why it is believed that insights into this model may give us important understandings about rotating black holes.

The purpose of this paper is to continue the analysis of the physical processes in the interior of black holes in the framework of this toy model.

Inside a black hole the main sights are the singularity. A number of rigorous theorems (see references in [26]) imply that singularities in the structure of spacetime develops inside black holes. Unfortunately these theorems tell us practically nothing about the locations and the nature of the singularities. It has been found that in principle two types of singularities can exist inside black holes corresponding to the toy model: A strong spacelike singularity and a weak null singularity (instead of the inner horizon of a Reissner-Nordström black hole). Probably both types of singularities can exist simultaneously in the same black hole and probably it is possible to have cases where only the strong spacelike singularity exists. In the works [27] and references therein, some physical and geometrical properties of the singularities have been investigated. Numerical simulations of the fully nonlinear evolution of the scalar field and the geometry inside the spherical charged black hole has been carried out in [10, 14, 15, 28].

Near the strong spacelike singularity, one can use a homogeneous approximation in which it is supposed that temporal gradients are much greater than the spatial gradients. Hence it may be assumed that all processes near the singularity depend on the time coordinate only. This uniform approximation has been used in [9] (page 212) and [11, 29] to gain important new knowledge about the processes near the singularity. We will use the same homogeneous approximation to extend these analyses and clarify some fundamental physical processes near spacelike singularities under the influence of three different matter contents, namely for the case of pressureless dust, a massless scalar field and matter with ultrarelativistic isotropic pressure. This investigation is done by means of a suitable numerical code which we develop for this purpose.

Subsequently we will study the nonlinear processes in large regions inside the toy model black hole, not just limited to the homogeneous approximation near the singularity. This will be done by using a stable and second order accurate, numerical code with adaptive mesh refinement capabilities. We will perturb the black hole with initial infalling scalar fields of different forms and strengths to further investigate the behaviour of the singularities and physical processes near them. We will also investigate the influence of outgoing scalar fluxes on the interior regions and the singularity. Such outgoing fluxes will unavoidably appear as a result of the scattering of ingoing scalar field flux by the curvature of the spacetime and will also be emitted from the surface of a star collapsing to a black hole.

Today it is widely believed that in the singularity of a realistic black hole, the curvature of the spacetime tends to infinity. Close to the singularity, where the curvature approaches the Planck value ($(\frac{\hbar G}{3})^2 \approx 1.5 \cdot 10^{131} \text{ cm}^{-4}$ [30]), classical General Relativity is not applicable.

There is not yet a final version of the quantum theory of gravity, thus any extension of the discussion of physics in this region would be highly speculative and we will consider these regions as singularities from the classical point of view throughout the paper.

The paper is organised as follows; In section 4.2 we present our model of the spherically symmetric, charged black hole. In section 4.3 we discuss the mass function and some important nonlinear effects which are fundamental for understanding the physical processes inside black holes. In section 4.4 we use a homogeneous approximation to analyse the (spacelike) singularity for three different matter contents: dust with zero pressure, a massless scalar field and matter with relativistic isotropic pressure. In section 4.5 we analyse the full nonlinear equations of the model from section 4.2 using a numerical approach. Finally we summarize our conclusions in section 4.6. Details of the numerical code used to obtain the results in section 4.5 and analysis of it are given in appendices 4.7 and 4.7.

4.2 The model

We wish to study the geometry inside a spherically symmetric black hole with a fixed electrical charge q (i.e. Reissner-Nordström metric), which is nonlinearly perturbed by a selfgravitating, minimally coupled, massless scalar field. While astrophysical black holes are more likely to be described by the Kerr metric, it is believed that this toy model captures the essential physics, since the causal and horizon structures of the Reissner-Nordström and Kerr black holes are known to be very similar [9] (page 5). However, it is much simpler to make a numerical model of the toy model since this can be simulated in a two-dimensional spacetime. In constructing the toy model, we follow here the approach of Burko and Ori [14, 15, 28] who have done similar investigations.

4.2.1 Field equations

In spherical symmetry, the general line element in double null-coordinates can be written as:

$$ds^2 = -2e^{2\sigma(u,v)} du dv + r^2(u,v) d\Omega^2 \quad (4.1)$$

where $d\Omega^2 = d\theta^2 + \sin^2(\theta)d\phi^2$ is the line element on the unit two-sphere and r is a function of the null coordinates u and v (in- and outgoing respectively).

With this metric the non-zero components of the Einstein tensor are:

$$G_{uu} = \frac{4r_{,u}\sigma_{,u} - 2r_{,uu}}{r} \quad (4.2a)$$

$$G_{vv} = \frac{4r_{,v}\sigma_{,v} - 2r_{,vv}}{r} \quad (4.2b)$$

$$G_{uv} = \frac{e^{2\sigma} + 2r_{,v}r_{,u} + 2r r_{,uv}}{r^2} \quad (4.2c)$$

$$G_{\theta\theta} = -2e^{-2\sigma}r(r_{,uv} + r\sigma_{,uv}) \quad (4.2d)$$

$$G_{\phi\phi} = -2e^{-2\sigma}r\sin^2(\theta)(r_{,uv} + r\sigma_{,uv}) \quad (4.2e)$$

The energy-momentum tensor can be written as a sum of contributions from electromagnetic and scalar fields:

$$T_{\mu\nu} = T_{\mu\nu}^s + T_{\mu\nu}^{em} \quad (4.3)$$

The energy-momentum tensor of a massless scalar field Φ is [30]:

$$T_{\mu\nu}^s = \frac{1}{4\pi} \left(\Phi_{,\mu}\Phi_{,\nu} - \frac{1}{2}g_{\mu\nu}g^{\alpha\beta}\Phi_{,\alpha}\Phi_{,\beta} \right) \quad (4.4)$$

whose non-zero components for the metric (4.1) are:

$$T_{uu}^s = \frac{1}{4\pi} \Phi_{,u}^2 \quad (4.5a)$$

$$T_{vv}^s = \frac{1}{4\pi} \Phi_{,v}^2 \quad (4.5b)$$

$$T_{\theta\theta}^s = \frac{1}{4\pi} r^2 e^{-2\sigma} \Phi_{,u} \Phi_{,v} \quad (4.5c)$$

$$T_{\phi\phi}^s = \frac{1}{4\pi} r^2 \sin^2(\theta) e^{-2\sigma} \Phi_{,u} \Phi_{,v} \quad (4.5d)$$

The energy-momentum tensor of an electric field in spherical symmetry and null coordinates is [30]:

$$T_{\mu\nu}^{em} = F_{\mu\alpha} F_{\nu}^{\alpha} + \frac{1}{4} g_{\mu\nu} F_{\mu\nu} F^{\mu\nu} \quad (4.6)$$

whose non-zero components for the metric (4.1) are:

$$T_{uv}^{em} = \frac{q^2}{8\pi r^4} e^{2\sigma} \quad (4.7a)$$

$$T_{\theta\theta}^{em} = \frac{q^2}{8\pi r^4} r^2 \quad (4.7b)$$

$$T_{\phi\phi}^{em} = \frac{q^2}{8\pi r^4} r^2 \sin^2(\theta) \quad (4.7c)$$

From the Einstein and energy-momentum tensors we can write up the Einstein equations, $G_{\mu\nu} = 8\pi T_{\mu\nu}$ (with $c = 1, G = 1$), governing the spacetime. The $u - u$, $v - v$, $u - v$ and $\theta - \theta$ components of the Einstein equations respectively are:

$$r_{,uu} - 2r_{,u}\sigma_{,u} + r(\Phi_{,u})^2 = 0 \quad (4.8)$$

$$r_{,vv} - 2r_{,v}\sigma_{,v} + r(\Phi_{,v})^2 = 0 \quad (4.9)$$

$$r_{,uv} + \frac{r_{,v}r_{,u}}{r} + \frac{e^{2\sigma}}{2r} \left(1 - \frac{q^2}{r^2}\right) = 0 \quad (4.10)$$

$$\sigma_{,uv} - \frac{r_{,v}r_{,u}}{r^2} - \frac{e^{2\sigma}}{2r^2} \left(1 - 2\frac{q^2}{r^2}\right) + \Phi_{,u}\Phi_{,v} = 0 \quad (4.11)$$

Lastly, the scalar field must satisfy the Gordon-Klein equation (note that Gordon-Klein is a consequence of the Einstein equations for the scalar field [30]), $\nabla^{\mu}\nabla_{\mu}\Phi = 0$, which in the metric (4.1) becomes:

$$\Phi_{,uv} + \frac{1}{r}(r_{,v}\Phi_{,u} + r_{,u}\Phi_{,v}) = 0 \quad (4.12)$$

Equations (4.10) - (4.12) are evolution equations which are supplemented by the two constraint equations (4.8) and (4.9). It is noted that none of these equations depends on the scalar field Φ itself, but only on the derivatives of Φ , i.e. the derivative of the scalar field is a physical quantity, while the absolute value of the scalar field itself is not. Specifically we note the $T_{uu} = (\Phi_{,u})^2/4\pi$ and $T_{vv} = (\Phi_{,v})^2/4\pi$ components of the energy-momentum tensor which are part of the constraint equations. Physically T_{uu} and T_{vv} represents the flux of the scalar field through a surface of constant v and u respectively. These fluxes will play an important role in our interpretation of the numerical results in section 4.5.

4.2.2 Initial value problem

We wish to numerically evolve the unknown functions $r(u, v)$, $\sigma(u, v)$ and $\Phi(u, v)$ throughout some computational domain. We do this by following the approach of [10, 15, 28] to numerically integrate the three evolution equations (4.10) - (4.12). These equations form a well-posed initial value problem in which we can specify initial values of the unknowns on two initial null segments, namely an outgoing ($u = u_0 = \text{constant}$) and an ingoing ($v = v_0 = \text{constant}$) segment. We impose the constraint equation (4.8) and (4.9) on the initial segments. Consistency of the evolving fields with the constraint equations is then ensured via the contracted Bianchi identities [28], but we use the constraint equations throughout the domain of integration to check the accuracy of the numerical simulation.

On the initial null segments, the constraint equations reduces the number of unknowns by one on $v = v_0$ and $u = u_0$ respectively. The remaining two unknowns expresses only one degree of physical freedom, while the other unknown expresses the gauge freedom associated with the transformation $u \rightarrow \tilde{u}(u)$, $v \rightarrow \tilde{v}(v)$, (the line element (4.1) and eqs. (4.8)-(4.12) are invariant to such a transformation). We choose a standard gauge in which r is linear in v and u on the initial null segments. Specifically we choose:

$$r(u_0, v) = v, \quad r(u, v_0) = r_0 + u r_{u0} \quad (4.13)$$

We also choose that the outgoing segment should run along $u_0 = 0$.

We can now use (4.8) and (4.9) to find:

$$\sigma_{,v}(u_0, v) = \frac{1}{2r_{,v}} \left(r_{,vv} + r (\Phi_{,v})^2 \right) = \frac{v}{2} (\Phi_{,v})^2 \quad (4.14a)$$

$$\sigma_{,u}(u, v_0) = \frac{1}{2r_{,u}} \left(r_{,uu} + r (\Phi_{,u})^2 \right) = \frac{r_0 + u r_{u0}}{2r_{u0}} (\Phi_{,v})^2 \quad (4.14b)$$

which can be readily integrated to find $\sigma(u, v)$ on the initial null segments if Φ and the constants r_0, r_{u0} and $\sigma(u_0, v_0)$ are specified on these.

Following [14, 15, 28] we choose $\sigma(u_0, v_0) = -\frac{\ln(2)}{2}$ and $r_0 = 5$. The parameter r_{u0} , can be related to the initial mass and charge of the black hole via the mass function (the mass function is further discussed in section 4.3) which in the metric (4.1) has the form:

$$m(u, v) = \frac{r}{2} \left(1 + \frac{q^2}{r^2} + 4 \frac{r_{,u} r_{,v}}{2e^{2\sigma}} \right) \quad (4.15)$$

which in our choice of gauge, at the point of intersection of the initial null segments, take the form:

$$m_0 = m(u_0, v_0) = \frac{r_0}{2} \left(1 + \frac{q^2}{r_0^2} + 4r_{u0} \right) \quad (4.16)$$

hence r_{u0} can be determined by r_0 , m_0 and q as:

$$r_{u0} = \frac{1}{4} \left(\frac{2}{r_0} \left(m_0 - \frac{q^2}{2r_0} \right) - 1 \right). \quad (4.17)$$

Hence, by specifying a distribution of the scalar field Φ on the initial null segments, choosing a gauge and initial charge and mass of the black hole we can specify complete initial conditions on the initial null segments. Using a numerical code (described in appendix 4.A) we can then use the evolution equations, eqs. (4.10) - (4.12) to evolve the unknown functions throughout the computational domain.

4.3 Nonlinear effects; internal mass function

We will in the next sections consider the evolution of the scalar field together with the geometry of the interior of a black hole. This evolution is highly nonlinear. One of the main parameters of this evolution is the mass function which represents the total effective mass in a sphere of radius $r(u, v)$ [2, 26, 31]. We give here different expressions for the mass function, which emphasize its different characteristics.

In the metric:

$$\begin{aligned} ds^2 &= g_{tt}dt^2 + g_{rr}dr^2 + r^2d\Omega^2 \\ d\Omega^2 &= d\theta^2 + \sin^2\theta d\phi^2 \end{aligned} \quad (4.18)$$

the mass function can be written in the following forms:

$$m = \frac{r}{2} \left(1 + \frac{q^2}{r^2} - g_{rr}^{-1} \right) \quad (4.19)$$

or

$$m = 4\pi \int_{r_1}^{r_2} T_t^t r^2 dr + m_0 \quad (4.20)$$

In the metric

$$ds^2 = -\alpha^2 dudv + r^2 d\Omega^2 \quad (4.21)$$

it has the form [16, 28]:

$$m = \frac{r}{2} \left(1 + \frac{q^2}{r^2} + 4 \frac{r_{,u} r_{,v}}{\alpha^2} \right) \quad (4.22)$$

or (for the scalar field, Φ) [16]:

$$m_{,uv} = 2 \frac{r^3}{\alpha^2} \Phi_{,u}^2 \Phi_{,v}^2 - r \left(1 - \frac{2m}{r} + \frac{q^2}{r^2} \right) \Phi_{,u} \Phi_{,v} \quad (4.23)$$

There are two important physical processes which can lead to a nonlinear change of the mass parameter:

1. The mass m inside a sphere can change because of the work of pressure forces on the surface of the sphere. A clear manifestation of this squeeze effect is the change of the mass of a spherical volume in a homogeneous model of the Universe filled with relativistic gas (see [32], page 13). In section 4.4 we will consider another example, namely for the case of the imitation of the interior of a black hole. For the description of this process, it is most appropriate to use the form (4.20) for the mass function. Remember that inside the event horizon, r is a time-like coordinate.
2. Mass inflation [2]. This process inside the black hole exists if near the Cauchy horizon (CH) there are simultaneous ingoing and outgoing fluxes of a massless field (for example scalar field). Actually the existence of the outgoing flux together with the ingoing is inevitable because of backscattering of part of the ingoing flux by the spacetime curvature. The simplest exact model of the mass inflation process inside of a black hole has been constructed by Ori [3]. For the description of this process it is most useful to use formula (4.23) from which it can be seen that evolution of m with both u and v is possible only if there are both $\Phi_{,u}^2$ and $\Phi_{,v}^2$ fluxes simultaneously.

One can often observe the simultaneous manifestation of both these processes.

Another important nonlinear effect is the focusing effect by the gravity of beams of opposite fluxes of radiation. A particular manifestation of the focusing effect is the contraction of the CH under the gravity of transverse irradiation by the outgoing radiation. Eventually the CH singularity shrinks down to a point-like size and meets a central (probably spacelike) singularity $r = 0$. It should be mentioned that it is incorrect to say that the CH singularity is transformed into a $r = 0$ spacelike singularity, because the formation of the $r = 0$ singularity is causally absolutely independent from the formation of the CH singularity.

We want to mention that it is possible, in principle, to have the situation when the mass function depends on only one null coordinate, say v , while it does not depend on the other u coordinate. This situation is described by a charged Vaidya solution [33]. In this solution there is an effect of a linear change of m , because of an ingoing lightlike radial flux of energy into the black hole (without any scattering of this radiation by a curvature of the spacetime). Of course this effect is compatible with formula (4.23).

4.4 Homogeneous approximation

In the close vicinity of the spacelike singularity of a black hole all processes, as a rule, have high temporal gradients, much higher than the spatial gradients along the singularity, and the processes depend on a very restricted space region. So for clarification of some physical processes one can use a homogeneous approximation and assume that all processes depend on the time coordinate only. This approach has been proposed by Burko [9, 29] and we will use it at the beginning of our analysis to clarify some main properties of the singularity before coming to the full analysis of the spherical model in section 4.5.

The general homogeneous, spherically symmetric line element has the form:

$$\begin{aligned} ds^2 &= g_{tt}(r)dt^2 + g_{rr}(r)dr^2 + r^2 d\Omega^2 \\ d\Omega^2 &= d\theta^2 + \sin^2 \theta d\phi^2 \end{aligned} \quad (4.24)$$

Inside a black hole in the region between the event horizon and the Cauchy horizon (or the spacelike singularity) r is timelike and t is spacelike. To describe the contraction of the CH, we should thus consider the variation of the time coordinate r from bigger to smaller values. The $r - r$, $t - t$ and $\theta - \theta$ components of the Einstein equations (with $c = 1, G = 1$) are then given by:

$$\frac{g_{tt} - g_{rr} g_{tt} + r g'_{tt}}{r^2 g_{rr} g_{tt}} = 8\pi (T_r^r + E_r^r) \quad (4.25)$$

$$\frac{g_{rr} - g_{rr}^2 - r g'_{rr}}{r^2 g_{rr}^2} = 8\pi (T_t^t + E_t^t) \quad (4.26)$$

$$\begin{aligned} \frac{1}{4r g_{rr}^2 g_{tt}^2} \{ g_{tt} [2g_{rr} (g'_{tt} + r g''_{tt}) - (r g'_{rr} g'_{tt})] \\ - 2g_{tt}^2 g'_{rr} - r g_{rr} g_{tt}^2 \} = 8\pi (T_\theta^\theta + E_\theta^\theta) \end{aligned} \quad (4.27)$$

where the primes denotes differentiation with respect to r (the $\phi - \phi$ component of the Einstein equations again yields equation (4.27)). The tensor E represents here contribution from a free electric field corresponding to a charge q , which we will assume to be constant:

$$E_r^r = E_t^t = -E_\theta^\theta = -\frac{q^2}{8\pi r^4}, \quad (4.28)$$

while the tensor T represent contributions from other matter contents.

To clarify the meaning of different processes we will consider three different physical matter contents (in addition to the electric field) with different equations of state. Namely, we will consider:

- A) Dust
- B) A massless scalar field
- C) Ultrarelativistic gas

From the Einstein equations one can find the following expressions for the non-zero components of T for these matter contents:

A) Dust (with pressure $P = 0$):

$$T_r^r = -\epsilon = \epsilon_0 \left(\frac{g_{tt,init}}{g_{tt}} \right)^{\frac{1}{2}} \left(\frac{r_{init}}{r} \right)^2 \quad (4.29)$$

where ϵ_0 , $g_{tt,init}$ and r_{init} are constants.

B) Massless scalar field [9]:

$$T_r^r = -\epsilon \quad (4.30a)$$

$$T_t^t = \epsilon \quad (4.30b)$$

$$T_\theta^\theta = \frac{\epsilon}{g_{rr}} \quad (4.30c)$$

$$\epsilon = \epsilon_0 \left(\frac{g_{tt,init}}{g_{tt}} \right) \left(\frac{r_{init}}{r} \right)^4 = \frac{-1}{8\pi g_{rr}} \left(\frac{d\Phi}{dr} \right)^2 \quad (4.30d)$$

$$\epsilon_0 = \frac{d^2}{8\pi} \frac{1}{g_{tt,init} r_{init}^4} \quad (4.30e)$$

where d is a constant which were used in [9].

C) Ultrarelativistic gas (with isotropic pressure $P = \frac{\epsilon}{3}$, ϵ being matter density):

$$T_r^r = -\epsilon \quad (4.31a)$$

$$T_t^t = T_\theta^\theta = \frac{\epsilon}{3} \quad (4.31b)$$

$$\epsilon = \epsilon_0 \left(\frac{g_{tt,init}}{g_{tt}} \right)^{\frac{2}{3}} \left(\frac{r_{init}}{r} \right)^{\frac{8}{3}} \quad (4.31c)$$

Substitution of (4.29)-(4.31) into (4.25) and (4.26) enables us to find the unknown functions $g_{rr} = g_{rr}(r)$ and $g_{tt} = g_{tt}(r)$ and hence solve the problem for each of the three cases. Equation (4.27) can be used as a control of the calculations.

Formally metric (4.24) corresponds to a metric of a special class of the ‘‘homogeneous cosmological models’’ considered by Zeldovich and Novikov [32] (page 535), Grishchuk [34] and others.

4.4.1 Dust, $P = 0$

Leading order analysis

Let us start the discussion with the simplest case, namely the case of dust with pressure $P = 0$.

In this case it is possible to have a singularity at $r = r_{sing} \neq 0$ with $r_{CH} < r_{sing} < r_{EH}$, where r_{CH} and r_{EH} are the positions of the Cauchy Horizon and the Event Horizon in the absence of dust.

Let us consider the leading order terms in a series expansion for the metric functions and leading order terms in the Einstein equations, near the singularity. Close to the singularity, where $g_{tt} \rightarrow 0$, a leading order expansion of eqs. (4.25)+(4.29) gives us:

$$\frac{dg_{tt}}{dx} \frac{1}{g_{tt} r_{sing}} = - \frac{8\pi (g_{rr})_{sing} \epsilon_0}{\left(\frac{g_{tt}}{g_{tt,init}}\right)^{1/2} \left(\frac{r_{sing}}{r_{init}}\right)^2} \quad (4.32)$$

where $(g_{rr})_{sing} = g_{rr}(r_{sing})$ and $g_{tt,init} = g_{tt}(r_{init})$ and where we assume that $g_{tt} = Ax^\alpha$ and $x = r - r_{sing}$. Also A, α are constants and $(g_{rr})_{sing} = g_{rr}(r_{sing})$ is the value of g_{rr} at the singularity $r = r_{sing}$.

From (4.32) one find:

$$\alpha = 2 \quad (4.33)$$

which leads in turn to (remember that $(g_{rr})_{sing}$ is negative for $r_{CH} < r < r_{EH}$):

$$r_{sing} = - \frac{4\pi (g_{rr})_{sing} \epsilon_0 r_{init}^2 \sqrt{g_{tt,init}}}{\sqrt{A}} \quad (4.34)$$

Using the proper time $\tau : d\tau = \sqrt{|g_{rr}|} dr$ we have for the vicinity of the singularity:

$$\begin{aligned} g_{tt} &\propto \tau^2, \\ r &\propto \tau^0 = const., \\ \tau &= 0 \text{ at the singularity} \end{aligned} \quad (4.35)$$

For the Kretschmann scalar $K \equiv R_{iklm}R^{iklm}$ we have [9]:

$$K = \frac{12}{\tau^4} \quad (4.36)$$

Thus this spacelike singularity does not correspond to $r = 0$

Numerical analysis

To understand the behaviours of the model (4.24) as functions of the parameters of the model we use a simple numerical code to numerically solve (4.25)+(4.26) substituting (4.29) for the stress-energy tensor. According to the remark in the introduction we consider the region with $K = K_{planck}$ as a physical singularity and will consider only the region with $r > r_c$, where r_c corresponds to the critical value of r at which the Kretschmann scalar is equal to the planckian value. We will take this restriction into account in all our subsequent analyses.

We note that for the case of dust $P = 0$ there are no nonlinear effects causing an increase of the mass function m . This is seen from eq. (4.20) because $T_t^t = P = 0$.

To analyse the change of r_c with variation of the matter contents we numerically integrate eqs.(4.25), (4.26), (4.29). As initial values we use $r_{init} = 0.95 \cdot r_{EH} \approx 1.25$ and set $g_{tt,init}$ and

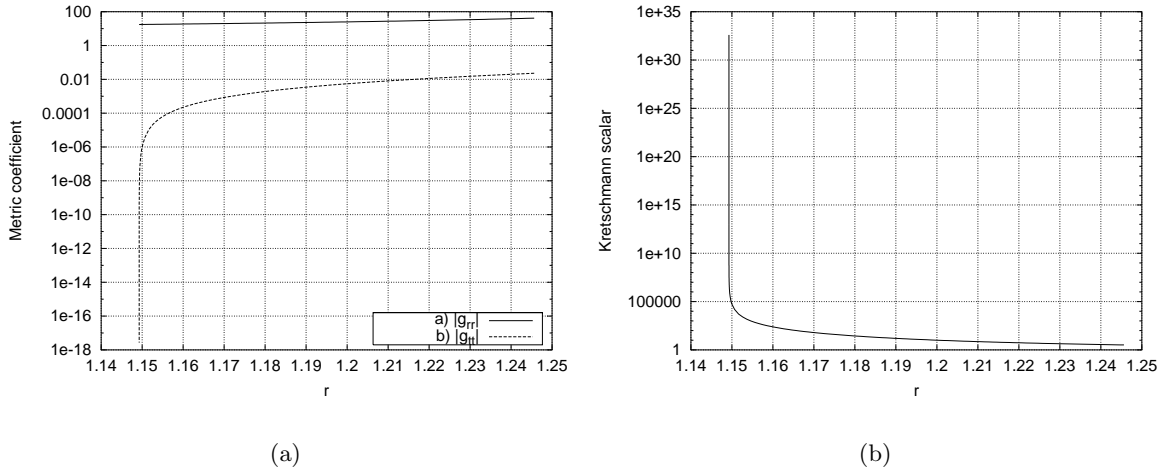


Figure 4.1: Metric coefficients (plot a) and Kretschmann scalar (plot b) versus r for the case of dust with $\epsilon_0 = 0.03$

$g_{rr,init}$ equal to their values at r_{init} for the Reissner-Nordström solution (with initial mass $m_0 = 1$ and charge $q = 0.95$) and vary the initial matter density ϵ_0 .

Figure 4.1(a) shows an example of the variation of the metric functions with r for the case $\epsilon_0 = 0.03$. It is seen that $g_{tt} \rightarrow 0$ as $r \rightarrow r_c \approx 1.149$. As $g_{tt}(r) \rightarrow 0$, the density and curvature increases rapidly, which can easily be understood from eq. (4.29). This is indicated in fig. 4.1(b) which shows the variation of $K(r)$ for the same case. The line in this figure does not visibly reach $K = K_{planck} \approx 1.5 \cdot 10^{131}$, however this is solely due to limitations in numerical resolution because of the catastrophic blowup of $K(r)$ as indicated by the vertical line in the figure.

The dependence of r_c on the initial matter density ϵ_0 can be seen in fig. 4.2. Near the mathematical singularity, r_{sing} , the scalar K increases very rapidly with decreasing r , so approximately $r_{sing} \approx r_c$ (physical singularity). As one can see from the figure, for the case of dust, r_c decreases with decreasing ϵ_0 until $r_c \rightarrow r_{CH}$ at $\epsilon_0 \rightarrow 0$. This behaviour is easily understood: for smaller matter contents it takes a longer time to compress the dust to the critical density at r_c . On the other hand, in the Reissner-Nordström solution without additional matter, the volume of the uniform reference frame (4.24) tends to zero when $r \rightarrow r_{CH}$ (because $g_{tt} \rightarrow 0$). So when $\epsilon_0 \rightarrow 0$ and the behaviours of the solutions are close to the Reissner-Nordström solution, the matter density of dust must tend to infinity when the volume tends to zero at $r \rightarrow r_{CH}$. Note that this spacelike singularity $r = r_{sing}$ is not a central singularity $r = 0$. The physical singularity, where $K = K_{planck}$, practically coincide with the mathematical one, where $K = \infty$.

Finally we note that the laws (4.35), (4.36) has been confirmed by numerical calculations.

4.4.2 Massless scalar field

The case of a scalar field has been analysed by Burko in [9]. Here we extend his analysis.

This case differs drastically from the case of dust. In this case a mathematical singularity r_{sing} can exist only at $r_{sing} = 0$. In the vicinity of this singularity the solution (4.25), (4.26),

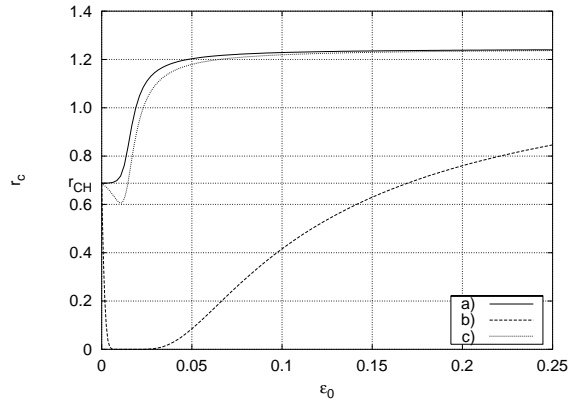


Figure 4.2: Critical value r_c as a function of ϵ_0 for a) Dust case, b) Scalar case and c) Ultrarelativistic gas.

(4.30) can be written in the first approximation as follows:

$$g_{tt} = 2mCr^\beta \quad (4.37a)$$

$$g_{rr} = -(\beta + 2)\frac{1}{2m}r^{\beta+2} \quad (4.37b)$$

$$\Phi = \sqrt{\beta + 1} \ln r, \quad (4.37c)$$

where m, C and β are constants. We note that we use constants m and C which are different from Burko's constants. Our constants have direct physical meanings: m is the black hole mass, C is a gauge parameter, related to the possibility of changing the scale of measurement of the t space coordinate. Also we have $d^2 = \frac{(\beta+1)}{(\beta+2)}4m^2C$ where d is a constant used by Burko in [9].

The exponent β depends on the amplitude of the scalar field. As Burko demonstrated $\beta > 0$ if $q \neq 0$. So in the vicinity of the singularity the value of $\left(\frac{d\Phi}{dr}\right)^2$, which is the only term in the equations (4.25), (4.26), (4.30), which determines the strength of the scalar field, can not be smaller than $\frac{1}{r^2}$ (unless it is equal to zero identically). To understand the behaviour of the singularity in this case let us note the following;

In the metric (4.21) the scalar field can be represented as a sum of two equal fluxes moving in opposite directions along the (spacelike) t -axis with the fundamental velocity c . Indeed, let us suppose that in u, v coordinates there are everywhere and always two equal, opposite directed, fluxes along these coordinates, hence $\frac{d\Phi}{du} = \frac{d\Phi}{dv}$ which depend on $r = u + v$, but not on $t = u - v$. Then there is a coordinate transformation:

$$u = R - t, v = R + t \quad (4.38)$$

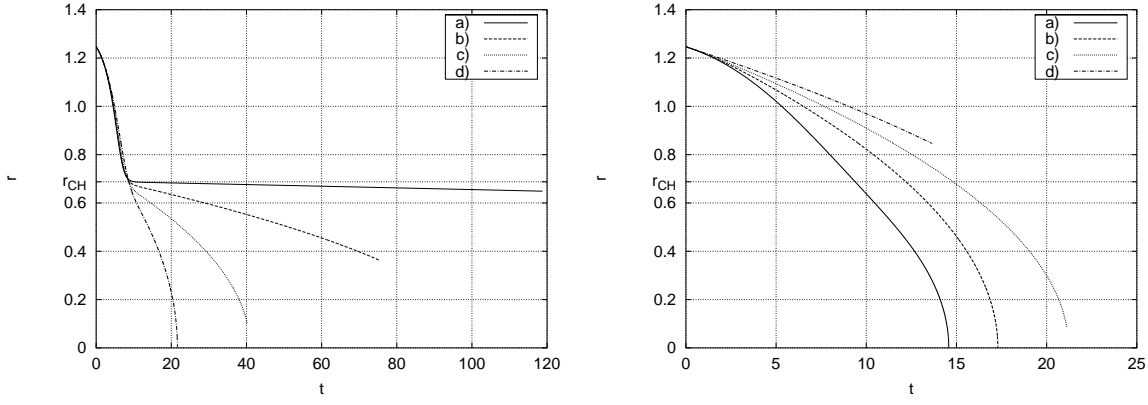
which corresponds to a transformation to the metric (4.24) but with another time coordinate R : $dR = \sqrt{\frac{-g_{rr}}{g_{tt}}} dr$. The transformation (4.38) corresponds to a transformation of the tensor of the scalar field:

$$T_{rr} = T_{tt} = \tilde{T}_{uu} + \tilde{T}_{vv} \quad (4.39a)$$

$$T_{\theta\theta} = \tilde{T}_{\theta\theta} \quad (4.39b)$$

$$T_{\phi\phi} = \tilde{T}_{\phi\phi} \quad (4.39c)$$

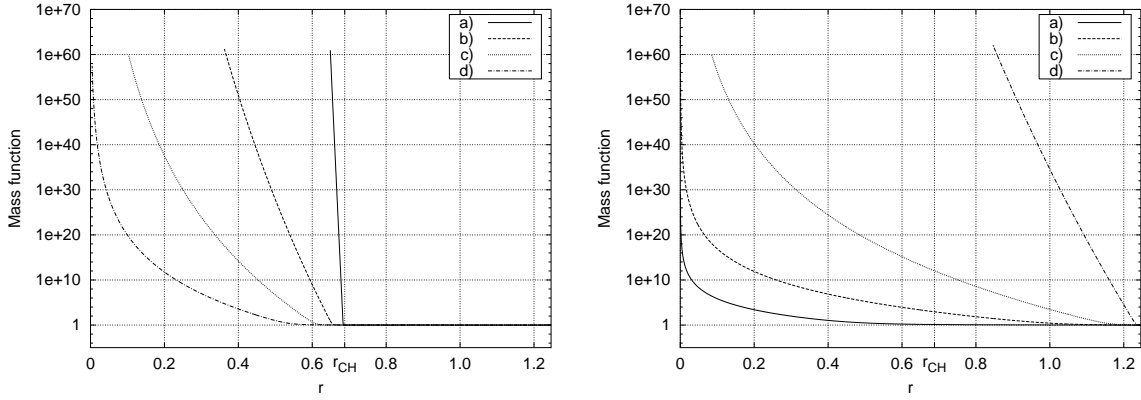
$$\text{All other } T_{ik} = 0 \quad (4.39d)$$



(a) Line a) $\epsilon_0 = 0.0001$, b) $\epsilon_0 = 0.001$, c) $\epsilon_0 = 0.0025$ and d) $\epsilon_0 = 0.005$

(b) Line a) $\epsilon_0 = 0.010$, b) $\epsilon_0 = 0.025$, c) $\epsilon_0 = 0.050$, d) $\epsilon_0 = 0.250$

Figure 4.3: r versus t for the scalar case for various ϵ_0 .



(a) Line a) $\epsilon_0 = 0.0001$, b) $\epsilon_0 = 0.001$, c) $\epsilon_0 = 0.0025$ and line d) $\epsilon_0 = 0.005$

(b) Line a) $\epsilon_0 = 0.010$, b) $\epsilon_0 = 0.025$, c) $\epsilon_0 = 0.050$ and line d) $\epsilon_0 = 0.250$

Figure 4.4: Mass function versus r for the scalar case for various ϵ_0 .

Applying transformation (4.38) to (4.30), the new energy-momentum tensor depends on the timelike coordinate r but not on t . The existence of two opposite fluxes near the Cauchy Horizon should lead to two nonlinear effects: mass inflation and shrinking of the CH down to $r = 0$. The uniformity and equality of the two fluxes lead to the situation where both effects manifest themselves simultaneously and there are not any gradients in space. To see these effects we perform the numerical integration of the system (4.25),(4.26),(4.30). Here, as for the case of dust, we start the computation from $r_{init} = 0.95 \cdot r_{EH} \approx 1.25$, put the initial values of g_{tt} and g_{rr} equal to their values for the zero matter content Reissner-Nordström solution (with $q = 0.95$, $m = 1.0$) at r_{init} and vary the characteristic of the initial amplitude of the scalar field, ϵ_0 .

In fig. 4.3 one can see the propagation (r vs. t) of the ingoing signal with the velocity c ($c = 1$) in models with different ϵ_0 . Fig. 4.4 shows the mass function as a function of r for the same choices of ϵ_0 and fig. 4.5 presents examples of the evolution of the metric functions, g_{tt} and g_{rr} , and K in the models with different ϵ_0 . Also we refer to fig. 4.2, (line b) depicting r_c as a function of ϵ_0 .

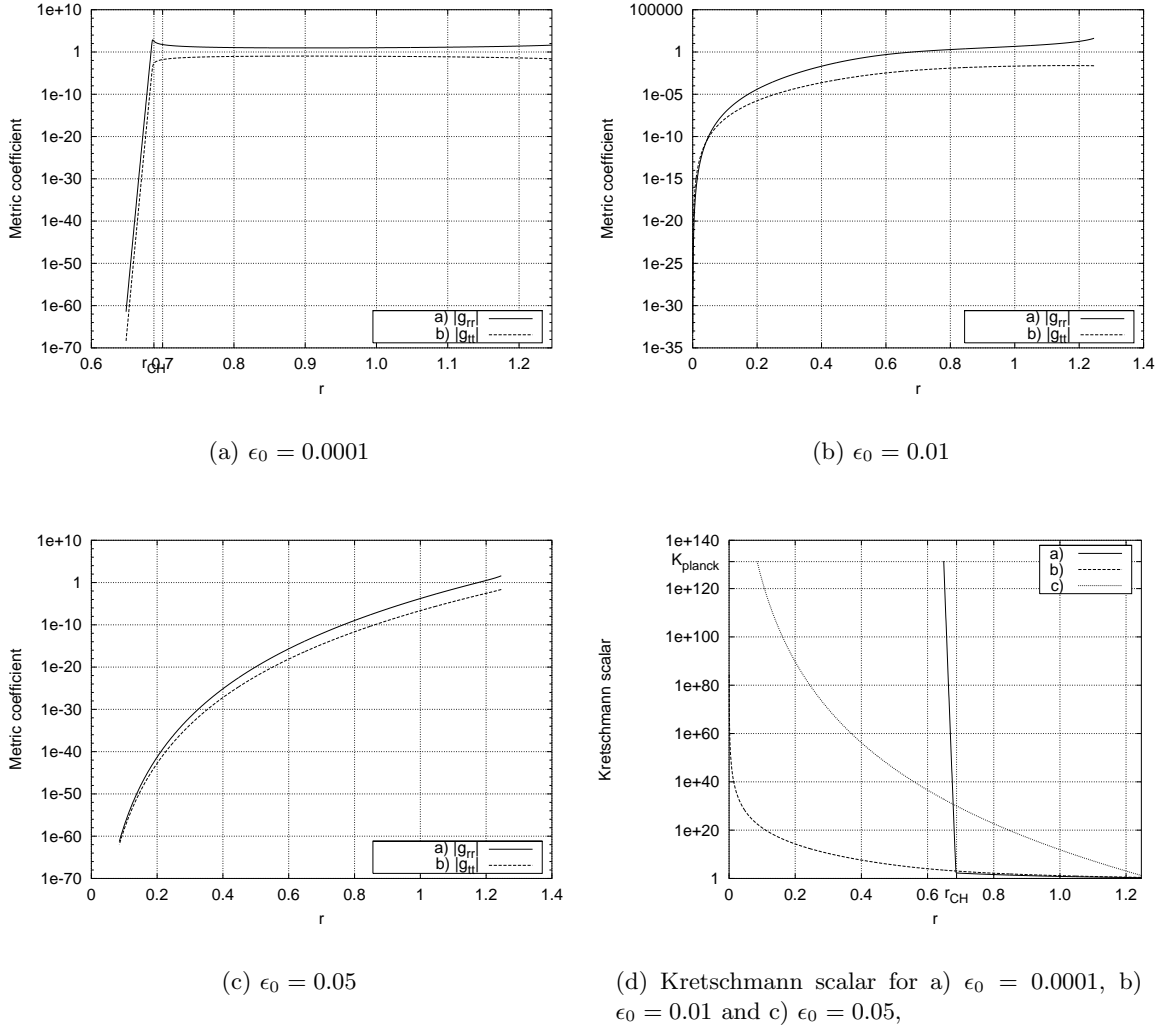


Figure 4.5: Metric functions (a-c) and Kretschmann scalar (d) versus r for the scalar case for various ϵ_0 .

From these figures it is clearly seen that in models with very small ϵ_0 (e.g. $\epsilon_0 = 0.0001$) there is a manifestation of a mass inflation at r close to the CH. First of all we see that the light signal propagates along $r \approx r_{CH}$ during a long period (line “a” in fig. 4.3(a)). This is a necessary condition for mass inflation to occur. Secondly, we see more directly that the massfunction, which was small at large r , starts to manifest mass inflation at r close to r_{CH} (line “a” in fig. 4.4(a)). The metric functions g_{tt} and g_{rr} behaves like the case of the pure Reissner-Nordström solution at larger r , but in the vicinity of r_{CH} they start to collapse (fig. 4.5(a)). We also see that K demonstrates a sudden sharp increases at r close to r_{CH} (fig. 4.5(d), line “a”), and it reaches the K_{planck} value at r_c close to r_{CH} before the shrinkage of the CH manifests itself strongly (fig. 4.5(d)). Thus here we have the *physical* singularity at r close to $r_{CH} \neq 0$.

At larger ϵ_0 , the term associated with scalar matter in the Einstein equations starts to dominate over a term which represents the electric charge much earlier, hence the manifestation of the electric field (which is responsible for the origin of the CH) is not so essential in this case. Functions g_{tt} and g_{rr} differ from the case of the Reissner-Nordström at r essentially larger than r_{CH} (see figs. 4.5(b), 4.5(c) and compare with fig. 4.5(a) which essentially behaves

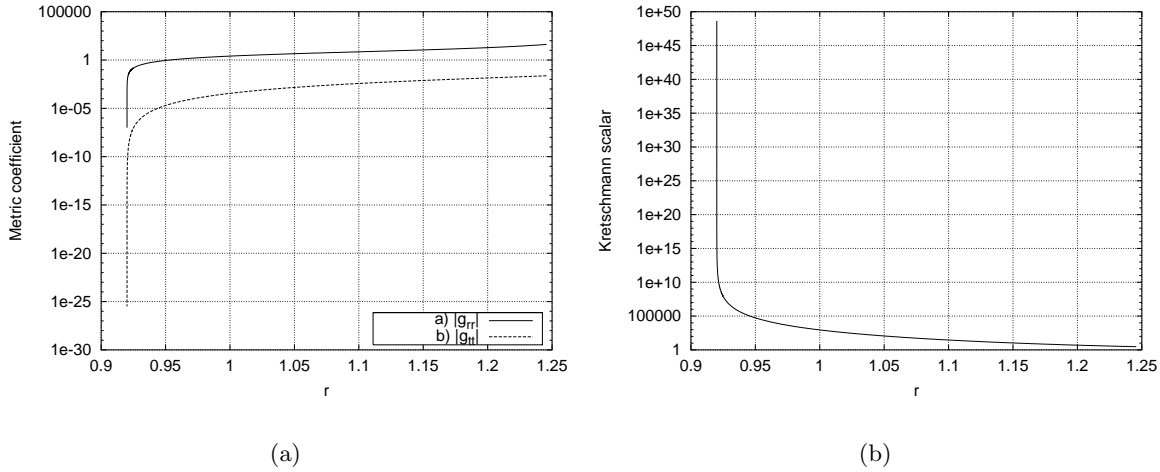


Figure 4.6: Metric functions (plot a) and Kretschmann scalar (plot b) versus r for the case of ultrarelativistic gas for $\epsilon_0 = 0.02$.

like the Reissner-Nordström solution for $r > r_{CH}$). For the cases $\epsilon_0 \geq 0.001$, the light signal propagates at r close to r_{CH} for a very short period of time (line “b,c,d” on Fig. 4.3(a)). For $\epsilon_0 \geq 0.01$ the light signal does not feel the presence of r_{CH} at all (see fig. 4.3(b)). For $0.01 \leq \epsilon_0 \leq 0.03$, we observe the shrinkage of the model to r close to $r = 0$ before K reaches K_{planck} (see line “b” on fig. 4.2). So for these values of ϵ_0 the physical singularity is at r close to $r = 0$.

At big values of ϵ_0 (for example $\epsilon_0 \geq 0.050$) there is not any manifestation of the effects near $r = r_{CH}$ because in this case the light signal does not propagate long enough along $r \approx r_{CH}$ for mass inflation to occur. The mass function nevertheless increases impetuously with decreasing r due to the compression of the model and K reaches the critical value K_{planck} at rather big r (see figs. 4.2, 4.5(c) and 4.5(d)).

4.4.3 Ultrarelativistic gas, $P = \frac{\epsilon}{3}$

The case $P = \frac{\epsilon}{3}$ is in some sense intermediate between the cases of pressureless dust and scalar field as it is seen in fig. 4.2. In fig. 4.6 one can see the contraction of the model and corresponding increase of the Kretschmann scalar K . There is not any manifestation of the mass inflation near $r \approx r_{CH}$, but only the nonlinear effect of the increase of the mass function because of the matter squeeze.

4.5 Physics of the interior

In this section we analyse the fully nonlinear processes inside a spherical, charged black hole with a scalar field, as described in section 4.2, using results from numerical simulations. Our numerical code is described in appendix 4.A and tested in appendix 4.B. As mentioned in the introduction, some parts of this problem have been discussed in works [10, 14, 15]. In this section we extend these analyses and reveal new aspects of the problem. In subsection 4.5.1 we investigate a simple compact pulse. In subsection 4.5.2 we investigate a somewhat more complicated compact pulse and in subsection 4.5.3 we investigate the influence of the T_{uu} flux on the singularities.

To perform this analysis we specify different boundary conditions along some initial $u = u_0 = 0.00$ and $v = v_0 = 5.00$ to imitate some physical fluxes of energy into the charged black hole, perform numerical simulations and analyse the results. Throughout this section, the black hole, prior to influence from scalar pulses, has initial mass $m_0 = 1.00$ and charge $q = 0.95$. Also, our domain of integration is from $5.0 < v < 20.0$ and $0.0 < u < 30.0$. For all simulations the gauge is chosen as described in section 4.2.

4.5.1 Simple compact pulse

We start from the simplest case when the flux of the scalar field into the charged black hole is specified along initial $u = u_0$ outside of the black hole in the following way:

$$\Phi_{,v}(u_0, v) = A \sin^2 \left(\pi \frac{v - v_0}{v_1 - v_0} \right) \quad (4.40)$$

where v_0 and v_1 marks the beginning and end of the ingoing scalar pulse, respectively (i.e. we set the beginning of the pulse equal to the beginning of our computational domain) and A measures the amplitude of the pulse. This can readily be integrated to give:

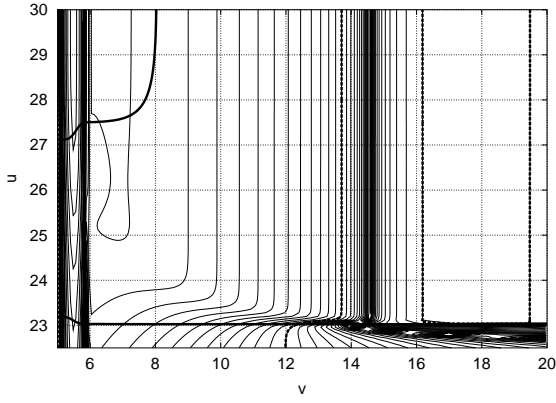
$$\Phi(u_0, v) = \frac{A}{4\pi} \left(2\pi (v - v_0) - (v_1 - v_0) \sin \left(2\pi \frac{v - v_0}{v_1 - v_0} \right) \right) \quad (4.41)$$

After the pulse, at $v > v_1$, the flux through $u = u_0$ is set equal to zero, i.e. $\Phi_{,v}(u_0, v) = 0$. The flux of the scalar field through initial ingoing segment $v = v_0$ is set equal to zero: $\Phi_{,u}(u, v_0) = 0$. This means that there is no flux of energy from the surface of a collapsing charged star into the computational domain.

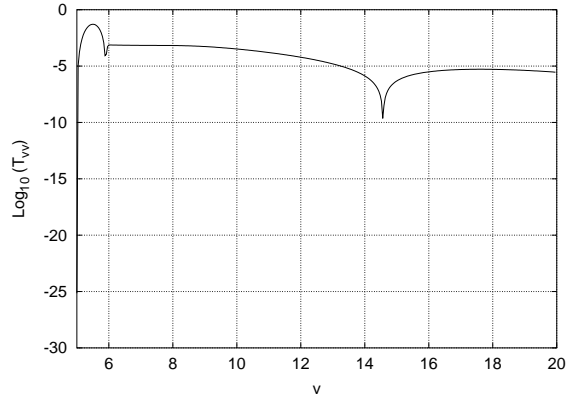
Note that we formulate the initial condition directly for the flux $T_{vv} = (\Phi_{,v})^2/4\pi$ of the scalar field through the surface $u = u_0$, rather than for Φ itself since T_{vv} has the direct physical meaning. Also remember from section 4.2, that once the flux through the two initial surfaces has been chosen, all other initial conditions are determined by our choice of gauge and the constraint equations.

In our computations we vary the width of the signal $\Delta = (v_1 - v_0)$, and its amplitude A , in a broad range. In fig. 4.7 is seen a typical example of the evolution of the scalar field Φ for the case of $\Delta = 1.00$, $A = 0.05$. Fig. 4.7(a) and 4.7(b) represents the evolution of the flux T_{vv} of the scalar energy into the black hole. Fig. 4.7(c) and 4.7(d) shows the T_{uu} flux which arises as a result of T_{vv} being scattered by the spacetime curvature. In fig 4.7(a)-4.7(b) the initial pulse (between $5.0 < v < 6.0$) and subsequent tails with resonances are clearly seen. In different regions, T_{uu} and T_{vv} are converted into one another due to curvature and resonances. In some regions, T_{vv} is locally greater than T_{uu} , it is especially noted that the highest local flux is T_{vv} inside the pulse (between $5.0 < v < 6.0$, fig. 4.7(b)).

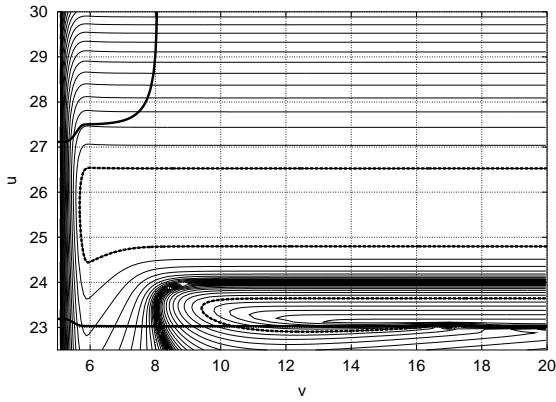
We will now consider some direct effects related to these fluxes.



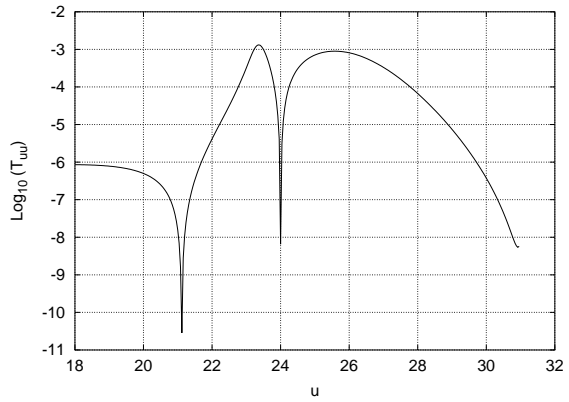
(a) Lines of constant $\log_{10}(T_{vv})$. Lines are from $\log_{10}(T_{vv}) = -10.05$ to $\log_{10}(T_{vv}) = -0.85$ in $\Delta \log_{10}(T_{vv}) = 0.20$ intervals. Thick dotted line marks $\log_{10}(T_{vv}) = -5.45$. Fully drawn thick line marks apparent horizon.



(b) $\log_{10}(T_{vv})$ along $u = 26.00$.



(c) Lines of constant $\log_{10}(T_{uu})$. Lines are from $\log_{10}(T_{uu}) = -10.0$ to $\log_{10}(T_{uu}) = -2.00$ in $\Delta \log_{10}(T_{uu}) = 0.25$ intervals. Thick dotted line marks $\log_{10}(T_{uu}) = -3.25$. Fully drawn thick line marks apparent horizon.



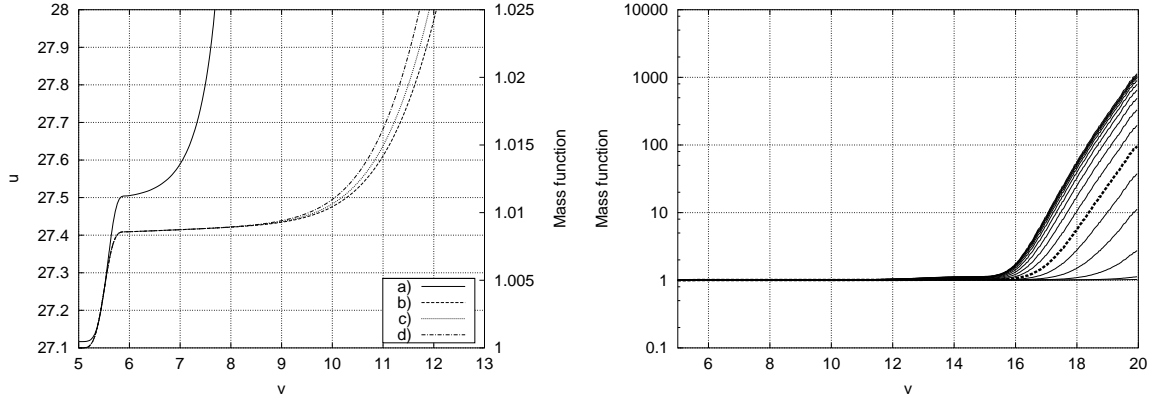
(d) $\log_{10}(T_{uu})$ along $v = 10.00$.

Figure 4.7: T_{vv} and T_{uu} for the simple compact pulse, case: $\Delta = 1.0$, $A = 0.05$.

Focusing effects

One of the first noticeable effect is that the initial pulse T_{vv} leads to an initial change of the outer apparent horizon (OAH) and inner apparent horizon (IAH) in the region within the pulse itself, e.g. $5 < v < 6$ for fig 4.7. In fig. 4.8(a), it can be seen that the mass function, m (eq. (4.22)) near the IAH increases correspondingly as the IAH moves from $u \approx 27.12$ to $u \approx 27.51$. A similar change can be seen for the OAH in the same region (e.g. fig. 4.9(a)). The increase of the mass function and the change of the apparent horizons in this region is the trivial effect of mass being pumped into the black hole by the T_{vv} -flux of the initial pulse.

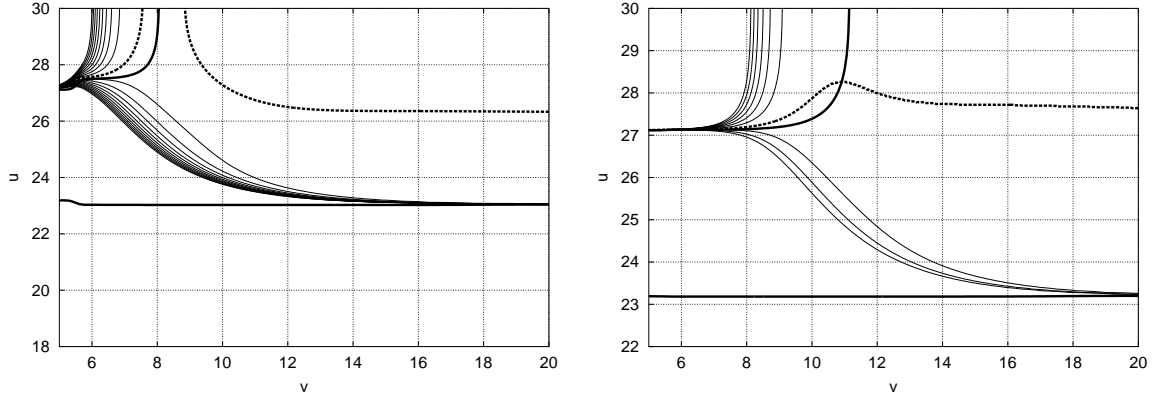
The dramatic change of the IAH at $v \approx 7 - 8$, however, is related with other nonlinear effects. We remember that worldlines of imaginary test photons along $u = \text{const}$ and $v = \text{const}$ are under action of the gravity of the radiation T_{vv} and T_{uu} , which leads to a focusing



(a) IAH and mass function. Line a) is the IAH (left and bottom axis). Lines b)-d) represents the mass function along $u = 27.338$, $u = 27.533$ and $u = 27.884$ respectively (right and bottom axis).

(b) Mass function along lines of constant u . Separation between lines is $\Delta u = 0.40$, bottom line is along $u = 24.00$, top line is along $u = 30.00$, thick dotted line is along $u = 26.00$.

Figure 4.8: Illustrations of the mass function for the simple compact pulse, case: $\Delta = 1.0$, $A = 0.05$.



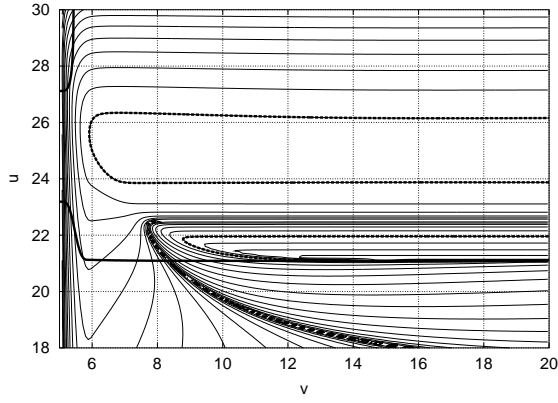
(a) Lines are from $r = 0.680$ (bottom line) to $r = 0.660$ (top left line) in $\Delta r = 0.001$ increments. Thick dotted line is $r = 0.669$.

(b) Lines are from $r = 0.68710$ to $r = 0.68665$ in $\Delta r = 5 \cdot 10^{-5}$ increments. Thick dotted line is $r = 0.68690$.

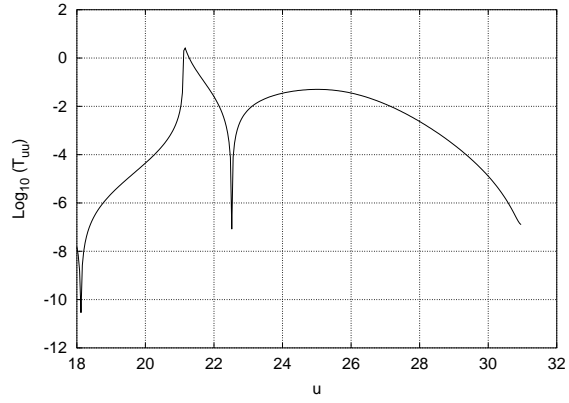
Figure 4.9: Lines of constant r for the simple compact pulse, cases (a): $\Delta = 1.0$, $A = 0.05$ and (b): $\Delta = 1.0$, $A = 0.01$. Fully drawn thick line marks apparent horizon.

effect. For example, in the absence of scalar radiation, outgoing photons along $u = \text{const}$ slightly above of the IAH will go to greater r as $v \rightarrow \infty$ in the Reissner-Nordström solution. With the existence of scalar radiation, a similar outgoing ray initially slightly above the IAH will now, because of the focusing effect of the T_{vv} and T_{uu} radiation, go to smaller r and generate a maxima $(\frac{du}{dv} = 0)_{r=\text{const}}$ which correspond to the position of the IAH. This is seen in fig. 4.9(a) and more clearly in fig. 4.9(b). This effect leads to a drastic change of the shape of the IAH. It is seen by lines c) and d) in figure 4.8(a) that this change of the IAH in this region ($v \approx 7 - 8$) is not accompanied by any significant change of the mass function. About the increase of the mass function at $v > 8$ see below.

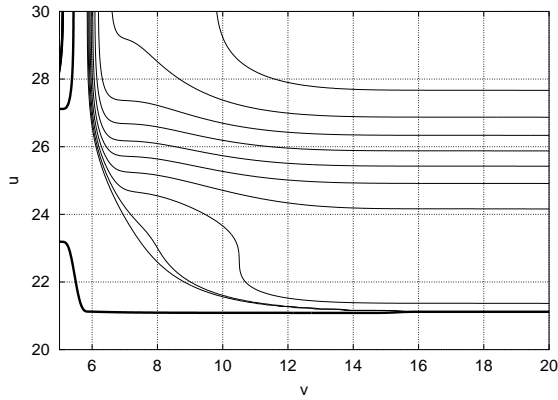
In the case of smaller initial amplitude of the pulse A , the change of the shape of IAH due



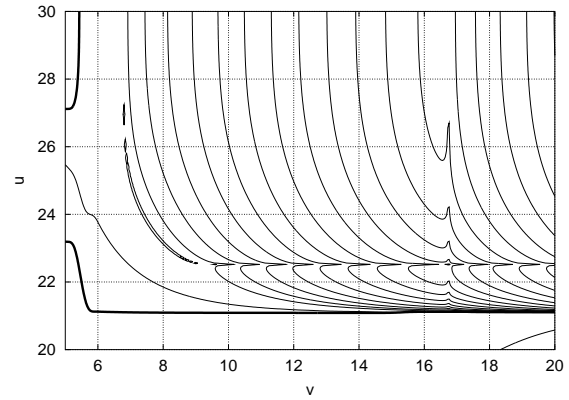
(a) Lines of constant $\log_{10}(T_{uu})$. Lines are from $\log_{10}(T_{uu}) = -10.0$ to $\log_{10}(T_{uu}) = 0.00$ in $\Delta \log_{10}(T_{uu}) = 0.50$ intervals. Thick dotted line marks $\log_{10}(T_{uu}) = -1.50$ (decreasing “outwards”). Fully drawn thick line marks apparent horizon.



(b) $\log_{10}(T_{uu})$ along $v = 15.00$



(c) Lines of constant r . Lines are from $r = 0.520$ (bottom left line) to $r = 0.475$ (top right line) in intervals of $\Delta r = 0.005$.

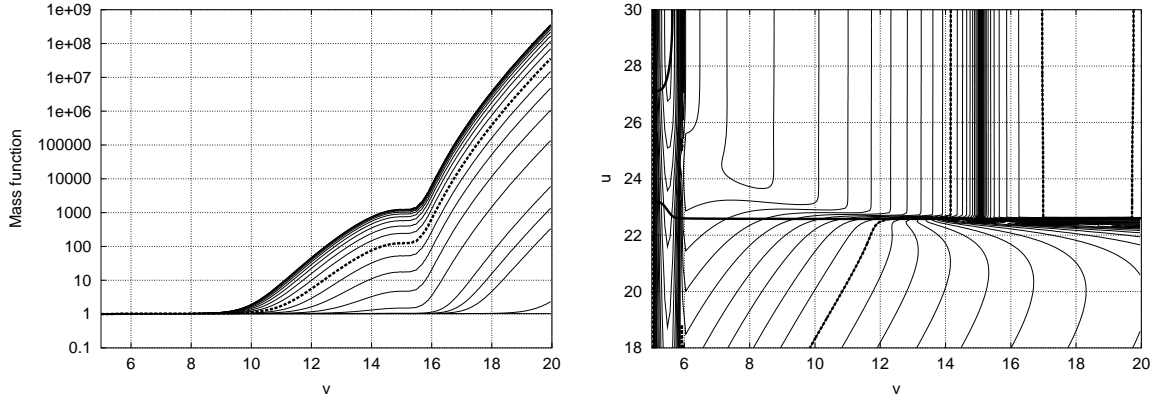


(d) Lines of constant $\log_{10}(T_{\theta\theta})$. Lines are from $\log_{10}(T_{\theta\theta}) = -2.0$ (bottom right line) to $\log_{10}(T_{\theta\theta}) = 32.0$ (top right line) in intervals of $\Delta \log_{10}(T_{\theta\theta}) = 2.0$.

Figure 4.10: Various contour plots for the simple compact pulse, case: $\Delta = 1.0$, $A = 0.20$

to focusing starts later. For example, for the case $\Delta = 1$, $A = 0.01$ (see figure 4.9(b)), the change starts at $v \approx 10$. In this case the change of the OAH and IAH in the region $5 < v < 6$, related to the initial pulse of the scalar field, is so small that it is invisible in the figure.

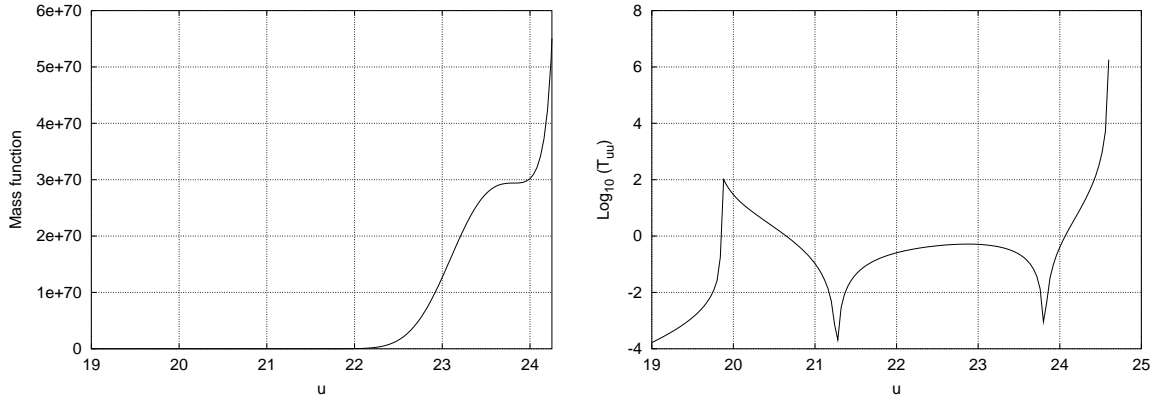
In figs. 4.10(a)-4.10(c) (case: $\Delta = 1.0$, $A = 0.2$) one can see another manifestation of the focusing effect related with the change of the flux T_{uu} . The figures shows close correspondence between T_{uu} and the rate of focusing of lines of constant r . Especially we note that along the line $u \approx 22.5$ for $v > 8$ there is a minimum of T_{uu} (seen by the collection of very closely spaced lines in fig. 4.10(a) and as the local minima in fig. 4.10(b)). Comparing with figure 4.10(c) we see that the lines of $r = const$ shows minimal focusing along this minima, compared to the focusing at $u < 22.5$ and $24 < u < 28$. At $u > 28$ there is a decrease of T_{uu} and we see a corresponding decrease of the focusing effect.



(a) Mass function along lines of constant u . From $u = 22.40$ (bottom line) to $u = 30.00$ (top line) in $\Delta u = 0.40$ intervals. Thick dotted line is along $u = 26.00$.

(b) Lines of constant $\log_{10}(T_{vv})$. Lines are from $\log_{10}(T_{vv}) = -10.0$ to $\log_{10}(T_{vv}) = -0.25$ in $\Delta \log_{10}(T_{vv}) = 0.25$ intervals. Thick dotted line marks $\log_{10}(T_{vv}) = -4.75$. Fully drawn thick line marks apparent horizon. Closely spaced lines near $v \approx 15$ inside apparent horizon marks local minima.

Figure 4.11: Plots for the simple compact pulse, case: $\Delta = 1.0$, $A = 0.10$.



(a) Mass function along $v = 20.00$.

(b) $\log_{10}(T_{uu})$ along $v = 20.00$.

Figure 4.12: Plots for the simple compact pulse, case: $\Delta = 2.0$, $A = 0.20$.

We should also remember that in the dynamic equations (equations (4.10)-(4.12)) and the expression for $T_{\theta\theta}$, (eqs. (4.5) + (4.7)) the scalar field appears only in the form of the product $\Phi_{,u}\Phi_{,v}$ and the same nonlinear effects can be described in terms of $T_{\theta\theta}$ component which is presented in fig. 4.10(d). For example, where T_{uu} has its minima, a corresponding effect is clearly visible in fig. 4.10(d). We also note from fig. 4.10 that for this case the initial pulse is so strong that its flux changes the IAH inside the pulse and there are no double turns as it was seen on fig. 4.7.

Mass function

Let us come now to the discussion of the behaviour of the mass function m . As we remember, the (modest) increase of m in the region $5 < v < 6$ in fig. 4.8(a) is related to the

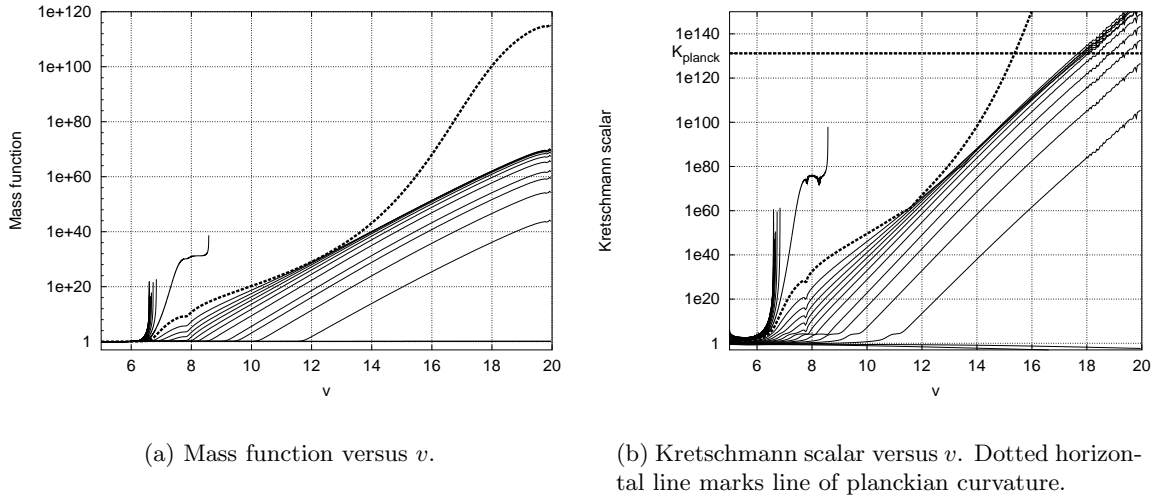


Figure 4.13: Mass function and Kretschmann scalar along lines of constant u for the simple compact pulse, case: $\Delta = 2.0, A = 0.2$. Separation between lines is $\Delta u = 0.40$. Lines are from $u = 19.40$ (lowest right line) to $u = 29.80$ (near vertical line in lower left corner). Thick dotted line is along $u = 24.60$.

input of the energy in the initial pulse. The increase of m seen in the region $8 < V < 15$ in fig. 4.8 is related partly with the compression-effect (see section 4.3), but still it is very difficult to separate this effect from the beginning of the mass inflation. The essentially faster increase of m at $v > 15$ (fig. 4.8(b)) is the manifestation of the mass inflation when we come to the CH.

Mass inflation depends mainly on the T_{vv} flux but also on the T_{uu} flux and, as described in section 4.3, the co-existence of both fluxes is essential for mass inflation to occur. An example of the dependence on T_{vv} is seen in fig. 4.11 (case $\Delta = 1.0, A = 0.10$). It is seen that where T_{vv} has a minimum (the narrowly spaced lines at $v \approx 15$) the increase of m almost stops. Fig. 4.12 demonstrates the dependence of mass inflation on T_{uu} for the stronger pulse: $\Delta = 2.0, A = 0.20$. This pulse is so strong that a $r = 0$ singularity is formed in the domain (this is further discussed in the next subsection). At the minimum of T_{uu} at $u \approx 23.8$ the increase of m also stops and at $u > 24$ where T_{uu} increases rapidly, m also has similar rapid increase. However, the line plotted terminates at the $r = 0$ singularity, thus the final rapid increase of mass is a combination of the effects of compression and mass inflation.

The compression effect can be more clearly seen in fig. 4.13(a), which shows m , along lines of constant u , again for the case $\Delta = 2.0, A = 0.2$. When one comes to the $r = 0$ singularity, compression tends to infinity and we see catastrophic infinite increase of m . This can be seen by the near vertical lines in the lower left in the figure, which represents lines of high u . These lines experience a catastrophic infinite increase of mass as they approach $r = 0$, as indicated by these lines being near vertical.

The remaining right hand side lines which run in all the range $5 < v < 20$, represents lines of constant u which reach the CH and the mass increase along those lines are due to the mass inflation. The line marked by thick dashes represent a line that comes close to the point where the $r = 0$ and CH singularities meet. The structure of this line is more complicated as it is influenced by both processes.

Finally, in fig. 4.13(b) is seen the Kretschmann scalar for the same lines.

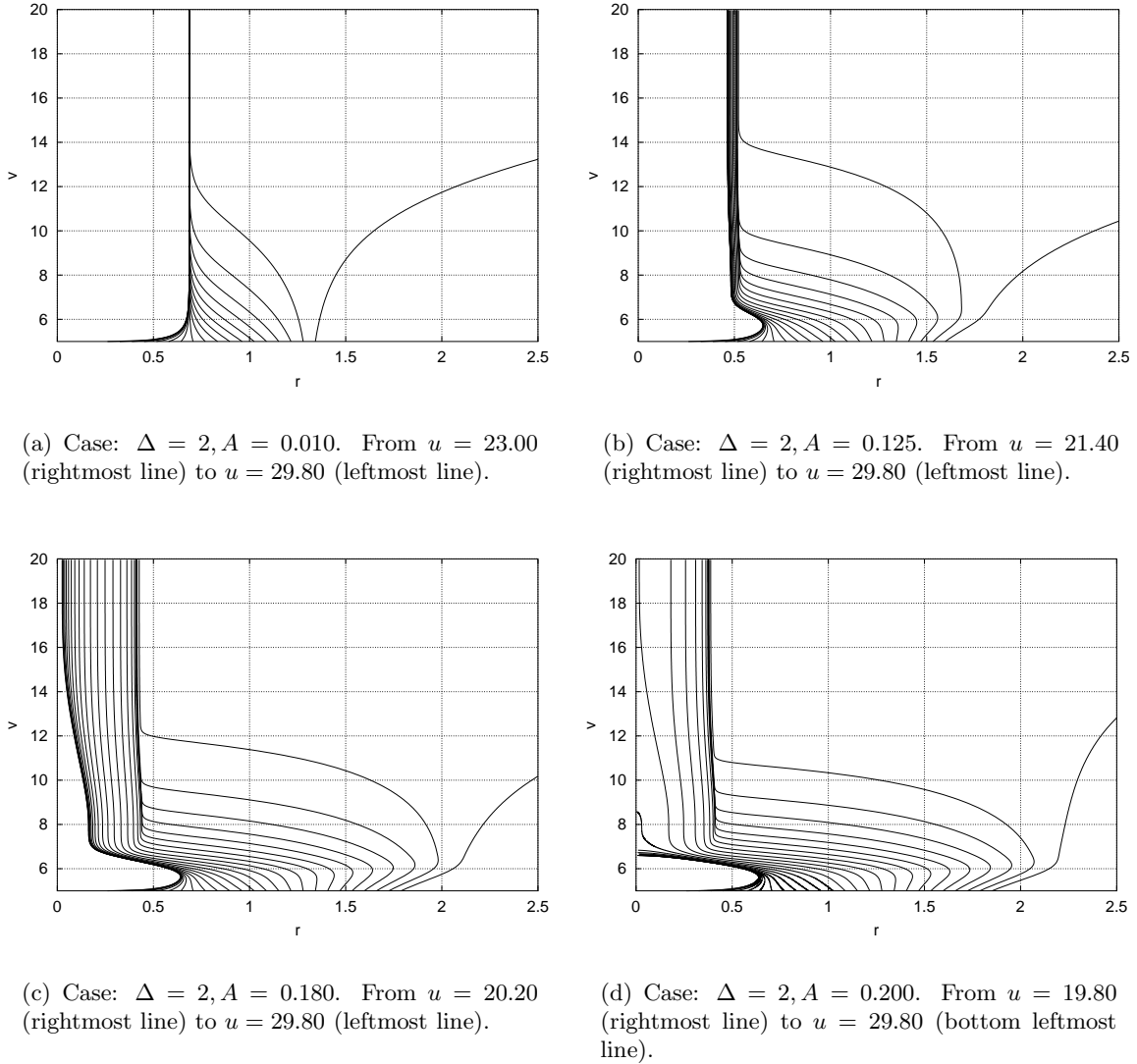
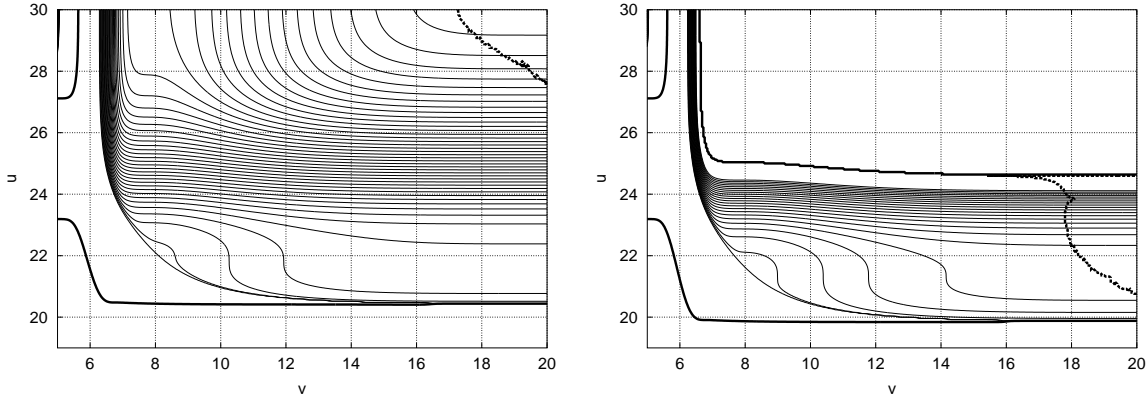


Figure 4.14: v versus r along lines of constant u for amplitudes for the simple compact pulse. Separation between lines of constant u is $\Delta u = 0.40$.

The singularity

Now we will discuss the singularity. When the initial pulse is rather weak we cannot see the manifestation of the spacelike singularity in our computational domain. However, we can see the asymptotic approach of $u = \text{constant}$ test photons to the CH singularity. In fig. 4.14(a) we see that for the case $\Delta = 2.0, A = 0.01$, all our test photons come asymptotically to the same value at $r \approx 0.69$, corresponding to the analytical value for r at the CH for the pure Reissner-Nordström solution, i.e. the CH singularity itself does not show any tendency to shrink down (within our computational domain).

With an increase of the amount of energy in the initial pulse one can observe a nonlinear effect of shrinkage of the CH-singularity under the action of the gravity of the irradiating flux T_{uu} together with the T_{vv} flux. In fig. 4.14(b) (case $\Delta = 2.0, A = 0.125$) the test photons with greater $u = \text{constant}$ comes asymptotically to smaller values of r and in fig. 4.14(c) (case $\Delta = 2.0, A = 0.180$) the pulse is so strong that the CH almost (but not quite) shrinks down to $r = 0$.



(a) Case: $\Delta = 2.0$, $A = 0.18$. Lines are from $r = 0.45$ (bottom left line) to $r = 0.03$ (top right line) in intervals of $\Delta r = 0.01$

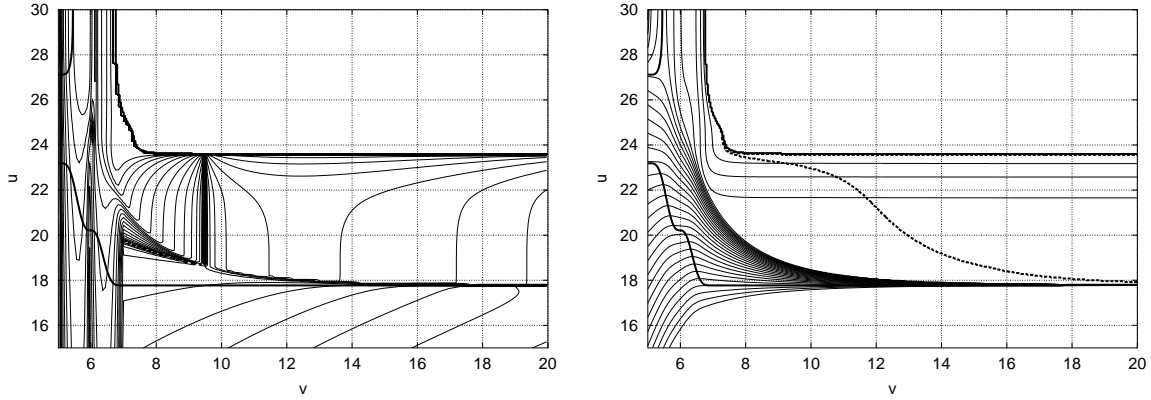
(b) Case: $\Delta = 2.0$, $A = 0.20$. Lines are from $r = 0.42$ (bottom left line) to $r = 0.20$ (top right line) in intervals of $\Delta r = 0.01$. Top right thick line mark $r = 0$ singularity.

Figure 4.15: Lines of constant r for two different simple compact pulses. Thick dotted lines in right part of the figures represents line of planckian curvature. Bottom fully drawn thick line marks OAH.

In fig. 4.14(d) (case $\Delta = 2.0, A = 0.200$) one can see both the manifestation of the shrinkage of the CH singularity (photons with higher u come asymptotically to smaller r) and existence of the $r = 0$ singularity (photons with the highest u come to $r = 0$).

Figure 4.15 shows lines of constant r and the position of $K = K_{planck}$ (marked by the thick dotted line) for the two strongest cases from fig. 4.14. We remember that this line and places with higher K should be considered as a singularity from the point of view of classical physics. Thus, for both these cases the physical singularity is placed at finite values of v and is not a null singularity. In fig. 4.15(b) we furthermore see the $r = 0$ spacelike singularity inside of our computational domain. This singularity can be considered as a result of mutual gravitational focusing of T_{vv} and T_{uu} fluxes in the region between inner and outer apparent horizons. At small $v < 15$ the physical singularity practically coincide with $r = 0$, but for $v > 17$ we see that the spacetime structure of the physical singularity is quite different from the structure of the mathematical singularity. The physical singularity here depends mainly on the true CH-singularity, but its position in the $u - v$ diagram is quite different from the position of the true CH-singularity which is at $v = \infty$.

This can also be compared with fig. 4.13(b) from which we see different behaviours of K for the test photons for the strong case of $\Delta = 2.0, A = 0.200$. The lines in the lower left hand corner, sharply increasing to near vertical, are the lines which come to $r = 0$. The thick dotted line is the line which comes to a point at the singularity close to the meeting of the $r = 0$ and CH singularities. The remaining lines in the right hand side are the lines which come to the CH-singularity.



(a) Lines of constant $\log_{10}(T_{vv})$. Lines are from $\log_{10}(T_{vv}) = -10.0$ to $\log_{10}(T_{vv}) = 2.0$ in intervals of $\Delta \log_{10}(T_{vv}) = 0.50$.

(b) Lines of constant r . From $r = 3.00$ (bottom line) to $r = 0.10$ (top right thin line) in $\Delta r = 0.10$ intervals. Thick dotted line marks $K = K_{planck}$.

Figure 4.16: Contour lines for double sine pulse of form of eq. (4.42), case $\Delta = 2.0, A = 0.25$. Thick bottom line is AH, thick upper line is $r = 0$.

4.5.2 Double sine pulse

In this subsection we choose the ingoing flux to be of the form:

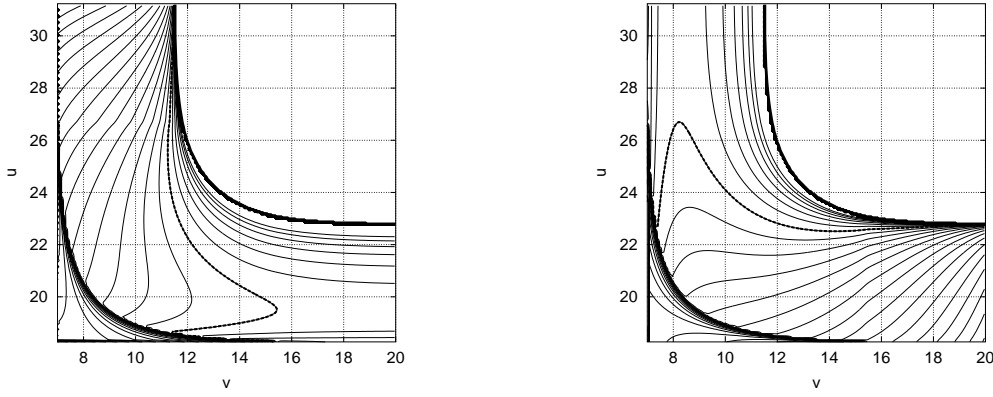
$$\Phi_{,v}(u_0, v) = \sqrt{6} A \cos\left(\pi \frac{v - v_0}{v_1 - v_0}\right) \sin\left(\pi \frac{v - v_0}{v_1 - v_0}\right)^2 \quad (4.42)$$

instead of equation (4.40). This readily integrates to give the initial expression for $\Phi(u_0, v)$:

$$\Phi(u_0, v) = \frac{\sqrt{\frac{2}{3}} A (v_1 - v_0) \sin\left(\pi \frac{v - v_0}{v_1 - v_0}\right)^3}{\pi} \quad (4.43)$$

where v_0 and v_1 as before, marks the beginning and end of the pulse respectively and A is the amplitude of the pulse. Also, as before we set $\Phi_{,v}(u_0, v) = 0$ for $v > v_1$. The pulse is scaled in such a way that for a given width $\Delta = v_1 - v_0$ and amplitude A , the integral of the initial flux, $\int_{v_0}^{v_1} T_{vv} dv$, is equal for pulses of the form (4.40) and (4.42). Eq. (4.42) has the shape of a double pulse, rather than (4.40) which is the shape of a single initial pulse. This pulse is more complicated than (4.40), but is similar in shape to the pulse shapes used in some other papers (e.g. [28, 29]).

We have performed a series of computations based on eq. (4.42) (all other initial conditions equal to those in the previous subsection). The results of these computations demonstrate a more complex picture of interplay between the scalar fluxes than in the case of subsection 4.5.1. This is natural because of the more complex shape of the initial pulse. But the main physics and principal properties of the singularities are the same in the two cases. An example illustrating the increased complexity in structure of the fluxes can be seen in figure 4.16, which illustrates the T_{vv} flux for the case: $\Delta = 2.0, A = 0.25$. The shapes of the apparent horizons and the central singularity $r = 0$ are now more complex as well as the distribution of the T_{vv} field. Still the general characters of the $r = 0$ and the physical $K = K_{planck}$ singularities are the same.



(a) Lines of constant $\log_{10}(T_{uu})$. Lines are from $\log_{10}(T_{uu}) = -10.0$ to $\log_{10}(T_{uu}) = 3.00$ in $\Delta \log_{10}(T_{uu}) = 0.25$ intervals. Thick dotted line marks $\log_{10}(T_{uu}) = 1.50$, decreasing leftwards.

(b) Lines of constant $\log_{10}(T_{vv})$. Lines are from $\log_{10}(T_{vv}) = -10.0$ to $\log_{10}(T_{vv}) = 3.00$ in $\Delta \log_{10}(T_{vv}) = 0.25$ intervals. Thick dotted line marks $\log_{10}(T_{vv}) = 1.50$, decreasing downwards.

Figure 4.17: Contours for the double-flux case based on the simple compact pulse: $\Delta = 2.0$, $A = 0.25$. Thick top right line marks $r = 0$.

4.5.3 The influence of the T_{uu} flux

So far in all our analyses we have assumed that the flux of the scalar field T_{uu} through $v = v_0$ was zero and that any T_{uu} -flux arised only as a result of scattering of the T_{vv} -flux by the curvature of the spacetime. Now we would like to consider the influence of a T_{uu} -flux through the surface $v = v_0$. To do this we will consider an extreme case when T_{uu} through $v = v_0$ is equal exactly to T_{vv} through $u = const$ just inside of a black hole. More concretely we do the following; We specify some initial $\Phi(u_0, v)$ along $u = u_0$ with a pulse width $\Delta = v_1 - v_0$ and amplitude A and set all initial conditions equal to those in subsection 4.5.1, including $\Phi_{,u}(u, v_0) = 0$ along $v = v_0$. These initial data are then simulated as usual, however only in the computational domain of $5 < v < 20$ and $0 < u \leq u_{AH}$, where u_{AH} is the first computational point which is inside of the outer apparent horizon along $v = v_1$. Because of scattering of the initial pulse there is now a T_{vv} flux into the black hole along the line $u = u_{AH}$ for $v > v_1$. We then stop the computation and start a new with the following domain of integration: $v_1 \leq v \leq 20$ and $u_{AH} \leq u \leq u_{max}$ (where $u_{max} - u_{AH} = (20 - v_1)$). Along the (new) outgoing initial hypersurface, $u = u_{AH}$, all the variables are kept as they were in the original simulation, while along the (new) ingoing initial hypersurface, $v = v_1$, initial data are set equal to the data along the outgoing hypersurface, hence we have completely symmetrical initial conditions. Subsequently we performed a computation for the new computational domain. It is obvious that all conditions in this domain are symmetrical with respect to u and v and hence the boundary fluxes T_{uu} along $v = v_1$ and T_{vv} along $u = u_{AH}$ must be exactly equal.

We performed our computations for the compact simple pulses (eq. (4.40)) for different parameters Δ and A . An example of our results can be seen in figs. 4.17 - 4.21 for the case $\Delta = 2.0, A = 0.25$. All pictures are symmetrical with respect to u and v , as they should be. The outer apparent horizon is naturally outside of our computational domain. Figs. 4.17 and 4.18 shows the T_{uu} and T_{vv} distributions and r contour lines. On these figures there is no inner apparent horizon because it coincide with another CH singularity at $u \rightarrow \infty$ (see below). But on fig. 4.18 one can see the mathematical strong singularity $r = 0$ and the

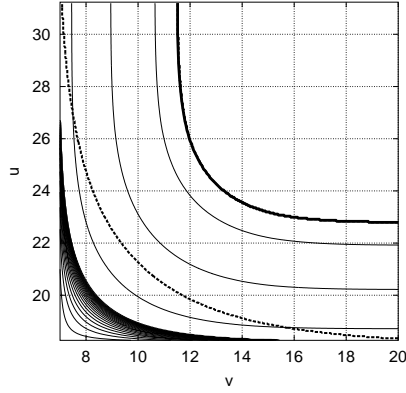
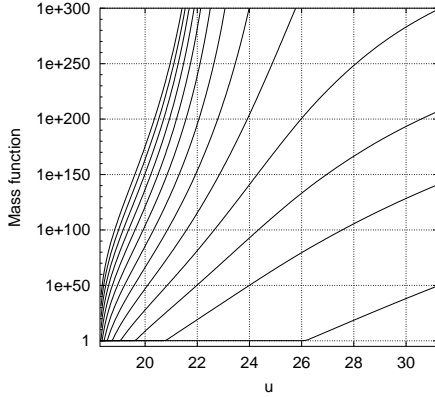
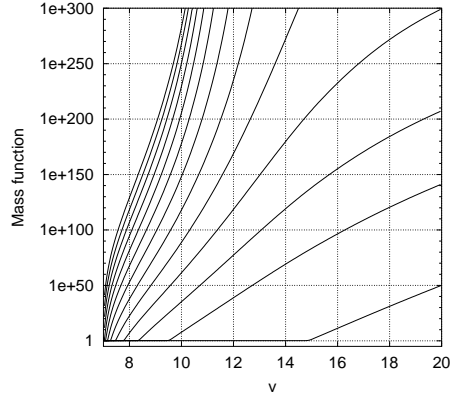


Figure 4.18: Lines of constant r for the double-flux case based on the simple compact pulse: $\Delta = 2.0$, $A = 0.25$. Thick top right line marks $r = 0$. Lines are from $r = 2.50$ (bottom left line) to $r = 0.10$ (top right thin line) in intervals of $\Delta r = 0.10$. Thick dotted line marks $K = K_{planck}$.



(a) Mass function along lines of constant v . Lines are from $v = 7.04$ (bottom right) to $v = 19.04$ (top left) in $\Delta v = 1.0$ intervals.

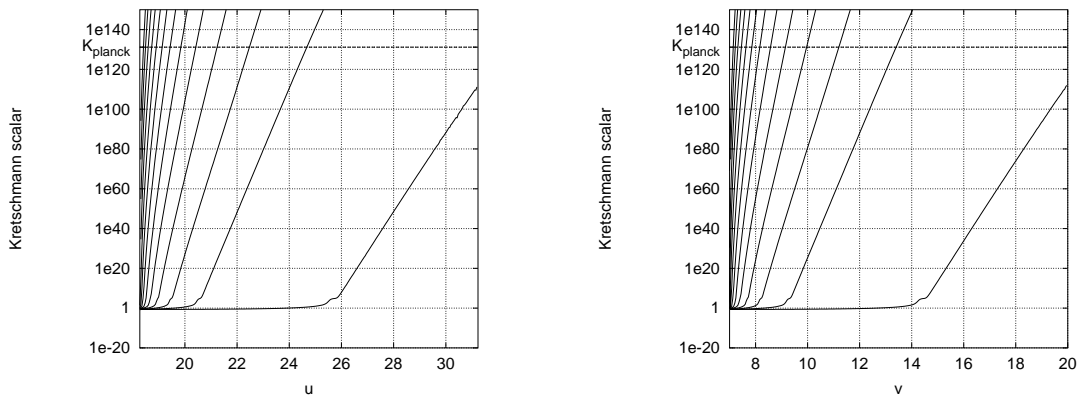


(b) Mass function along lines of constant u , corresponding to the symmetrical equivalent of the lines in fig. 4.19(a).

Figure 4.19: Mass function for the double-flux case double-flux case based on the simple compact pulse: $\Delta = 2.0$, $A = 0.25$

physical singularity (with $K = K_{planck}$) which is reached long before the CH singularity at $u \rightarrow \infty$ and $v \rightarrow \infty$ in most of the computational domain.

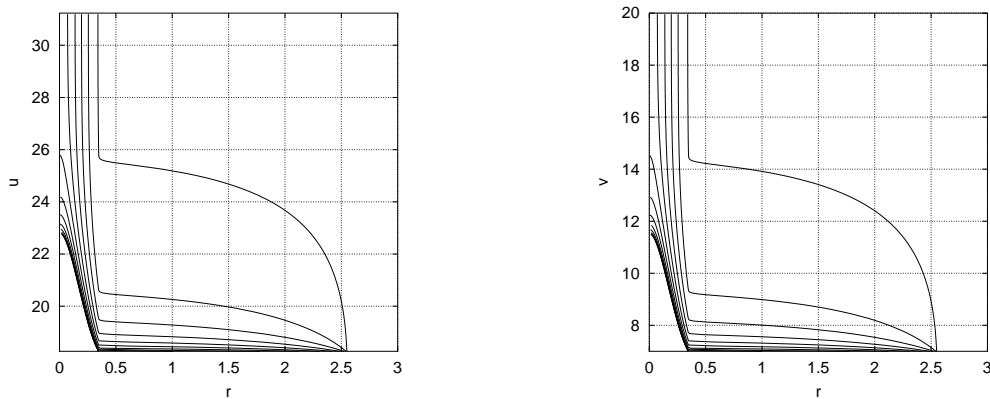
Fig. 4.19 shows the huge increase of the mass function with growing u and v , and fig. 4.20 shows the increase of the Kretschmann scalar as function of u and v up to $K = K_{planck}$. Finally fig. 4.21 shows light signals along $v = const$ and $u = const$ respectively. This figure shows both the existence of null singularities of the CH singularity-type and $r = 0$ singularity. Indeed for example in the case fig. 4.21(a) one can see that for some $v = const$ (the rightmost curves) for $u \rightarrow \infty$, signals goes asymptotically to practically $r = const$ (asymptotically approach to the null singularity at $u \rightarrow \infty$). Smaller asymptotic values r are seen for the signals at bigger v corresponding to the focusing effect. Finally the signals with v big enough, come to the central singularity $r = 0$. The symmetrical picture for the signals with $u = const$ is shown in fig. 4.21(b). Here we see the asymptotic approach to another null singularity at $v \rightarrow \infty$.



(a) Kretschmann scalar along lines of constant v . Lines are from $v = 7.04$ (bottom right) to $v = 19.04$ (top left) in $\Delta v = 1.0$ intervals. Horizontal dashed line is $K = K_{planck}$.

(b) Kretschmann scalar along lines of constant u , corresponding to the symmetrical equivalent of the lines in fig. 4.20(a).

Figure 4.20: Kretschmann scalar for the double-flux case double-flux case based on the simple compact pulse: $\Delta = 2.0$, $A = 0.25$



(a) u vs. r along lines of constant v . Lines are from $v = 7.04$ (rightmost) to $v = 19.04$ (bottom left) in $\Delta v = 1.0$ intervals

(b) v vs. r along lines of constant u , corresponding to the symmetrical equivalent of the lines in fig. 4.21(a).

Figure 4.21: u and v versus r for the double-flux case double-flux case based on the simple compact pulse: $\Delta = 2.0$, $A = 0.25$

Note also the different character of the increase of mass function on fig. 4.19 for lines of big and small v and u respectively. For example on fig. 4.19(a) the topmost lines (big $v = const$) come to the central singularity but lines with small $v = const$ (bottom lines) go to the null singularity at $u \rightarrow \infty$. The different behaviour of these lines correspond to the different nonlinear processes influencing the mass function for lines terminating at the $r = 0$ singularity and reaching the CH singularity.

Thus in this case there are three different singularities inside the black hole: two null singularities at $u \rightarrow \infty$ and $v \rightarrow \infty$ and the physical singularity at $K = K_{planck}$. In addition there is also a central (mathematical) singularity at $r = 0$.

4.6 Conclusions

In this paper we investigated the physics of nonlinear processes inside of the spherical charged black hole, nonlinearly perturbed by a selfgravitating, minimally coupled, massless scalar field. For this purpose we created and tested a numerical code which is stable and second-order accurate. For our computations we used an adaptive mesh refinement approach in ingoing u -direction.

The following nonlinear physical processes are important inside the black hole: Scattering of radiation by the curvature of the spacetime, gravitational focusing effect, mass inflation and squeeze of matter with pressure.

At the beginning of our analysis we used a homogeneous approximation to clarify some physical processes near a spacelike singularity. In this approximation one supposes that near the singularity temporal gradients are much higher than the spatial gradients, so one assumes that all processes depend on the time coordinate only (uniform approximation). We used both analytical analyses and a numerical approach to analyse three different physical matter contents: dust, a massless scalar field and an ultrarelativistic gas.

For the case $P = 0$ (dust) we found that the singularity is at $r = r_{sing} \neq 0$, $r_{CH} < r_{sing} < r_{EH}$, where r_{CH} and r_{EH} are the positions of the Cauchy Horizon and the Event Horizon when there are no dust at all. The value r_{sing} decreases monotonically with a decrease of the matter contents and tends to $r_{sing} = r_{CH}$ when the matter contents goes to zero.

In the case of the scalar field, the uniform approximation demonstrates a more complex behaviour. Here the scalar field can be represented as a sum of two equal fluxes moving in opposite directions. One can for this case see the manifestation of both the effect of mass inflation and the effect of shrinkage of the CH down to $r = 0$. For very small matter contents ($\epsilon_0 \ll 0.01$) the Kretschmann scalar, K , becomes equal to the Planck value at r close to r_{CH} . So in this case the physical singularity (when $K = K_{planck}$) is at $r \approx r_{CH}$. For larger values of ϵ_0 , (e.g. $0.01 \lesssim \epsilon_0 \lesssim 0.03$), the CH does not manifest itself and the model squeezes to r very close to $r = 0$ before K reaches K_{planck} . It means that for these values of ϵ_0 , the physical singularity practically coincides with $r = 0$. For rather big ϵ_0 , K reaches K_{planck} at rather big r as it was for the case of dust, $P = 0$.

In the case of matter with isotropic relativistic pressure, $P = \epsilon/3$, we have the situation intermediate between $P = 0$ and the scalar field. The physical singularity, in this case, is located at r essentially greater than $r = 0$.

We performed the analysis of the full nonlinear processes inside the spherical charged black hole with a scalar field using the numerical approach. This analysis extends the analysis of the earlier works [10, 14, 15] and reveal new aspects of the problem. The detailed description of the results is given in section 4.5. We analysed nonlinear gravitational interaction of the fluxes of the scalar field, the dependence of the effects on the boundary conditions, analysed the focusing effects, mass inflation and squeeze effect and the behaviours of the Kretschmann scalar K . We payed special attention to the analysis of the singularity in subsection 4.5.1. We investigated the focusing of the CH singularity and its dependence on the boundary conditions. We determined the position of the physical singularity (where $K = K_{planck}$) inside the black hole and demonstrated that this position is quite different from the positions of the mathematical $r = 0$ singularity and CH singularity.

The results mentioned above were obtained with the scalar flux into the black hole in the form of a simple compact sine-pulse with different amplitudes and widths.

We also analysed the physics in the case of a scalar flux in the form of a double sine-pulse qualitatively similar to the usage in [28, 29]. In this case physics is more complicated, but the main characteristics of the results are the same as for the simple pulse.

Finally we investigated the influence of the boundary T_{uu} -flux on the physics of the

singularity. We demonstrated that it is possible to have the existence of three different singularities inside the black hole: two null singularities at $u \rightarrow \infty$ and $v \rightarrow \infty$ and the physical singularity $K = K_{planck}$ in addition to a central mathematical singularity $r = 0$.

4.7 Acknowledgements

This work was supported in part by Danmarks Grundforskningsfond through its support for establishment of the Theoretical Astrophysics Center and by the Danish SNF Grant 21-03-0336. J. Hansen and I. Novikov thanks The University of Chicago for hospitality during their visits.

Appendix 4.A: The numerical code

In this appendix we describe the structure of the numerical code used to obtain the numerical results presented in section 4.5.

Appendix 4.A.1: The numerical scheme

Our approach to numerically integrating the field equations is similar to that of other authors [10, 14–16, 28]. Denoting the three unknowns, r, σ, Φ as h_j with $j = 1, 3$, the three evolution equations (4.10)-(4.12) are each of the form:

$$h_{j,uv} = F_j(h_k, h_{k,v}, h_{k,u}), k = 1, 3 \quad (4.44)$$

We denote four grid points in the (u, v) -domain by $p_1 \equiv (u, v)$, $p_2 \equiv (u, v + \Delta v)$, $p_3 \equiv (u + \Delta u, v)$ and $p_4 \equiv (u + \Delta u, v + \Delta v)$, where Δv and Δu are finite increments in the v and u directions (see fig. 4.22).

By combining a Taylor expansion h_j at these four points (evaluated around an intermediate point $p_5 \equiv (u + \Delta u/2, v + \Delta v/2)$) with eq. (4.44) we find that:

$$\begin{aligned} h_j(p_4) &= h_j(p_3) + h_j(p_2) - h_j(p_1) \\ &\quad + \Delta u \Delta v [F_j(h_k(p_5), h_{k,u}(p_5), h_{k,v}(p_5))] \\ &\quad + \frac{\Delta u^2}{24} h_{j,vuuu}(p_5) + \frac{\Delta v^2}{24} h_{j,uvvv}(p_5) \\ &\quad + O(\Delta u^3, \Delta v^3)], k = 1, 3 \end{aligned} \quad (4.45)$$

i.e. we can evaluate h_j at p_4 with second order accuracy if we know h_j at the four points p_1, p_2, p_3, p_5 and $h_{j,v}, h_{j,u}$ at p_5 . Initially we only know the values of h_j along in- and outgoing null segments (see section 4.2) i.e. for example at p_1, p_2 and p_3 . However, by employing eq. 4.45 twice in a predictor-corrector style we can evaluate $h_j, h_{j,v}, h_{j,u}$ at p_5 with the desired accuracy and hence subsequently find h_j at p_4 .

Equation (4.45) constitutes the heart of our code. As described in section 4.2, the values of the unknown functions along the initial hypersurfaces u_0, v_0 are given by the constraint equations (4.8) and (4.9). We can then use our numerical scheme to calculate the values of h_j along the ingoing ray $v = v_0 + \Delta v$ starting at the point $u = u_0 + \Delta u$, then solving for $u = u_0 + 2\Delta u$ etc. until we reach the last grid point at $u = u_{final}$. Using the (now known) values of h_j along $v = v_0 + \Delta v$, we can then calculate the unknowns along the next ingoing ray along $v = v_0 + 2\Delta v$ and so on throughout our computational domain until we reach the end of our computational domain at $v = v_{final}$.

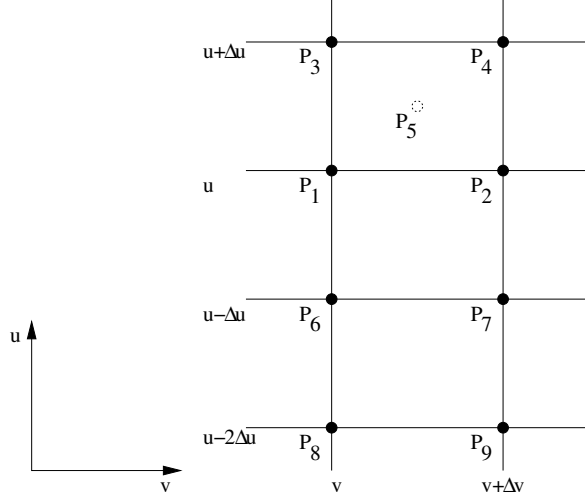


Figure 4.22: Schematic of the points used in the numerical scheme.

Appendix 4.A.2: Splitting algorithm

When outside the event horizon (EH), the scheme described above works reasonably good as it is, but when the domain of integration crosses the EH, the unknown functions exhibits extremely great gradients. This can be seen by considering two outgoing rays, one just inside and one just outside of the EH. One ray is destined to be trapped inside the EH, while the other must escape to infinity, i.e. regardless of how close the two rays were initially, their distance will diverge as their advanced time v grows. Integration across such great gradients using fixed increments in u and v would cause the numerical errors to explode unless the initial increments were chosen to be unrealistically small. To overcome this difficulty an adaptive mesh refinement (AMR) approach is crucial for an accurate integration of the field equations. However, the strong gradients are mainly in the ingoing u -direction, hence AMR is most important in this direction. While AMR in both v and u directions would be desirable, implementation of AMR in only one direction, while much less complicated, still produces good results. This is supported by other authors who also employ uni-directional AMR [16, 28].

To determine whether AMR is needed and a cell should be split (or possibly desplit), we focus on the truncation error in the numerical scheme. As can be seen from equation (4.45), the primary error introduced by the scheme comes mainly from the terms:

$$\epsilon_j^u(p_5) = \frac{\Delta u^2}{24} h_{j,vuuu}(p_5) \quad (4.46a)$$

$$\epsilon_j^v(p_5) = \frac{\Delta v^2}{24} h_{j,uvvv}(p_5) \quad (4.46b)$$

Since we use AMR only in the ingoing u direction, thus keeping Δv constant, we can only control $\epsilon_j^u(p_5)$ by splitting, hence we will focus on this term. By introducing four new points: $p_6 \equiv (u - \Delta u, v)$, $p_7 \equiv (u - \Delta u, v + \Delta v)$, $p_8 \equiv (u - 2\Delta u, v)$, $p_9 \equiv (u - 2\Delta u, v + \Delta v)$, (see fig. 4.22), we can estimate $h_{j,vuuu}$ (and hence ϵ_j^u) at p_5 with the following finite difference

operator:

$$\begin{aligned}
h_{j,vuuu}(p_5) = & \Delta v \Delta u^3 \left(3h_j(p_1) - 3h_j(p_3) \right. \\
& - 3h_j(p_6) + 3h_j(p_7) - h_j(p_2) + h_j(p_4) \\
& \left. + h_j(p_8) - h_j(p_9) \right) + O(\Delta u)
\end{aligned} \tag{4.47}$$

In practice we proceed as follows; Following a calculation of h_j at p_4 we use eq. (4.46a) + (4.47) to estimate the error $\epsilon_j^u(p_5)$ involved in the calculation and compare it to $F_j(h_k(p_5), h_{k,u}(p_5), h_{k,v}(p_5))$ in eq. (4.45) for each of the variables, $j = 1, 3$. We now require that the relative error should be within some fixed interval:

$$S_{desplit} < \frac{\epsilon_j^u(p_5)}{F_j(h_k(p_5), h_{k,u}(p_5), h_{k,v}(p_5))} < S_{split} \tag{4.48}$$

If the relative error is greater than the threshold parameter S_{split} we perform a split. Conversely, if the relative error is less than the threshold parameter $S_{desplit}$ a desplit is made. Note that because we need knowledge of the points p_6 to p_9 to calculate the relative error, we don't use splitting for the first two cells $u < u_0 + 2\Delta u$ on a given ingoing ray.

If a split is required a new point is introduced at $p'_3 \equiv (u + \Delta u/2, v)$. The values of h_j at p'_3 are then found by a four-point interpolation scheme (using data from the two points above and the two below p'_3). The numerical scheme is then used to calculate h_j at $p'_4 \equiv (u + \Delta u/2, v + \Delta v)$ using the points p_1, p_2 and p'_3 . If a desplitting is needed the reverse process takes place, i.e. p_3 is deleted and the point above is used in its place.

To obtain the results presented in section 4.5, the splitting thresholds were set to $S_{split} = 10^{-7}$, $S_{desplit} = 10^{-9}$. The resolutions along the initial outgoing null segment were set to $\Delta u = 1/100$ and $\Delta v = 1/12800$. The initial value of Δu can be set rather low, since the splitting algorithm will assure that Δu always have an appropriate value. The value of Δv on the other hand, is constant throughout the computational domain and must initially be chosen to have a suitable value everywhere. The high value of Δv has been chosen such that Δv is as comparable to Δu in large parts of the interior of the black hole. This has been verified by numerical tests to give the best results.

Appendix 4.B: Analysis of the code

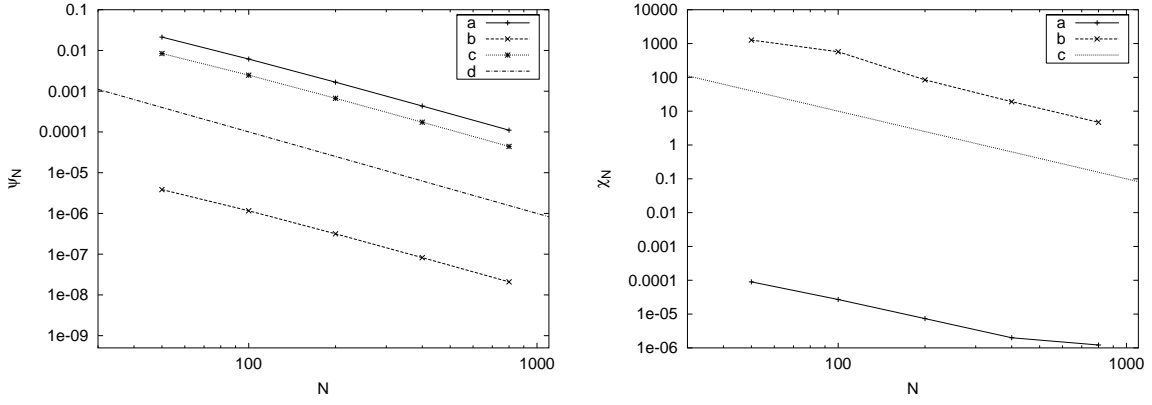
We have tested the code and found it to be stable and second-order accurate. Here we presents tests to demonstrate this.

Appendix 4.B.1: Basic convergence tests

We test the basic convergence properties of the code by performing simulations with the same initial conditions, but with varying resolutions and with the splitting algorithm disabled. As initial conditions we use a Reissner-Nordström spacetime (with initial mass $m_0 = 1$ and charge $q = 0.95$) which is perturbed by a massless scalar field. We set the specific form of the scalar field along the initial outgoing null segment in the interval $v_0 \leq v \leq v_1$ to be:

$$\Phi(u_0, v) = \frac{A}{4\pi} \left(2\pi(v - v_0) - (v_1 - v_0) \sin \left(2\pi \frac{v - v_0}{v_1 - v_0} \right) \right) \tag{4.49}$$

with $A = 0.05$ and $v_0 = 5, v_1 = 6$. For $v > v_1$ we set Φ constant to $\Phi(u_0, v) = \Phi(u_0, v_1)$. Along the ingoing null segment $v = v_0$ we specify $\Phi_{,u}(u, v_0) = 0$ (these initial conditions are



(a) Line a) $\psi_N(r)$, b) $\psi_N(\Phi)$ and line c) $\psi_N(\sigma)$. Line d) shows a line with a slope of minus two. (b) Line a) $\chi(C_1)$ and b) $\chi(C_2)$. Line c) shows a line with a slope of minus two

Figure 4.23: Demonstration of the convergence (without AMR) of r , Φ , σ , C_1 and C_2 along an outgoing ray $u = 23.00$.

the same as those used in section 4.5). As domain of integration we used $5 < v < 100$ and $0 < u < 23.05$ and with the gauge choice described in section 4.2.

We make simulations with varying resolutions $N = 1/\Delta u = 1/\Delta v$ and examine data along an outgoing ray $u = 23.00$ which is just outside of the event horizon. Along this ray we calculate the average absolute difference at each data point between the unknown functions for two resolutions along the outgoing ray. We define:

$$\psi_N(x) \equiv \frac{1}{n} \sum_i^n |x_N^i - x_{2N}^i| \quad (4.50)$$

where x_N^i denotes the value of variable x at the i 'th data point (out of a total of n points) from a simulation with resolution N . I.e. we basically calculate the normalized L_1 -norm of the difference between a simulation with resolution N and one with resolution $2N$ at each point for the three unknowns, which is similar to the convergence tests used in [28].

In figure 4.23(a) are shown $\psi_N(r)$, $\psi_N(\Phi)$ and $\psi_N(\sigma)$ for $N = 50, 100, 200, 400, 800$. We see that all the lines have a slope of approximately minus two (compare with line 'd'), indicating that the functions converge with second order. However, we also need to show that the converging solution is a physical solution of our field equations. We have tested the code against the Reissner-Nordström and Schwarzschild solutions and reproduced all known features (e.g. location of the event horizon as a function of initial mass etc.) of these space-times. If a scalar field is present there are no suitable analytic solutions against which we can compare the numerical results, but we can use the constraint equations (4.8) and (4.9) to test that our code is converging to a physical solution.

Denoting the left hand side of the constraint equations (4.8) and (4.9) by C_1 and C_2 respectively, we calculate the average absolute value of C_1 and C_2 at each point:

$$\chi(x) \equiv \frac{1}{n} \sum_i^n |x^i| \quad (4.51)$$

defined similar to eq. (4.50), with x being either C_1 or C_2 . In figure 4.23(b) are shown $\chi(C_1)$ and $\chi(C_2)$ along $u = 23.00$. It is noted that $\chi(C_2)$ is much greater than $\chi(C_1)$. This is

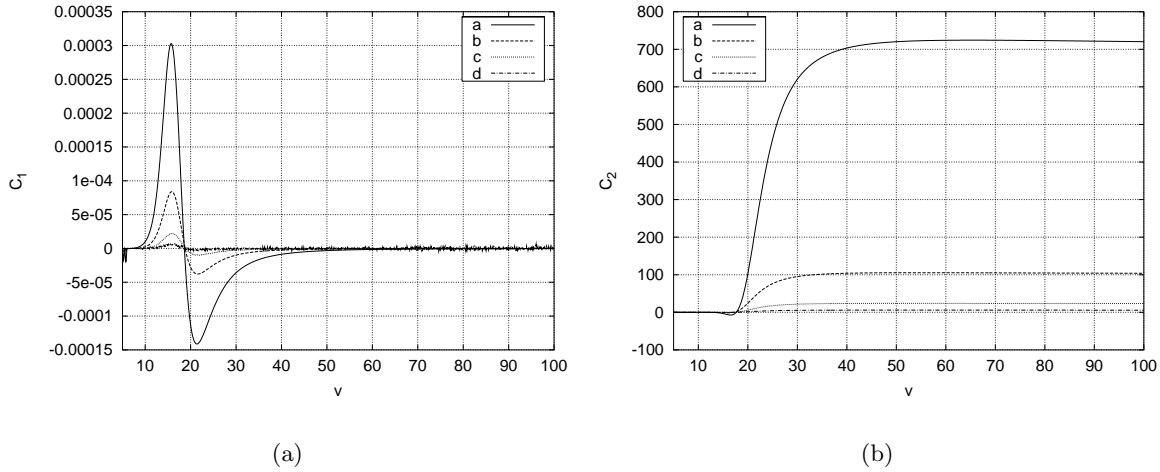


Figure 4.24: C_1 (fig. a) and C_2 (fig. b) along an outgoing ray $u = 23.00$ for resolutions; line a) $N = 100$, b) $N = 200$, c) $N = 400$ and line d) $N = 800$.

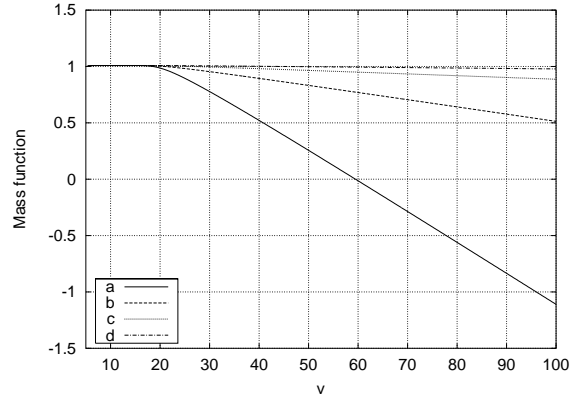


Figure 4.25: Mass function as a function of v for the resolutions; line a) $N = 200$, b) $N = 400$, c) $N = 800$ and d) $N = 1600$.

mainly because the line $u = 23.00$ is very close to the event horizon and the gradients along ingoing rays are here very large. This results in great inaccuracy for coarse resolutions when calculating the derivatives used to calculate C_2 . Related to this is of course the fact that we are not using AMR for these basic convergence tests and hence the large average value for C_2 is also an indication that splitting would be most desirable in this region. However, $\chi(C_2)$ is decreasing with increasing resolution, which is the important result in this context. We note also that the typical absolute value of the biggest term in eq. (4.9) is approximately ten times greater than C_2 even for rough resolutions. This means that the constraint equation is roughly satisfied for this case even though C_2 has very large values. For the highest resolution ($N = 800$), $\chi(C_1)$ shows indications of a slightly decreasing convergence rate. This can also be traced to roundoff errors when calculating the r_{vv} -term of C_1 .

Figure 4.24(a) shows $C_1(v)$ for the resolutions $N = 100, 200, 400, 800$. It is seen that C_1 is clearly converging to zero for increasing resolution. It is also clear that numerical noise play a dominant role for $N = 800$, especially at large v , causing the mentioned decreasing convergence rate effect in fig. 4.23(b). As noted, this numerical noise can be traced to the numerical calculation of the r_{vv} -term in eq. (4.9). The reason that this particular term exhibits large roundoff errors is mainly that $r_{vv} \approx 0$ along the line at which we look. This

results in the subtraction of two nearly equal numbers which results in large roundoff errors. Figure 4.24(b) shows the convergence for C_2 again for $N = 100, 200, 400, 800$. Clearly C_2 is also converging to a zero value, but for a given resolution, C_2 is much larger than C_1 due to the proximity to the event horizon and the absence of AMR in these simulations as explained above.

It is also noted that although C_1 and C_2 seem to be converging with second order accuracy, the convergence rates of C_1 and C_2 are not by themselves as important as the convergence rates of the unknown functions, since C_1 and C_2 are functions of the derivatives of the unknown function. The unknown functions, however, directly measure the convergence rate of the code as these are the actual variables being evolved.

Appendix 4.B.2: Convergence with AMR

Another test to show that the numerical solution is converging to a physical solution is to monitor whether the code is mass conserving. Figure 4.25 shows the mass function (4.15) along the outgoing ray $u = 23.00$ in the interval $5 < v < 100$ for the resolutions $N = 200, 400, 800, 1600$. We see that the mass function is converging to a constant value for high resolutions, further indicating that the code is converging to a physical solution of the field equations.

In the previous subsection we verified that with the fixed increments $\Delta u = \Delta v$, our code converges to a physical solution with second order accuracy. In this subsection we will demonstrate the convergence properties of our code with the splitting algorithm turned on, as a function of the splitting criteria used.

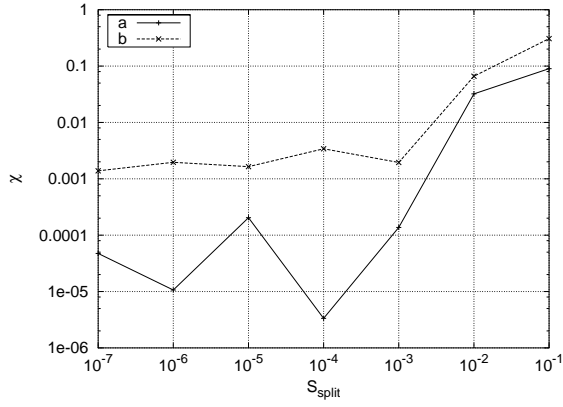
We wish to confirm that our splitting algorithm works as desired and that the numerical solution converges to a physical solution. For this purpose we make a number of simulations with identical initial conditions, but vary the splitting thresholds. We use the same pulse shape as in the previous subsection (eq. (4.49)), but with a wider and stronger pulse with $A = 0.20$ and $v_0 = 5.0$ and $v_1 = 7.0$ which is strong enough to generate a $r = 0$ singularity within our computational domain. Our computational domain is in the range $5 < v < 20$ and $0 < u < 25$. We examine an outgoing ray ($u = 24.60$) which is inside the event horizon and in fact comes very close to the $r = 0$ singularity.

To measure the convergence rates we use eq. (4.50) and (4.51) only in this subsection they are functions of S_{split} (see section 4.7) instead of the resolution N .

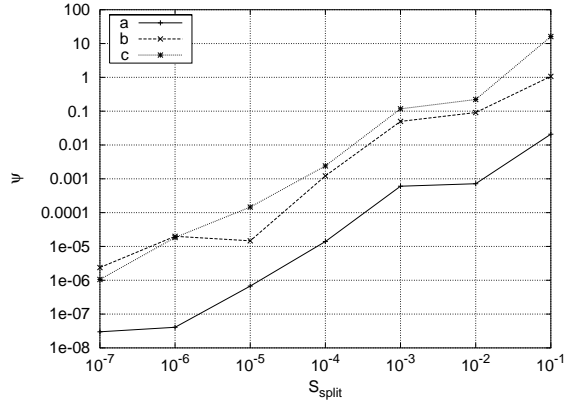
Figure 4.26(a) shows $\chi(C_1)$ and $\chi(C_2)$ as functions of the splitting threshold S_{split} (see section 4.7) that we require the relative numerical error to be below for all computational cells, i.e. the left hand side of the figure denotes a more strict splitting policy. The threshold for desplitting is here and throughout the paper set to two orders of magnitude lower than the splitting threshold, $S_{desplit} = 10^{-2} \cdot S_{split}$. We see that as the splitting threshold S_{split} is decreased, so is the average absolute of C_1 and C_2 , indicating that the numerical solution converges to a physical solution with decreasing error tolerance.

For the lowest splitting threshold at the left side of the figure we see that lower splitting thresholds does not result in significant smaller values of C_1 and C_2 . This arises because C_1 and C_2 becomes so small that numerical noise (which is little affected by resolution) begins to dominate the calculations of C_1 and C_2 .

Figure 4.26(b) illustrates the convergence of the functions r , Φ and σ along the same outgoing ray $u = 24.60$. The figure, which is qualitatively similar to figure 4.23(a), shows the difference between simulations (ψ) with different the splittings thresholds $S_{split} = 10^{-7}, 10^{-6}, 10^{-5}, 10^{-4}, 10^{-3}, 10^{-2}, 10^{-1}$. Since ψ in this subsection is a function of S_{split} instead of N , a point in fig. 4.26(b) illustrates the average absolute difference between the simulation at S_{split} and the simulation with the next higher splittings threshold. For example the leftmost

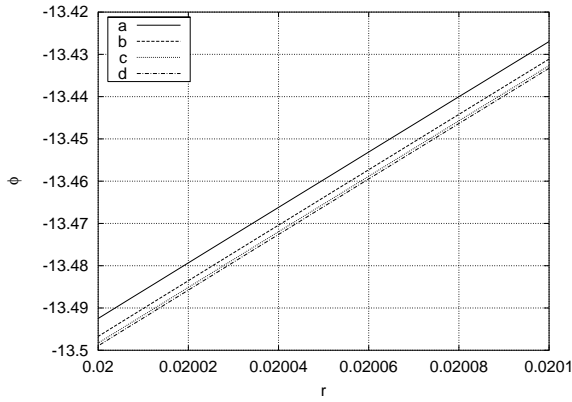


(a) a: $\chi(C_1)$ and b: $\chi(C_2)$.

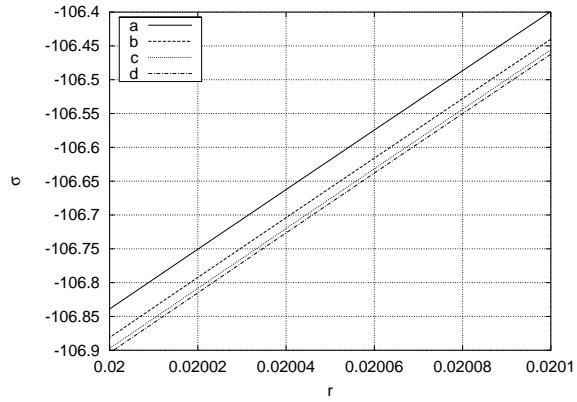


(b) a: $\psi(r)$, b: $\psi(\Phi)$ and c: $\psi(\sigma)$

Figure 4.26: Plots illustrating convergence (with AMR) as function of splitting criterias along outgoing ray at $u = 24.60$.



(a) Φ as a function of r .



(b) σ as a function of r .

Figure 4.27: Φ and σ as functions of r along outgoing ray at $u = 24.60$. Error tolerance intervals are for line a) $S_{split} = 10^{-4}$, b) $S_{split} = 10^{-5}$, c) $S_{split} = 10^{-6}$ and d) $S_{split} = 10^{-7}$. In all cases $S_{desplit} = 10^{-2} \times S_{split}$.

points in fig. 4.26(b) (at $S_{split} = 10^{-7}$) illustrates the difference between simulations with $S_{split} = 10^{-7}$ and $S_{split} = 10^{-6}$.

As the splitting thresholds decreases we expect to see ψ converge to zero. We see that for smaller S_{split} , the ψ decrease indicates a convergence of the unknown functions. This convergence is further demonstrated in figure 4.27 which shows Φ and σ as functions of r close to the $r = 0$ singularity (in the interval $0.02 < r < 0.0201$) along the same outgoing ray that was used for previous plots. From these figures it is clear that even in the vicinity of the $r = 0$ singularity, the unknown functions are converging. It is also important to notice that even though C_1 and C_2 cease to decrease at rather high splitting thresholds, the unknown functions themselves continue to benefit from lower splitting thresholds.

References for Chapter 4

- [1] D. S. Goldwirth and T. Piran, Phys. Rev. D **36**, 3575 (1987).
- [2] E. Poisson and W. Israel, Phys. Rev. **D41**, 1796 (1990).
- [3] A. Ori, Phys. Rev. Lett. **67**, 789 (1991).
- [4] A. Ori, Phys. Rev. Lett. **68**, 2117 (1992).
- [5] M. Gnedin and N. Gnedin, Class. Quant. Grav. **10**, 1083 (1993).
- [6] A. Bonanno, S. Droz, W. Israel, and S. Morsink, Proc. Roy. Soc. London A **450**, 553 (1994).
- [7] P. R. Brady and J. D. Smith, Phys. Rev. Lett. **75**, 1256 (1995).
- [8] S. Droz, Helv. Phys. Acta **69**, 257 (1996).
- [9] L. M. Burko and A. Ori, eds., *Internal structure of black holes and spacetime singularities*, vol. 13 of the Annals of the Israel Physical Society (Israel Physical Society, Jerusalem, 1997), ISBN 0-7503-05487.
- [10] L. M. Burko, Phys. Rev. Lett. **79**, 4958 (1997).
- [11] L. M. Burko, Phys. Rev. **D59**, 024011 (1999).
- [12] L. M. Burko and A. Ori, Phys. Rev. **D57**, R7084 (1998).
- [13] L. M. Burko, Phys. Rev. **D60**, 104033 (1999).
- [14] L. M. Burko, Phys. Rev. **D66**, 024046 (2002).
- [15] L. M. Burko, Phys. Rev. Lett. **90**, 121101 (2003), erratum in Phys. Rev. Lett. **90**, 249902 (E) (2003).
- [16] Y. Oren and T. Piran, Phys. Rev. **D68**, 044013 (2003).
- [17] S. Hod and T. Piran, Phys. Rev. **D55**, 3485 (1997).
- [18] S. Hod and T. Piran, Gen. Rel. Grav. **30**, 1555 (1998).
- [19] S. Hod and T. Piran, Phys. Rev. Lett. **81**, 1554 (1998).
- [20] A. Ori, Phys. Rev. Lett. **83**, 5423 (1999).
- [21] A. Ori, Phys. Rev. **D61**, 024001 (2000).
- [22] B. K. Berger, Living Reviews Relativity (2002), <http://www.livingreviews.org/gr-qc/0201056>.
- [23] A. Hamilton and S. Pollack, gr-qc/0411061 (2004).
- [24] A. Hamilton and S. Pollack, gr-qc/0411062 (2004).
- [25] M. Dafermos, Proceedings of the Seventh Hungarian Relativity Workshop (2004), to appear, gr-qc/0401121.
- [26] V. P. Frolov and I. D. Novikov, *Black Hole Physics* (Kluwer Academic Publishers, 1998).

- [27] O. Gurtug and M. Halilsoy, gr-qc/0203019 (2002).
- [28] L. M. Burko and A. Ori, Phys. Rev. **D56**, 7820 (1997).
- [29] L. M. Burko, Phys. Rev. **D58**, 084013 (1998).
- [30] C. W. Misner, K. S. Thorne, and J. A. Wheeler, *Gravitation* (W. H. Freeman, San Francisco, 1973).
- [31] E. Poisson and W. Israel, Phys. Rev. Lett. **63**, 1663 (1989).
- [32] Y. B. Zeldovich and I. D. Novikov, *Relativistic Astrophysics*, vol. II, The Structure and Evolution of the Universe (The University of Chicago press, 1983).
- [33] W. B. Bonnor and P. C. Vaidya, Gen. Relativ. Gravit. **1** (1970).
- [34] L. P. Grishchuk, Sov. Phys. Doklady **190**, 1066 (1970).

